Islamic University of Gaza
Engineering Faculty
Civil Engineering Department
Infrastructure Engineering

الجامعة الإسلامية – غزة
كلية الهندسة
قسم الهندسة المدنية
فرع البنى التحتية

Spatio -Temporal Analysis of the Dead Sea Area Using Remote Sensing and GIS-Based Model: Markov - Cellular Automata

Prepared by:
Mohammed Habboub

Supervised by:
Dr. Maher El-Hallaq

A Thesis Submitted in Partial Fulfillment of the Requirements for the Degree of Master in Infrastructure Engineering

2013

Abstract

Understanding spatio-temporal changes is essential to many aspects of engineering, geographic and planning researches. The area of the Dead Sea surface - at the end of the fifties - was about 1000 km^2. The altitude of the surface was around 350 m below sea level. Since 1978, the Dead Sea has retreated, and the sea body turned into two basins: the principal northern one that was about 631.27 km^2 with a water level of about -430 m MSL (in 2010), and the shallow southern one with the Lisan Peninsula and the Lynch Straits in between, which has a sill elevation of about 400 m below the sea level.

In this research fourteen satellite imageries are collected from 1972 to 2010 in addition to 2011-ASTGTM-DEM. Satellite imageries are radiometrically and atmospherically corrected. Geographic Information system and Remote Sensing techniques are used for spatio-temporal analysis in order to detect changes in the Dead Sea area, shape, water level, and volume.

Dead Sea shrinks by 2.5 km^2/yr while the water level decreases by 0.7 m/yr. Consequently, the volume changes by - 0.33 km^3/yr. The use of Dead Sea water for the industry by both Israel and Jordan is one of the essential factors that affect area of the Dead Sea. The intensive human water consumption from the Jordan and Yarmouk Rivers for other usage are the main reasons of that shrinkage in area as well.

The direction of this shrinkage is from the north, northwest and from the south direction of the northern part due to slopes of bathymetry. No shrinkage is considered from the east direction due to the same reason since the bathymetric slope is so sharp.

In order to make a rational prediction of the Dead Sea shape, data is prepared for suitability map creation using Markov chain analysis and Multicriteria Evaluation (MCE). Then, Markov Cellular Automata model and spatial statistics are used in prediction and validation processes. The validation process shows a standard Kappa index of 0.9545 which means a strong relation between the model and reality.

The predicted shapes of 2020, 2030 and 2040 follow the same conditions from 1984 to 2010. The predicted areas of 2020, 2030 and 2040 are 610, 591 and 574 km^2 which are considered a logical extension of the trend from 1984 till 2010. So, Markov - Cellular Automata model can be used to predict closed seas as the Dead Sea.

الخلاصة

إن فهم التغيرات المكانية خلال فترات الزمن المختلفة أو ما يسمى بالتحليل (الزمكاني) يعد من أهم الجوانب البحثية الهندسية وغير الهندسية، فمنطقة البحر الميت - منطقة الدراسة - تعد مثالاً حياً ومحلياً لمثل هذه التغيرات.

إن مساحة المسطح المائي للبحر الميت في الخمسينيات كانت ما يقارب 1000 كم^2 وبمنسوب 350م تحت سطح البحر، ولكن منذ 1978 تم تقسيم البحر الميت إلى جزئين، الجزء الأساسي وهو الجزء الشمالي والذي تبلغ مساحته 631.27 كم^2 وبمنسوب 429.9 م تحت سطح البحر خلال سنة 2010، والجزء الجنوبي الضحل الذي تحول إلى برك صناعية لتسريع عمليات البخر.

في هذا البحث تم استخدام 14 صورة فضائية من سنة 1972 إلى سنة 2010، بالإضافة إلى نموذج الارتفاعات الرقمية الحرارية ASTGTM-DEM لسنة 2011. حيث تمت معالجة هذه الصور من العيوب الطيفية المختلفة سواء كانت بسبب العوامل الجوية أو زاوية ميل الشمس أو اختلاف نوع مجسات القمر الصناعي. واستخدمت تقنيات نظم المعلومات الجغرافية والاستشعار عن بعد في دراسة التغيرات الزمكانية للبحر الميت من حيث الشكل، المساحة، المنسوب والتغير في الحجم.

وقد خَلُصَت نتائج البحث بأن مساحة البحر الميت تتقلص بمعدل 2.5 كم^2 سنوياً ومنسوب مياهه يتناقص بمعدل 0.7 م كل عام، و كنتيجة لهذا التناقص، فإن التغير السنوي للحجم يقدر بـ 0.33- كم^3. وتعزو الدراسات الهيدرولوجية هذا التناقص بسبب السدود الحاجبة لمياه نهر الأردن واليرموك للوصول للبحر الميت وللإستخدام الجائر لمياه البحر الميت في الصناعات الأردنية وصناعات الاحتلال الإسرائيلي.

أما الإتجاه الجغرافي للتغير فمحصور بشكل تضاريس أعماق للبحر، وخَلُصَت الدراسة إلى أن التناقص يحدث من الجهة الشمالية الغربية و الجهة الجنوبية للجزء الشمالي من البحر الميت، ولا وجود لأي تناقص من الجهة الشرقية لوجود ميل حاد للأعماق في تلك الجهة.

تم استخدام نموذج ماركوف للخلايا ذاتية السلوك Markov Cellular Automata في عمليات التنبؤ المستقبلي لشكل و مساحة البحرالميت، بحيث تم تجهيز البيانات المختلفة لإستنباط خريطة الملائمة suitability map باستخدام تحليل متسلسلة ماركوف Markov chain analysis

والتقييم متعدد المعايير Multicriteria Evaluation ثم بتطبيق كل من نموذج ماركوف للخلايا ذاتية السلوك Markov Cellular Automata والتحليل الإحصائي المكاني في عمليات التحقق من كفاءة وفاعلية النموذج والبيانات المستخدمة في التقييم متعدد المعايير Multicriteria Evaluation بحيث كانت نتائج التحليل الإحصائي توكد فاعلية هذا النموذج بنسبة 95.45% والتي تعتبر مؤشراً لعلاقة قوية بين نموذج التنبؤ والواقع.

وبإفتراض أن الظروف المناخية ومعدلات السحب لسنوات التنبؤ ستكون امتداداً طبيعياً للفترة ما بين 1984 و 2010، تم التنبؤ بشكل ومساحة البحر الميت لسنة 2020 ، 2030 و 2040 البالغة 610، 591 و574 كم^2 على الترتيب وهي مساحات إذا ما قورنت بمعدل التناقص العام للبحر الميت، وجدت أنها مساحات منطقية.

وقد خلصت الدراسة الى كفاءة نموذج ماركوف للخلايا ذاتية السلوك Markov Cellular Automata في التنبؤ بأشكال ومساحات البحار المغلقة كالبحر الميت.

Dedication

This thesis is lovingly dedicated to my parents who have always stood by me and dealt with all of my absence from many family occasions with a smile. Their support, encouragement, and constant love have sustained me throughout my life.

Acknowledgement

First of all, I would like to express the deepest appreciation to Allah for everything that has been given to me. I would also like to thank my parents for their continuous encouragement.

In addition, I would like to express my gratitude to my supervisor Dr. Maher El-Hallaq for his useful comments, remarks and engagement through the learning process of this master thesis. Furthermore, I would like to thank my committee members, Dr. Alaeddinne Ajamassi and Dr. Mazen Abualtayef, who accept to discuss this thesis.

Special thanks to Mr. Riccardo Klinger, who introduced me to ERDAS imagine and kindly supported me though this thesis. I also thank Prof. R. Douglas Ramsey for his helpful advices. Many thanks for Mr. Skye Cooley for his creative articles in "GIS 4 Geomorphology" website. Thanks a lot to Eng. Jamal Numan from Ramallah and the labs of Clark University for their technical support in IDRISI program. I would also like to thank the United Nations Educational, Scientific and Cultural Organization (UNESCO) for their free educational material on the internet.

Finally, I would like to give my thanks to everybody supported me during my master degree.

Table of Contents

List of Figures

List of Tables

Abbreviations and Notations

ASTGTM-DEM	Advanced Space-borne Thermal Emission and Reflection Radiometer Global Digital Elevation Model
A	The overall allocation disagreement, (%)
A_{1984}	Dead Sea area in year 1984
a_g	The Allocation disagreement, (%)
AOI	Areas of Interest
APC	Arab Potash Company
A_t	Dead Sea area in a given time
AVHRR	Advanced Very High Resolution Radiometer
C	The proportion of agreement, (%)
CA	Cellular Automata
CA_Markov	Markov Cellular Automata
C_i	Criteria for suitability
COST	Cosine of the Solar zenith angle
CVA	Change Vector Analysis
D	The total disagreement, (%)
D’	The Normalized Earth-Sun distance, astronomical units
DOP	Depth of Penetration
DOS	Dark Object Subtraction
DSW	Dead Sea works
$E_{band\ N}$	Solar Irradiance for Band N, (watts/ (m^2 . μ))
ERDAS	Earth Resources Data Analysis System
ETM+	Enhanced Thematic Mapper Plus
GIS	Geographic Information System
GSA	Greater Shanghai Area
H_{1984}	Dead Sea water level in year 1984
$H_{band\ N}$	The Digital Number representing Dark Object for Band N
H_t	Dead Sea water level in a given time
ISODATA	Iterative Self-Organizing Data Analysis Technique

JD	Julian Day
K(m)	Perfect stratum
KIA	Kappa Index of Agreement
$K_{location}$	Kappa for grid-cell level location
$K_{location\ Strata}$	Kappa for stratum-level location
K_{no}	Kappa for no information
$L_{band\ N}$	The Digital Number for Band N
$L_{max\lambda}$	The spectral radiance that is scaled to (QCALMAX), (watts × (m^2 . ster . μm) $^{-1}$)
$L_{min\lambda}$	The spectral radiance that is scaled to (QCALMIN), (watts × (m^2 . ster . μm) $^{-1}$)
LU_t	The distribution of land uses among the different types at the beginning of the projection period
LU_{t+1}	The distribution of land use types at the end of the projection period
M(m)	The proportion of grid cells classified correctly
MCE	Multi-Criteria Evaluation
MODIS	Moderate Resolution Imaging Spectroradiometer
MSL	Mean sea level
MSS	Multispectral Scanner
N(i, j)	The observed data during the transition from state i to j
NASA	National Aeronautics and Space Administration
NDVI	Normalized Difference Vegetation Index
$N_{i,j(t)}$	The Neighborhood index of cell i,j.
n_{ij}	The number of years between time step i and step j
P	Transition probability matrix
P(i, j)	The yearly transition probability
Q	The overall quantity disagreement, (%)
QCALMAX	The maximum quantized calibrated pixel value (corresponding to $LMAX_\lambda$) in DN
QCALMIN	The minimum quantized calibrated pixel value (corresponding to $LMIN_\lambda$) in DN
q_g	The Quantity disagreement, (%)

r_i	Restriction
RS	Remote Sensing
$S_{i,j\,(t)}$	Suitability indexes of cell i,j at time t
SGB	Stochastic Gradient Boosting
SLC-off	Scan Line Corrector Failure
TM	Thematic Mapper
USGS	U.S. Geological Survey
ΔV	The change in volume
W_i	Weight for a criteria i
θ	The Sun Azimuth, degrees
$\rho_{Band\ N}$	The Reflectance for Band N, (%)

CHAPTER 1

1 Introduction

Understanding changes in wetlands, land-uses, seashores and vegetation areas over time is essential to many aspects of engineering, geographic and planning researches. Imagery acquired by airborne or satellite sensors provide an important source of information for mapping and monitoring the natural and manmade features on the land surface. Interpretation and analysis of remotely sensed imagery requires an understanding of the processes that determine the relationships between the property the sensor actually measures and the surface properties we are interested in identifying and studying (Smith, 2012). However, dealing with imageries which describe these temporal changes is still a little bit restricted because these imageries describe only a past data.

1.1 Research Problem

According to Omar (1996), the decrease of inflow into the Dead Sea is causing its shoreline to undergo very fast and to change dynamically in area. The area of the Dead Sea surface - at the end of the 1950's - was about 1000 km^2 of which about 757 km^2 where located in the northern part and 240 km^2 in the southern part. The altitude of the surface was around 350 m below sea level. The Dead Sea began receding gradually. This occurred as a result of the hydraulic projects started by Jordan and Israel (Israeli occupation) in the basin. These projects resulted in a gradual decrease of the amount of discharge into the Dead Sea, and thus the shorelines began to shrink. During the 1980s this increased further. By the 1990s the situation became very grave.

1.2 Aim and Objectives

This research aims to conduct a spatio-temporal analysis of the Dead Sea Area based on satellite imagery using Remote Sensing (RS) and Geographic Information System (GIS) techniques. To achieve this aim, the following objectives are to be considered:

- Detecting the magnitude and direction of change occurred at the Dead Sea Area, water level and shape.
- Predicting the area and shape of the Dead Sea in the future.

1.3 Methodology

The methodology was as follows;

1. Literature review.

2. Collecting data: Data was collected from official websites; National Aeronautics and Space Administration (NASA) and U.S. Geological Survey (USGS). The study focuses on satellite images which captured by the Landsat (1, 2, 3, 4, 5 &7) satellites.
3. Using image processing environment (e.g., Earth Resources Data Analysis System software, ERDAS) in restoring, enhancing, classifying and transforming images when required.
4. Using raster/vector overlay analysis in order to detect change; ArcGIS software was used to overlay, extract and intersect shapes in a vector format.
5. Applying a spatio-temporal analysis to study the changes over time.
6. Predicting the future shape of the Dead Sea Area using CA_Markov which combines Cellular Automata (CA) model and Markov chain analysis.
7. Model Validation.
8. Getting conclusion and recommendation.

1.4 Thesis Structure

This thesis is oriented into six chapters. Chapter one gives an introduction about the thesis including problem statement, aim and objectives, general methodology as well as the structure of this thesis.

In chapter two, change detection, spatio-temporal analysis, Markov chain analysis, cellular automata and statistical validation are defined. An overview of the change detection methods and algorithms over time is discussed. Then, case studies about wetlands change detection, CA_Markov and Dead Sea Area are summarized from previous literatures.

Chapter three gives an overview about the study area location, hydrology, geology, as well as economic and political issues related to the study area.

In chapter four, methodology is described in details; image pre-processing, supervised classification, change detection analysis and prediction analysis are explained.

Chapter five lists and discusses change of the Dead Sea shape, area, water level and volume over time. Then, it illustrates the relation between area and water level of the Dead Sea. After that, it also discusses the validation results of the CA_Markov model. Finally the result of predicted shape, area and volume are illustrated and explained.

At the end, chapter six gives a general conclusion and recommendations.

CHAPTER 2

2 Literature Review

2.1 Scope

In this chapter, change detection and spatio-temporal analysis (time series analysis for spatial scenes), are defined. Then, change detection development over time is overviewed. After that, methods, algorithms and case studies about wetlands change detection are summarized from previous literatures. Next, Markov chain, Cellular Automata and statistical validation are defined. Finally, previous studies about CA_Markov and Dead Sea Area are summarized from previous literatures.

2.2 Introduction

Change information of the earth's surface is becoming more and more important in monitoring the local, regional and global resources and environment. Large collection of past and present remote sensing imagery makes it possible to analyze spatio-temporal pattern of environmental elements and impact of human activities in past decades (Jianya, et al., 2008).

2.3 Change Detection Definitions

Singh (1989) defines change detection as the process of identifying differences in the state of an object or phenomenon by observing it at different time. Another definition of change detection is a technology ascertaining the changes of specific features within a certain time interval. It provides the spatial distribution of features and qualitative and quantitative information of features changes (Kandare, 2000). Simply, U.S. Department of Defense defines change detection as an image enhancement technique that compares two images of the same area from different time periods. Identical picture elements are eliminated, leaving signatures that have undergone change.

2.4 Development of Change Detection over Time

Change detection history starts with the history of Remote Sensing. Thereafter, the development of change detection is closely associated with military technology during World Wars I and II and the strategic advantage provided by temporal information acquired by Remote Sensing. The civilian applications development of digital change detection era really started with the launch of Landsat-1 in July 1972. However, the development was limited by data processing technology capacities and followed closely the development of computer technologies (Théau, 2012).

2.5 Methods and Algorithms

Change detection algorithms analyze multiple images of the same scene – taken at different times – to identify regions of change (AUG signals, 2008). Singh (1989) classifies change detection methods into two types, namely, classification comparison and direct comparison. Deer (1999) proposes a classification of three categories, including pixel-based, feature-based and object-based change detection. LU, et al. (2004) generalizes the change detection methods into seven types, namely, arithmetic operation, transformation, classification comparison, advanced models, GIS integration, visual analysis and some other methods. Richard, et al. (2005) summarizes change detection methods in general terms and propose a classification of direct difference, statistical hypothesis testing, predictive models, shading model, and background modeling and so on. Jianya, et al. (2008) classifies change detection from its approaches, namely, bi-temporal change detection and temporal trajectory analysis. The former measures changes based on a 'two-epoch' timescale, i.e. the comparison between two dates. The latter analysis the changes based on a 'continuous' timescale, i.e. the focus of the analysis is not only on what has changed between dates, but also on the progress of the change over the period. AUG signals (2008) classifies change detection algorithms as algorithms based on pixel amplitude, both the magnitude and phase, or on transformed pixel values. Théau (2012) classifies change detection methods based on history since the algebra techniques such as image differencing or image rationing were the first techniques used to characterize changes in digital imagery then more complex techniques were developed since then with the improvement of processing capacities but also with the development of new theoretical approaches.

2.6 Time Series Analysis Definition

Data gathered sequentially in time are called a time series. Environmental modeling, meteorology, hydrology, the Advanced Spaceborne Thermal Emission and Reflection Radiometer Global Digital Elevation Model (ASTGTM-DEM) graphics and engineering are some examples in which spatio-temporal (time series of spatial scenes) arise. The simplest form of data used in time series is a longish series of continuous measurements at equally spaced time points. That is, observations are made at distinct points in time, these time points being equally spaced and, the observations may take values from a continuous distribution. Assume that the series X_t runs throughout time, that is$(X_t)_{t=0\pm1\pm2\pm3\ldots}$, but is only observed at times $t = 1,\ldots,n$ (Reinert, 2010).

Time series analysis is a technology ascertaining the changes of specific features within a certain time interval. It provides the spatial distribution of features and qualitative and quantitative information of features changes (Kandare, 2000).

There are, obviously, numerous reasons to record and to analyze the data of a time series. Among these is the wish to gain a better understanding of the data generating

mechanism, the prediction of future values or the optimal control of a system. The characteristic property of a time series is the fact that the data are not generated independently, their dispersion varies in time, they are often governed by a trend and they have cyclic components. Statistical procedures that suppose independent and identically distributed data are, therefore, excluded from the analysis of time series. This requires proper methods that are summarized under time series analysis (Falk, et al., 2011).

The quantitative analysis for identifying the characteristics and processes of surface changes are carried through from the different periods of remote sensing data. It involves the type, distribution and quantity of changes, that is the ground surface types, boundary changes and trends before and after the changes (Shaoqing, 2008) .

Time series analysis is mainly used for temporal trajectory analysis. In contrast to bi-temporal change detection, the temporal trajectory analysis is mostly based on low spatial resolution images such as Advanced Very High Resolution Radiometer (AVHRR) and Moderate Resolution Imaging Spectroradiometer (MODIS), which have a high temporal resolution. The trade-off of using these images, however, is the lost of spatial details that makes auto-classification very difficult, so that the temporal trajectory analysis is commonly restricted in, for example, vegetation dynamics in large areas, or change trajectories of individual land cover classes. Quantitative parameters such as Normalized Difference Vegetation Index (NDVI) or area of given land cover class are often used as the dependent variables for the establishment of change trajectories (Jianya, et al., 2008).

2.7 Wetlands and Change Detection

Moayeri, et al. (2012) studies Hurol Azim wetland that bordering Iran and Iraq, Landsat satellite images taken by the users in the past years reveal the fact that Hurol Azim wetland area has been smaller in recent decades. The purpose of this study is the wetland changes of Thematic Mapper (TM) and Enhanced Thematic Mapper Plus (ETM+) sensor of Landsat imagery in 1990 and 2005. The principal components analysis method was used to determine the aim. The result showed that the wetland area of Hurol Azim has been smaller of 515.4 km^2 in 1990 to 230.59 km^2 in 2000. The main reasons for wetland reduced water levels are dam of Karkheh and drought.

Ndzeidze (2009) utilizes remote sensing and GIS to determine the extent of change of the wetland area and of other land use and land cover classes in the Upper Noun drainage basin from 1973 to 2007. In this study, a supervised maximum likelihood algorithm classification method is used on available Landsat Multispectral Scanner (MSS), (TM) and (ETM+) imagery from 1978 to 2002. A significant drop in area of permanent and seasonally flooded prairies was observed. This study thus provides base

data for monitoring human impacts on the Upper Noun drainage basin and its natural habitats, especially within and around the wetland.

RUAN et al. (2008) aims to study the potential of a time series of remotely sensed data for the change detection of wetland in Hongze Lake in the Northern Jiangsu Province. The raw data comprised three digital images acquired between 1979 and 2002. The task proceeded in three parts. First, following pre-processing and registration to the topography at the scale of 1:100,000, the ETM+ image of 2002 was classified by using hybrid classification techniques. A thematic feature space image of near-infrared versus red was created based on the above classification results. Second, the historical remotely sensed data were clustered using standard unsupervised classification technique; Iterative Self-Organizing Data Analysis Technique (ISODATA). Then the clusters were labeled into information classes by means of the selection of core clusters, the relationship of clusters between clusters in feature space and geographical space. Third, the class "Emergent" was extracted from the three dates of thematic maps and recoded respectively as three files. The three files were then overlaid for the analysis of wetland change. The distribution of the class "Emergent" and its change as time and in space were used as indicators for the change of wetland environment. The results showed that a great loss of wetland has occurred in the study area in the past more than 20 years.

Baker et al. (2007) uses Landsat-based satellite imagery from 1988 and 2001 to map changes in wetland ecosystems in the Gallatin Valley of southwest Montana. Stochastic Gradient Boosting (SGB) algorithm was used to classify the 2001 image, and Change Vector Analysis (CVA) was used to identify locations where wetland areas might have changed between 1988 and 2001. These potentially changed locations again were classified for the 1988 Landsat image using SGB. Areas of change constituted 3.4% of the study area, thus only this small percentage of the image was reclassified for the 1988 image. Overall change detection accuracy was 76%, although changes along the periphery of wetland boundaries and in areas of smaller upland inclusions were not distinguished as well as other changes. Overall accuracies of the SGB wetland classification maps were 81% for 1988 and 86% for 2001. CVA significantly reduced the number of pixels involved in the historical image classification compared to conducting independent classifications, thus reducing the potential for compounding classification errors in unchanged areas.

2.8 Markov Chain Analysis

Eastman (2012) defines Markovian process as the state of a system at time 2 can be predicted by the state of the system at time 1 by given a matrix of transition probabilities from each cover class to every other cover class.

The application of Markov analysis is basically used to study of land use change and land use impact assessment. Recently, Markov analysis of land use change has been

combined with GIS to create a tool for visualizing and projecting the probabilities of land use change among categories of land use. Figure 2-1 shows a schematic illustration that illustrates the inputs and outputs of Markov chain. All Markov parameters will be discussed in chapter four in details.

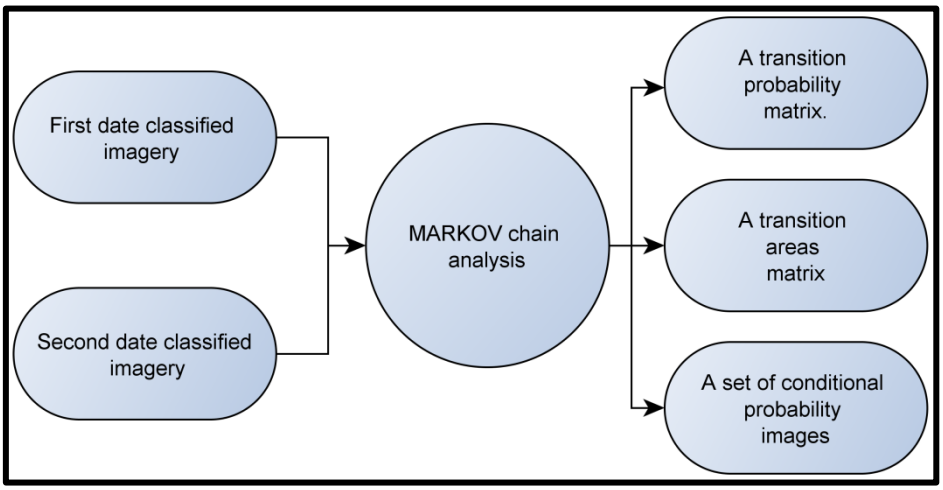

Figure 2-1 The inputs and outputs of Markov chain

All landscape spatial transition models can be expressed in a simple matrix equation as follows (TANG, et al., 2007):

$$\boldsymbol{LU_{t+1} = LU_t \times P} \qquad \textbf{Equation 2-1}$$

where LU_t is the distribution of land uses among the different types at the beginning of the period and LU_{t+1} is showing the distribution of land use types at the end of the projection period (Briassoulis, 2012) in other words LU_t and $LU_{t+1}$are vectors composed of the fractions of each landscape type at time t and time t+1, respectively.

TANG et al. (2007) defines P as a square matrix, whose cell P_{ij} is the transition probability from landscape i to j during times t and t + 1, while Memarian et al. (2012) described the transition probability, P_{ij}, as the probability of moving from one state i to another state which could be represented in the form of a transition matrix, P. Equation 2-2 illustrates the P matrix.

A transition areas matrix expresses the total area (in cells) expected to be changed in the next time period. A set of conditional probability images expresses the probability that each pixel will belong to the designated class in the next time period.

They are called conditional probability maps since this probability is conditional on their current state (Eastman, 2012).

$$P = \begin{bmatrix} p_{11} & p_{12} & \cdots & p_{1n} \\ p_{21} & p_{22} & \cdots & p_{2n} \\ \cdots & \cdots & \cdots & \cdots \\ p_{n1} & p_{n2} & \cdots & p_{nn} \end{bmatrix}$$ Equation 2-2

The transition probabilities P in K steps are derived from the landscape transitions occurring during some time interval as shown in equations 2-3 and 2-4 (TANG, et al., 2007):

$$P_m(i,j) = \frac{N(i,j)}{\sum_{k=1}^{k} n_{ij}}$$ Equation 2-3

$$P(i,j) = \sum_{k=1}^{k} \frac{P_m(i,j)}{K n_m}$$ Equation 2-4

Where N(i, j) is the observed data during the transition from state i to j, and n_{ij} is the number of years between time step i and step j, and the total number of years is m; P(i, j) is the yearly transition probability after normalizing the transition probability in multiyear and K is the number of steps (TANG, et al., 2007).

Briassoulis (2012), Bell et al. (1977) and TANG et al. (2007) mentions that there are several assumptions for Markov chain;

- The change is stochastic not deterministic.
- Markov chain gives a set of discrete classes which has to be identified clearly since the process can be in one and only one of these classes at a given time.
- It moves successively from one state to the other with some probability which depends only on the current state and without considering the other historical values, LU_1, LU_2, LU_3….
- The cells in the transition matrix are probabilities, it follows equation 2-5.

$$\sum_{j=1}^{m} P(i,j) = 1$$ Equation 2-5

One of the disadvantages of Markov chain is that it has a very limited spatial knowledge. To improve the spatial sense of these conditional probability images, using Cellular Automata model will be a good choice.

2.9 Cellular Automata (CA)

CA is a grid of cells with each cell updating its value based on its neighboring cell

values (Yao, 2010) while Eastman (2012) defines CA as a cellular entity that independently varies its state based on its previous state and that of its immediate neighbors according to a specific rule. Although this definition is so close to Markov chain, the only difference is that the application of a transition rule which depends not only upon the previous state, but also upon the state of the local neighborhood. So, the state of a cell is determined by the previous states of the surrounding neighborhood of cells. Each cell in a regular spatial lattice can have any one of a finite number of classes.

CA consists of different elements. They are; cell space which is one cell that can be in any geometric shape, cell state that represent any spatial variable, a sequence of discrete time steps, transition rules which is a rule specifies the state of cell before and after updating based on its neighbors. A limited neighborhood (Von Neumann) neighborhood including 4 or 12 adjacent cells for 3x3 filter and 5x5 filter respectively as shown in Figures 2-2-A and 2-2-C or an extended neighborhood (Moore) including the 8 or 24 adjacent cells for 3x3 filter and 5x5 filter respectively as shown in Figures 2-2-B and 2-2-D. See (equation 2-7) below which illustrated the effect of the neighborhood type (Collet, et al., 2012) (Fonstad, 2006).

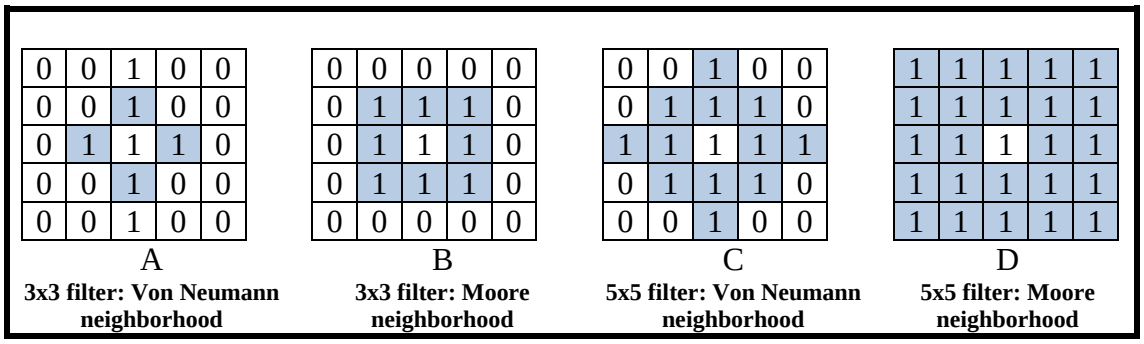

Figure 2-2 Neighborhood type (Fonstad, 2006) modified

2.10 CA_Markov

CA_Markov has the ability to simulate land use changes among multiple categories and combines the CA and Markov chain procedures. Markov analysis does not account for the causes of land use change and it is insensitive to space (Memarian, et al., 2012) .

IDRISI software illustrates a technique of CA_Markov since a Markov chain analysis is performed in order to estimate the transition matrix between the two past dates and to estimate probabilities of change for the third date to be predicted. Then, a Cellular Automata (CA) estimates the spatial distribution of landcover at a later date.

Equations 2-6 and 2-7 below illustrate the evaluation of cells from time t to t+1 is determined by a function of its state, its neighborhood space and a set of transition rule (Samat, et al., 2011).

$$LU_{i,j(t+1)} = f\left(LU_{i,j(t)}.S_{i,j(t)}.P_{x,y,i,j(t)}.N_{i,j(t)}\right) \quad \text{Equation 2-6}$$

$$N_{i,j(t)} = \frac{\sum^{t} N_{i,j(t)}}{\#\ \text{ofadjacent cells}} \quad \text{Equation 2-7}$$

Where:

- $LU_{i,j\,(t+1)}$: The potential of cell i,j to change at time t+1,
- $LU_{i,j\,(t)}$: States of cell i,j at time t,
- $S_{i,j\,(t)}$: Suitability indexes of cell i,j at time t [see equation 4-4] ,
- $P_{x,y,i,j\,(t)}$: Probability of cell i,j to change from state x to state y at time t(as shown in equation 2-3above, and;
- $N_{i,j\,(t)}$ Neighborhood index of cell i,j.

2.11 Previous Studies Using CA_Markov

Cabral, et al., (2006) investigates urban dynamics of Sintra-Cascais municipalities (Portugal) between years 1989 and 2025 using different land change models: two cellular automata-based models in different filters. The researcher used classified data of three Landsat time series satellite images (1989, 1994 and 2001). Models' validation and performance are assessed comparing predicted year of 2001 against year 2001 real classification. Two different resolutions are tested: pixels and the objects obtained by image segmentation for the classification of image of 2001. Among the models tested, 3x3 filter was the one that exhibited the best overall performance at the object level because of additional spatial component used. Results further indicate that one must use the same spatial unit of analysis that was employed in the image classification procedure to achieve better modeling estimates.

Wen (2008) uses CA_Markov model to predict the changes of wetland area in Lindu Enclave area & Lindu Lake, Indonesia. Land cover 1983 from aerial photography, Landsat TM 2002 and 2006 are used as the spatial model data. Multicriteria Evaluation (MCE) for wetland area created with soil map, topography map, and land cover map as the variables for suitable wetland area criteria that will be used in CA model. Finally, Markov chain probability values for each class and multicriteria evaluation map is merged with the CA model with 3 x 3 cell neighbors analysis then spatial wetland change prediction map for 2021 can be created. The results show that CA_Markov model can be used to predict wetland change area as well as land use.

Zhang et al. (2009) investigates the CA_Markov model under different development schemes for simulations of the urban expansion scenarios of Greater Shanghai Area (GSA) in 2015 and 2025 in support of sustainable urban development. In this study, multitemporal land cover dataset, derived from remotely sensed images from 1995,

2000 and 2005 were used for simulation and validation. Through this study, the combined approach using remote sensing data, GIS spatial analysis environment and urban simulation model with landscape metrics and scenario analysis proved to be effective to understand, represent and predict the spatial-temporal dynamics of urban evolution, and CA_Markov model is a useful tool for simulating the scenarios of future urban developments, even though there are some issues that need to be investigated in the future, such as the construction of localized schemes, and the incorporation of political, social, economic and cultural factors.

Kushwaha et al. (2011) focuses on the forest ecosystem dynamics assessment and predictive modeling deforestation and forest cover prediction in a part of north-eastern India using temporal satellite imagery of 1975, 1990 and 2009 and predicted forest cover for the period 2028 using CA_Markov. The study highlighted large-scale deforestation in the study area during 1975-1990 as well as 1990-2009 forest cover vectors. A net loss of 2,334.28 km^2 forest cover was noticed between 1975 and 2009, and with current rate of deforestation, a forest area of 4,563.34 km^2 will be lost by 2028. The annual rate of deforestation worked out to be 0.35 and 0.78% during 1975-1990 and 1990- 2009 respectively. Kushwaha et al. (2011) says that the study demonstrated high potential of RS and GIS for forest ecosystem dynamics assessment and the efficacy of CA_Markov to predict the forest cover change.

Samat et al. (2011) mentions the study undertaken in Seberang Perai region of Penang State which experience significant land use transformation since the 1970s. GIS was integrated with CA_Markov model to evaluate land use changes and forecast land use pattern until the year 2020. It was found that significant changes have occurred since 1990s and the same urban growth pattern will continue.

2.12 Validation

IDRISI software offers a comprehensive statistical analysis that answers how well a pair of maps agrees in terms of the quantity and location of cells in each category, various Kappa Indices of Agreement (KIA) and related statistics have been derived to indicate how well the comparison map agrees with the reference map. These methods of validation have been created recently at Clark University by Gil Pontius .Therefore, there are no explanations of these statistics in common statistical books. It is highly recommended to see (Pontius, 2000), (Pontius, 2002) and (Pontius, et al., 2011) for more information.

Validation process determines the disagreement between predicted map and real classified imagery. Two types of disagreement will be calculated; quantity disagreement happens when the quantity of cells of a category in the comparison map is different from the quantity of cells of the same category in the reference map and Allocation disagreement

occurs where location of a class in the comparison map is different from location of that class in the reference map (Memarian, et al., 2012) (Pontius, et al., 2011).

Equations below as shown in (Pontius, et al., 2011) illustrate these two parameters where J refers to the number of categories and number of strata - classes - in a typical stratified sampling design. Each category in the comparison map is indexed by *i*, which ranges from 1 to *J*. The number of pixels in each stratum is denoted by N_i. Each observation is recorded based on its category in the comparison map (*i*) and the reference map (*j*). The number of these observations is summed as the entry n_{ij} in row *i* and column *j* of the contingency matrix (Memarian, et al., 2012).

Proportion of the study area (P_{ij}) that is category *i* in the comparison map and category *j* in the reference map is estimated by equation 2-8.

$$\boldsymbol{P_{ij} = \left(\frac{n_{ij}}{\sum_{j=1}^{j} n_{ij}}\right)\left(\frac{N_i}{\sum_{i=1}^{j} N_i}\right)} \qquad \textbf{Equation 2-8}$$

Quantity disagreement (q_g) has been calculated for an arbitrary category g using equation 2-9.

$$\boldsymbol{q_g = \left|\left(\sum_{i=1}^{J} p_{ig}\right) - \left(\sum_{j=1}^{J} p_{ig}\right)\right|} \qquad \textbf{Equation 2-9}$$

Equation 2-10 calculates the overall quantity disagreement (Q) which incorporates all J categories.

$$\boldsymbol{Q = \frac{\sum_{g=1}^{J} q_g}{2}} \qquad \textbf{Equation 2-10}$$

Allocation disagreement (a_g) for an arbitrary category g is calculated using Equation 2-11. The first argument within minimum function is the omission of category g while the second argument is the commission of category g.

Where: a pixel is called omission for a class, when the pixel in the reference map is the same of that class and it is a different class in the comparison map. A pixel is called commission for a class, when the pixel in the comparison map is the same of that class and it is a different class in the reference map.

$$\boldsymbol{a_g = 2min\left[\left(\sum_{i=1}^{J} p_{ig}\right) - p_{gg}, \left(\sum_{j=1}^{J} p_{gj}\right) - p_{gg}\right]} \qquad \textbf{Equation 2-11}$$

The overall allocation disagreement (A) is computed by equation 2-12.

$$A = \frac{\sum_{g=1}^{j} a_g}{2} \qquad \text{Equation 2-12}$$

The proportion of agreement (C) is estimated by Equation 2-13.

$$C = \sum_{j=1}^{J} p_{jj} \qquad \text{Equation 2-13}$$

The total disagreement (D) is the sum of overall quantity of disagreement and overall allocation of disagreement as illustrated in equation 2-14.

$$D = 1 - C = Q + A \qquad \text{Equation 2-14}$$

IDRISI gives also the standard Kappa Index of Agreement (KIA) and some more useful variations on the KIA. KIA is denoted also by $K_{standard}$. Both the percent correct and the standard KIA confound disagreement of quantity with disagreement of location (Eastman, 2012). The standard Kappa can be initially appealing to many authors because Kappa is usually defined in the literature as an index of agreement that accounts for the agreement due to chance, meaning that Kappa compares the observed accuracy of the classification to the expected accuracy of a classification that is generated randomly. However, this definition is only partially true, and this imprecise definition has caused tremendous confusion in the profession. A more complete description is that the standard Kappa is an index of agreement that attempts to account for the expected agreement due to random spatial reallocation of the categories in the comparison map, given the proportions of the categories in the comparison and reference maps, regardless of the size of the quantity disagreement (Pontius, et al., 2011). Thus, in addition to calculating the standard KIA, IDRISI offers three more statistics:

1. Kappa for no information (denoted K_{no}),
2. Kappa for grid-cell level location which illustrates how well the grid cells are located on the landscape (denoted $K_{location}$), and
3. Kappa for stratum-level location which indicates how well the grid cells are located within the strata (denoted $K_{location\ Strata}$).

Pontius et al. (2011) explains that the motivation to derive Kappa for no information is that J is the statistically expected overall agreement when both the quantity and allocation of categories in the comparison map are selected randomly while $K_{location}$ is an index of pure allocation where 1 indicates optimal spatial allocation as constrained by the observed proportions of the categories, and 0 indicates that the observed overall agreement is equal the agreement expected under random spatial reallocation within the comparison map given the proportions of the categories in the comparison and reference maps .

Each Kappa is an index that attempts to describe the observed agreement between the comparison map and the reference map on a scale where 1 means that the agreement is perfect and 0 means that the observed agreement is equivalent to the statistically expected random agreement. Some Kappa indices accomplish this goal better than others.

Another term is offered by IDRISI, the disagreement at the grid cell level which is the amount of disagreement associated with the fact that the comparison map fails to specify perfectly the correct locations of categories at grid cells within strata. In other words, if we were to rearrange the grid cells within each stratum of the comparison map, then we could improve the agreement between the reference map and the comparison map from M(m) to perfect stratum K(m). K(m) = 1 if and only if the proportions of each category in each stratum in the comparison map are the same as the proportions in the reference map.

2.13 Previous Studies about the Dead Sea Area

Different studies states that the water level of the Dead Sea is dropping by an average of 90 cm per year. (Al-Zubaidy, et al., 2011)

ARAV et al. (2012) explains that the Dead Sea level has been dropping in a rate of one meter per year and higher as a combination of human and climate induced effect on the water balance in the lake. As a consequence, collapse sinkholes have began appearing and new stream channels have been forming in the alluvial fans along its shores. The study describes a methodology which is based on application of airborne laser-scanning technology.

Abu Ghazleh et al. (2010) illustrate that the Dead Sea has been experiencing a severe drop in level since 1978 with an average of 0.7 m/yr due to the accelerating water consumption in its catchment and stood in 2008 at -420 m. In this study, a terrain model of the surface area and water volume of the Dead Sea was developed from the SRTM data using ArcGIS. The model shows that the lake shrinks on average by 4 km^2/yr in area.

Bowman et al. (2010) disuses that the Dead Sea delineates during its continuous level drop a different mode of adjustment from those previously conceptualized. The study has recorded the entrenchment rates of channels and their transient shape evolution “at a station” in real time, i.e., during the ongoing base-level fall. Mean vertical entrenchment rates are very high, 0.4–0.8 m/y, and widening rates are even higher (2.1–24 m/y). Elevation-change detection maps ASTGTM-DEM on strata along banks a patchy pattern of channel entrenchment, indicating the initial widening stage. The incised channels have a trapezoidal, gorge-like, cross-sectional form the continuous and rapid lowering of the Dead Sea level entraps the drainage systems in the vertical incision

mode, preventing the evolutionary progression toward a wide, graded, and stable geometry which has been conceptualized in existing models.

Khlaifat et al. (2010) collects brine samples, Four times a month, from the Arab Potash Company (APC) point of intake and analyzed for physico-chemical parameters in the laboratory over 22 years, and Dead Sea surface temperature and level were measured during each sampling. The mean density values for the collected samples during the last 22 years ranged from 1.2040 g/cm3 in 1992 to 1.2393 g/cm3 in 2007, with an average value of 1.2376 g/cm3. The brine salinity values ranged from 293.6 in 1992 to 339.3 g/l in 2008 with an average value of 337.73 g/l. The ionic dominance observed was $Cl^{-}NMg^{++}NNa^{+}NCa^{++}NK^{+}$. The results showed that diluting the Dead Sea brine affects both magnesium and sodium chlorides significantly because of their high solubility in fresh water and their large reserves.

In conclusion, previous studies state that the Dead Sea is decreasing in area and water level.

CHAPTER 3

3 The Study Area

3.1 Scope

This chapter consists of five sections. It involves location and geography which discusses the position of the study area according to WGS84 coordinate system. Dead Sea Area hydrology is then reviewed temporally and quantitatively. After that, a geological back ground is discussed in the third section. Finally, the political and economical issues which affect the Dead Sea Area have been discussed in the last two sections.

3.2 Location and Geography

The Dead Sea is located on 31° 30′ 0″ N, 35° 30′ 0″ E, WGS84 coordinate system, bordering Jordan to the east, historical Palestine and the West Bank to the west as illustrated in Figure 3-1. The Dead Sea is considered as the lowest point on the Earth's surface at about -400 m (Morin, et al., 2009). The east and west shores of the Dead Sea are bounded by towering fault escarpments that form part of the African-Syrian rift system. The valley slopes gently upward to the north along the Jordan River, and to the south along the Wadi Araba. Since 1978, the Dead Sea has retreated, and the sea body turned into two basins: the principal northern one that is about 308 m deep (in 1997), and the shallow southern one with the Lisan (or Lashon) Peninsula and the Lynch Straits in between, which has a sill elevation of about 400 m below the sea level. (U.S. Geological Survey, 1998).

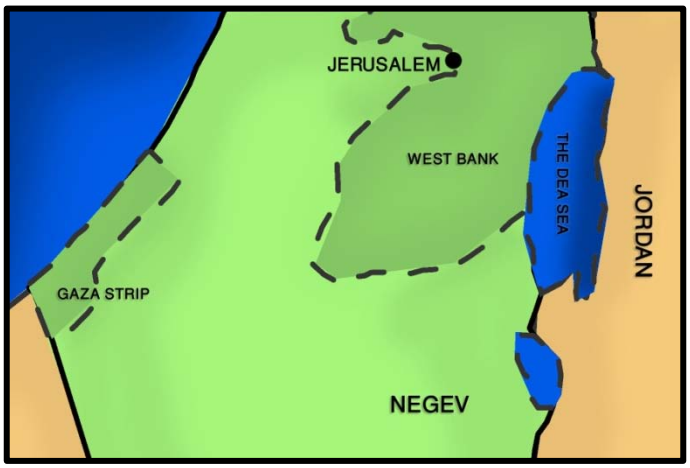

Figure 3-1 Dead Sea location

3.3 Hydrology

3.3.1 Temperature

The Dead Sea's area average temperature varies from 12°C in winter to 40°C in summer reches the maximum in July while in January, it reaches the minimum value (see Figure 3-2). The sea affects temperature nearby because of the moderating effect a large body

of water has on climate. During the winter, sea temperature tend to be higher than land temperature, and vice versa during the summer months. This is the result of the water's mass and specific heat capacity. On average, there are 192 days above 30°C. (U.S. Geological Survey, 1998). The evaporation in the Dead Sea Area ranges from about 970 to 1360 mm with an annual average evaporation rate estimation is about 1150 mm/yr (Dead Sea Research Team, 2011) .

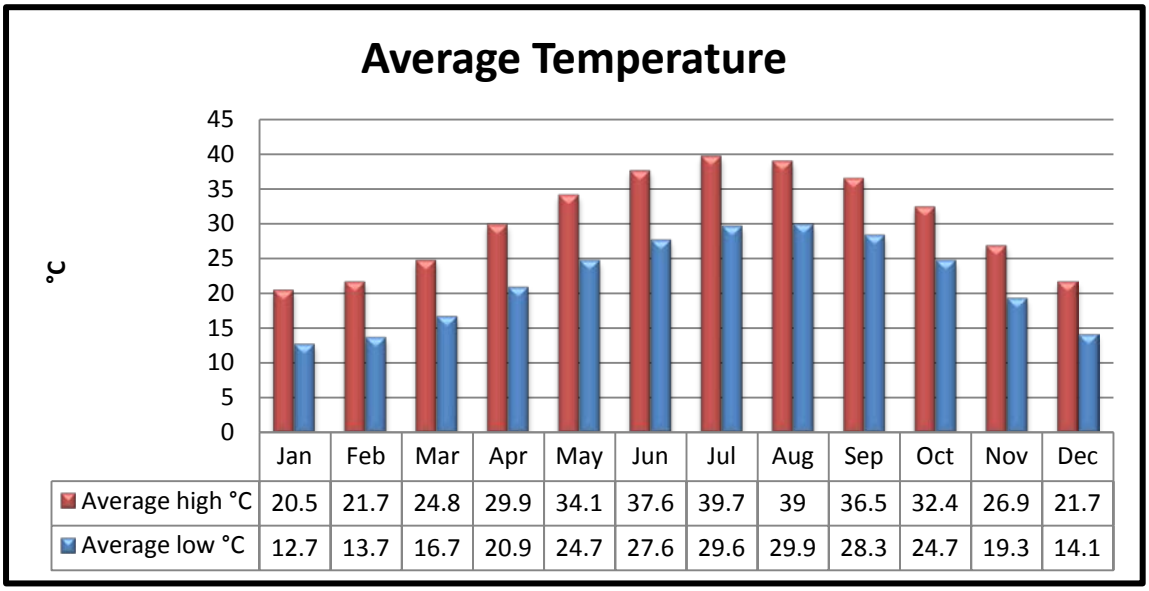

	Jan	Feb	Mar	Apr	May	Jun	Jul	Aug	Sep	Oct	Nov	Dec
Average high °C	20.5	21.7	24.8	29.9	34.1	37.6	39.7	39	36.5	32.4	26.9	21.7
Average low °C	12.7	13.7	16.7	20.9	24.7	27.6	29.6	29.9	28.3	24.7	19.3	14.1

Figure 3-2 The average temperature on the Dead Sea Area (Israel Meteorological Service, 2011) modified

3.3.2 Rainfall

Figure 3-3 illustrates the average rainfall on the Dead Sea Area. The rate of rainfall is less than 5 cm; most of the water flowing to the Dead Sea comes from the relatively high rainfall areas of the Jordan River watershed to the north, and the rift valley escarpments to the east and west of the Dead Sea.

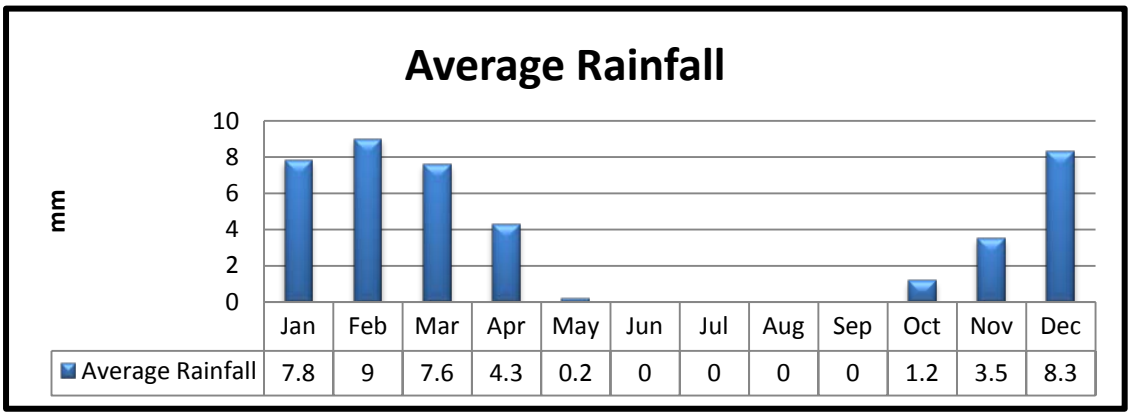

	Jan	Feb	Mar	Apr	May	Jun	Jul	Aug	Sep	Oct	Nov	Dec
Average Rainfall	7.8	9	7.6	4.3	0.2	0	0	0	0	1.2	3.5	8.3

Figure 3-3 The average rainfall on the Dead Sea Area (Israel Meteorological Service, 2011) modified.

To the south, the Wadi Araba watershed covers the arid regions of the Negev and South Jordan Desert. (U.S. Geological Survey, 1998)

3.3.3 Dead Sea Water Level

The water level of the Dead Sea has a seasonal cycle. Prior to development of water resources in the watershed, the peak water level occurred in May and the low occurred in December. Within-year variation ranges from 0.3 to 1.2 m for most of the period of record as shown in Figure 3-4.

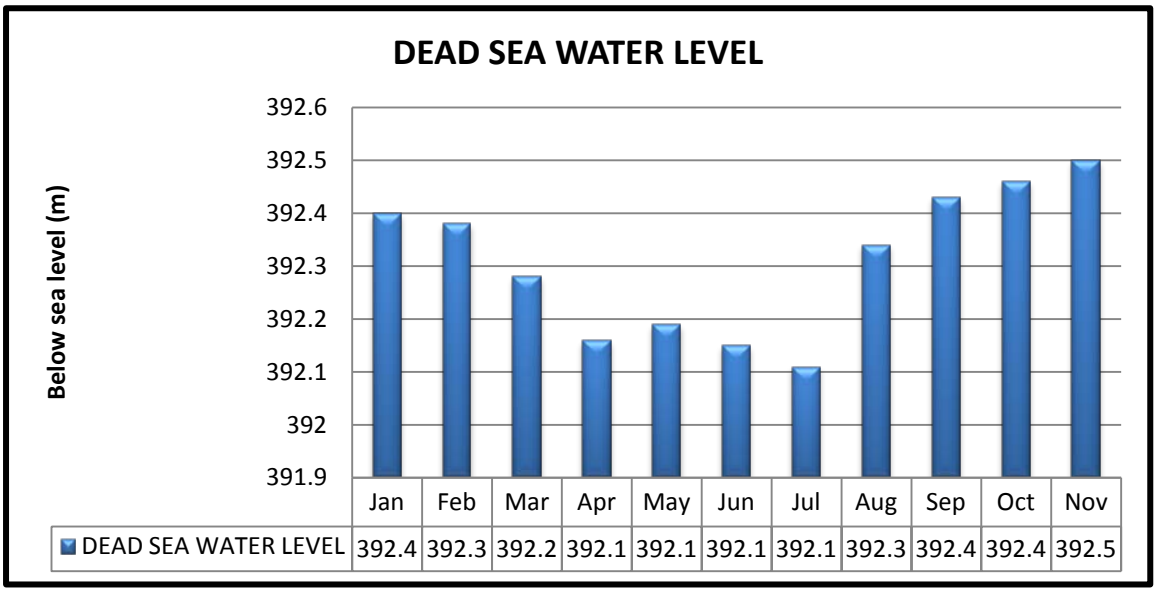

Figure 3-4 The average Dead Sea water level (U.S. Geological Survey, 1998) modified.

3.3.4 The Change of the Dead Sea Hydrological Parameters over Time

3.3.4.1 Historical Water Level

U.S. Geological Survey (1998) shows that the historical range of water level fluctuations is about 83 m (see Figures 3-5 and 3-6). The largest change in water level shown on the estimated historical hydrograph occurred between about 100 B.C. and A.D. 40. Within this period, the water level of the Dead Sea rose approximately 70 m, from about 400 m to about 330 m below sea level in 67 years; and subsequently fell nearly 65 m in about 66 years.

Figures 3-5 and 3-6 show that in the recent decades, the severe drop in level is in 1955 while (Abu Ghazleh, et al., 2010) discussed that the Dead Sea has been experiencing a severe drop in level since 1978 with an average of 0.7 m/yr due to the accelerating water consumption in its catchment and stood in 2008 at -420 m.

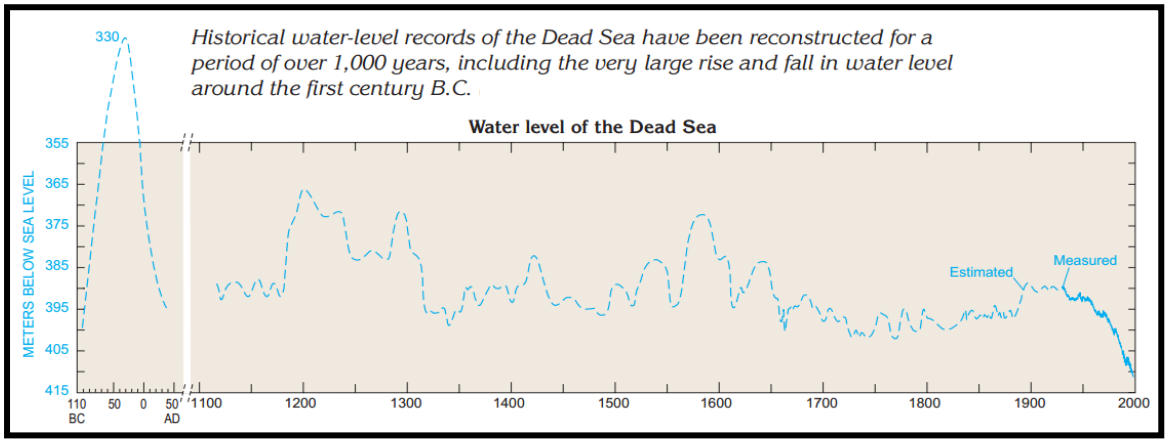

Figure 3-6 Historical Water level of the Dead Sea Area (U.S. Geological Survey, 1998)

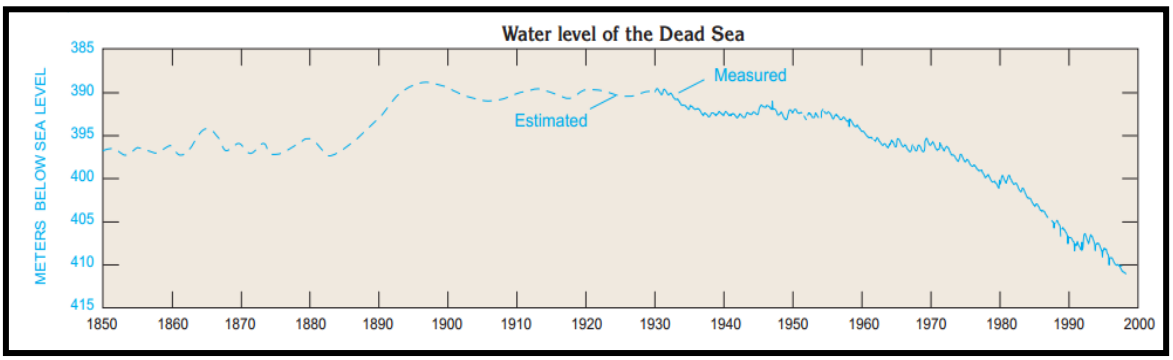

Figure 3-5 Recent water level of the Dead Sea Area (U.S. Geological Survey, 1998)

3.3.4.2 Recent Water Level

Dead Sea Research Team (2011) lists the water level from 1999 to 2009. As shown in Figure 3-7, from 1992 till 2009 the water dropped by 13.7 m which means 0.76 m/yr.

3.3.4.3 The Total Inflow of the Dead Sea

The annual total inflows of the Dead Sea are presented by the Dead Sea Research Team (2011) in Figure 3-8 for the years of 1992-2009. However, the team states that the total inflow is influenced by the uncertainty of the following components:

- Evaporation uncertainty is approximately ±126 MCM/yr.
- Estimations of the net deficit by the chemical industries Dead sea works (DSW) & Arab Potash Company (APC) vary by approximately 100 MCM/yr, ranging from 385 (642-257) MCM/yr, to 280 (520-240) MCM/yr.

3.3.4.4 The Evaporation of the Dead Sea

The Evaporation of the Dead Sea is presented annually in Figure 3-9 for the years of 1992-2009. It is obvious that the average evaporation is about 1.2 m/yr with a peak in 2006 (Dead Sea Research Team, 2011).

3.4 Geology

3.4.1 The Dead Sea Transform Fault Zone

This fault which runs through the Dead Sea region is a left-lateral strike-slip fault, which is a fault where movement is mostly horizontal and parallel to the strike. When a strike-slip fault is left-lateral, such as in the case of the Dead Sea fault, visible features such as hills and streams are displaced to the left. This is evident in many areas of the Dead Sea region. The slip rate, or rate of movement along the fault ranges from 1-10 mm annually. The fault connects the diverging plate boundary in the Red Sea to the Taurus converging plate boundary in the north, between Turkey and Syria, and runs along the Araba Valley, a 160 km stretch from the Dead Sea to the Gulf of Aqaba. The Dead Sea fault has been the source of several large historical earthquakes, but has not produced many recently, with the last major one being the 1995 earthquake that hit the Gulf of Aqaba and measured 7.3 on the Richter scale. In fact, there is little micro-seismicity along the fault except at the Dead Sea and Gulf of Aqaba, where the fault forms into complex pull-apart basin fault systems. The Dead Sea itself is surrounded by faults, which border its eastern, western, and southern shorelines. On the western shore there is a fault zone that runs parallel to the main fault, along which there are horsts and grabens. Geologists predict that given the slip rate, the Dead Sea fault running through the Araba Valley should trigger 7.0 earthquakes every 200 years (Agnew, 2005).

3.4.2 Dead Sea Graben and Geological History

As with many things in history, geological or otherwise, the Dead Sea didn't just happen overnight. It took several million years before it formed into its current state. It likely began its formation millions of years ago when activity at the boundary between the Sinai sub-plate and the Arabian plate caused major upheavals of the Mediterranean seabed, which covered most of modern-day Israel at the time. Between these two plates a block of crust sank, forming a graben. As the Mediterranean evaporated some water was retained in the graben, creating a series of lakes in the graben that disappeared and reappeared as a result of climatic changes in the area. The last of these lakes, Lake Lisan, which stretched from the northern portion of the Araba Valley to the Sea of Galilee, eventually dried up 15000 years ago leaving behind the current Dead Sea (Agnew, 2005).

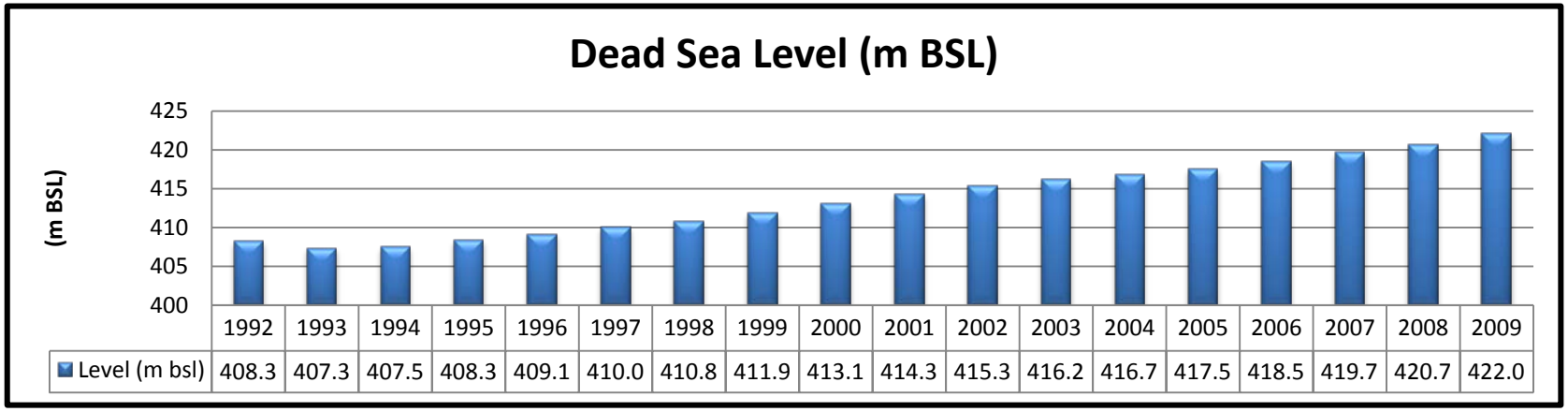

Figure 3-7 Dead Sea Level (Dead Sea Research Team, 2011), modified

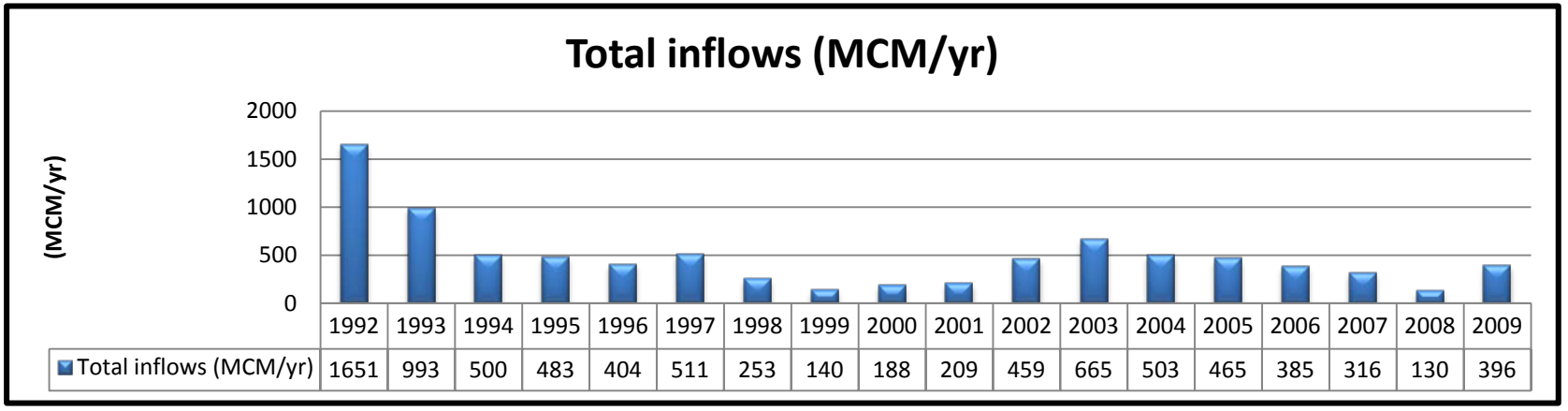

Figure 3-8 Dead Sea total inflow (Dead Sea Research Team, 2011), modified

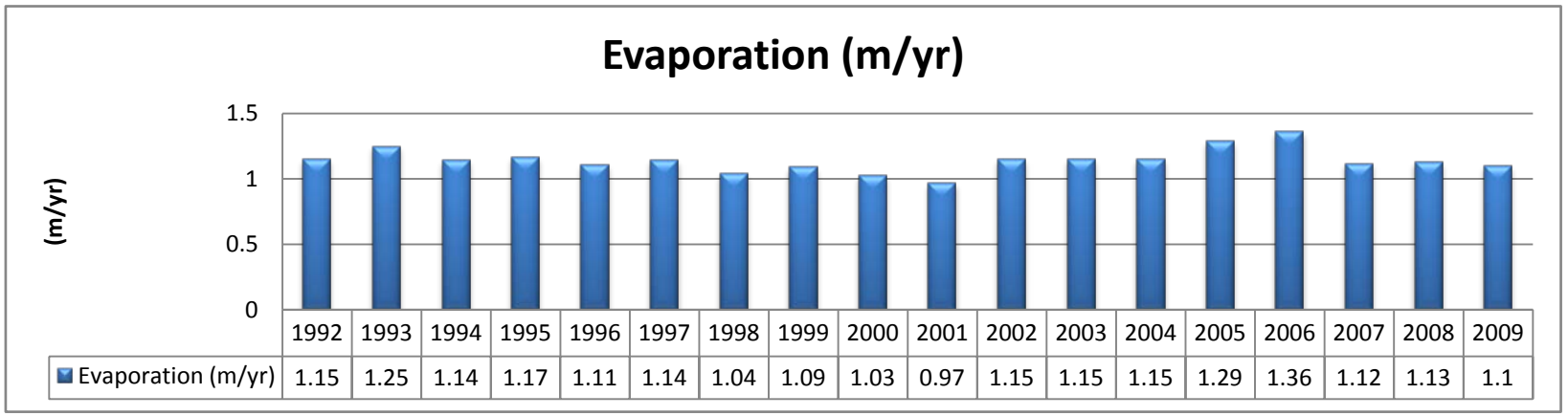

Figure 3-9 Average evaporation in the Dead Sea area (Dead Sea Research Team, 2011), modified

3.5 Dead Sea and Economic

Dead Sea today is considered as a major source of various mineral essential for agricultural and industrial development. The salty water and the black mud of the sea are used for various medical treatments. The Dead Sea is also famous for their restorative powers and the thermal mineral springs of Zarqa Ma'een. The therapeutic health spa is located there. Along with being one of the most visited tourist attractions of the country the Dead Sea is also well known for its religious reference (Maps of tha world, 2010).

Agnew (2005) explains that the northern basin has remained mostly untouched by industry and has been primarily set aside for tourist use, the southern basin, which is shallow and extremely rich in minerals, is being tapped for its mineral resources. The two major companies involved in mineral extraction at the southern basin are the DSW and APC. The DSW is the world's fourth largest producer and supplier of potash products, as well as other chemical products such as magnesium chloride, industrial salts, deicers, bath salts and table salts, and raw materials for the cosmetics industry. They use a very unique method to take potash and other minerals from the Dead Sea. Rather than mining them, DSW harnesses the solar energy that evaporates the water in the Dead Sea by constructing evaporation ponds, two meter deep ponds that crisscross the mining area to aide in extracting pure potash and other minerals. However, despite the great profit being generated from mineral extraction in the Dead Sea, some fear that potash production will upset the environmental stability of the area by emitting dust, carbon dioxide, sulphur dioxide, and carbon monoxide into the air, as well as by producing ozone-depleting methyl-bromide.

3.6 The Dead Sea and Politics

Asmar (2003) discusses that the decline in the level of the Dead Sea is generating considerable media, government, and NGO attention. Constructing a pipeline to link the Red Sea to the Dead Sea is one in a series of proposals to solve the problem. It is known that the scientific community agrees unanimously that the Dead Sea will not dry up, and a pipeline can restore the level of the Dead Sea, although not its previous water characteristics. A solution is certainly required, but more research is needed, and there is no immediate urgency to act. The media attitude of exaggerating the scale of the problem and urgency to act is not based on any credible scientific facts and is mainly politically motivated.

CHAPTER 4

4 Methodology

4.1 Scope

In this chapter, methodology framework is described in details. Then data collection criteria is explained and justified. After that, image pre-processing and normalization of satellites imageries are illustrated. Next, supervised classification process is discussed. After that, change detection analysis is described. Finally, prediction process is explained in details.

4.2 Methodology Framework

Figure 4-1 illustrates the methodology followed in this research which consists of nine major stages;

1. Problem identification and objectives.
2. Literature review.
3. Data collection: In this stage, the data is collected based on criteria illustrated in data collection dashed block shown in Figure 4-1.
4. Pre-processing: aims to normalize all imageries by converting Digital Number (DN) to spectral radiance. Then, removing atmospheric effects. After that, converting the resulted image to reflectance. Finally removing black gaps if exist.
5. Supervised Classification.
6. Change detection analysis: In this stage, changes of the Dead Sea area, shape, water level, and volume are analyzed.
7. Data preparation for prediction: This step consists of three steps:
    a. Markov chain analysis.
    b. Data generation for Multicriteria Evaluation (MCE).
    c. Suitability map creation.
8. Prediction and validation processes.
9. Results and discussion.

In order to achieve this methodology, the following software and supporting tools are used:

- ERDAS Imagine 10: Used for image pre-processing and normalization, supervised classification and bathymetric map creation.
- ArcGIS 9.3: Used for spatio-temporal analysis, building models for area, water level change analysis and Multicriteria Evaluation, calculating spatial parameters and cartographical representation.

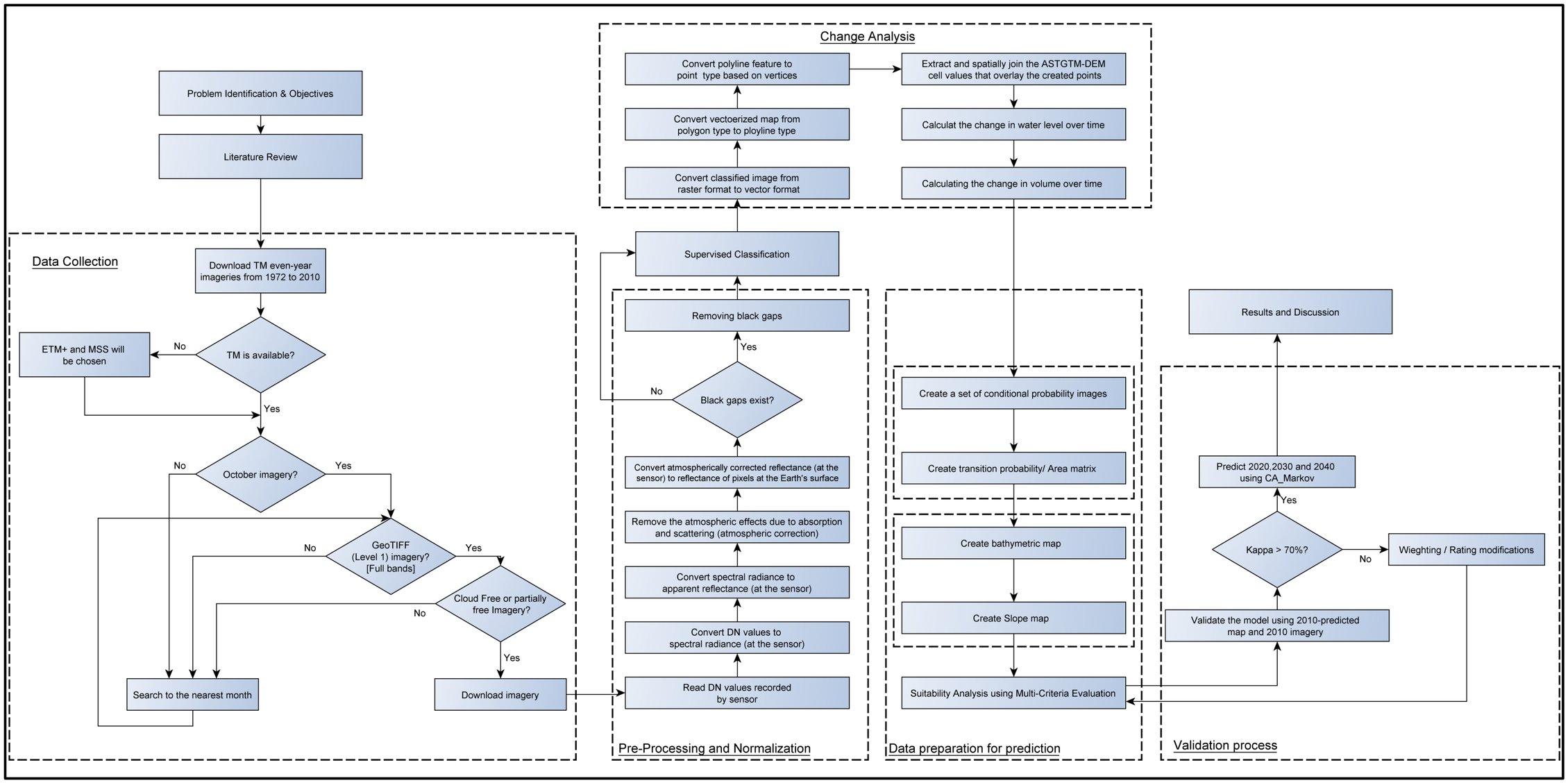

Figure 4-1 The methodology followed by the researcher

- IDRISI Selva: Used for Markov Cellular Automata prediction analysis and validation process.
- MS Excel: Used for chart representation.

4.3 Data Collection

In this research, the Advanced Spaceborne Thermal Emission and Reflection Radiometer Global Digital Elevation Model (ASTGTM-DEM) for 2011 is downloaded from U.S. Geological Survey (USGS) website. The rest of the data is mainly Landsat remotely sensed imageries downloaded also from USGS website – Landsat archive from 1972 to 2010. Figure 4-1, data collection dashed block, illustrates the criteria followed in this stage.

The first criterion in data collection is to download even-year imageries including the oldest and newest Landsat archived imageries, 1972 and 2010. The second criterion is to give TM imagery a priority over ETM+ and/or MSS since TM sensor life span is longer than ETM+ (approx. 20 years) so consistent data will be collected. In contrast, Landsat ETM+ imageries have the problem of the Scan Line Corrector Failure (SLC-off) which presented in black gaps. Moreover, Landsat ETM+ has the only advantage of the panchromatic band existence. However, the resolution in the multispectral bands in ETM+ is the same of TM, 30 m. The third criterion is reducing the pre-processing by downloading all imageries in the same date, month of October is chosen to avoid clouds in the scene. In case of October imagery does not match the listed criteria, the closest imagery to October matching the listed criteria will be downloaded. The fourth criterion is downloading a full-bands imagery in a Geostationary Earth Orbit Tagged Image File Format (GeoTIFF). In case of GeoTIFF does not available, the closest imagery to October matching the listed criteria will be downloaded. The fifth criterion is downloading free clouds scenes, at least above the water-body. In case of cloud existence above the water-body, the closest imagery to October matching the listed criteria will be downloaded.

Based on these criteria, fourteen imageries are downloaded as illustrated in Table 4-1. The only exception is 1975 imagery which is an odd-year and it is preferred to be used because of the lack of satellite imageries from 1973 to 1983.

Table 4-1 Imagery data set used in this research

Year	Imagery type	Year	Imagery type	Year	Imagery type
Sep 15, 1972	MSS	Aug 30, 1990	TM	Jun 17, 2004	ETM+
Jun 29, 1975	MSS	Aug 3, 1992	TM	Oct 13, 2006	ETM+
Sep 06, 1984	TM	Oct 15, 1998	TM	Oct 18, 2008	ETM+
Sep 28, 1986	TM	Oct 04, 2000	TM	Dec 03, 2010	TM
Dec 30, 1988	TM	Oct 18, 2002	TM		

4.4 Image Pre-Processing and Normalization

Since digital sensors record the intensity of electromagnetic radiation from each spot viewed on the Earth's surface as a Digital Number (DN) for each spectral band, the exact range of DN that a sensor utilizes depends on its radiometric resolution. For example, a sensor such as Landsat MSS measures radiation on a 0-63 DN scale even as Landsat TM and ETM+ measure it on a 0-255 scale (Green, et al., 2000). Therefore, normalizing image pixel values for differences in sun illumination geometry, atmospheric effects and instrument calibration is necessary specially because a time series of Landsat imageries will be used, from 1972 to 2010 (MSS, TM and ETM+), and compared to each other. The radiometric correction was used to restore the image by using sensor calibration concerned with ensuring uniformity of output across the face of the image, and across time. Figure 4-2 lists the steps followed to accomplish this stage.

In the first step, radiance calibration is used to convert DN to absolute radiance values that are important for comparative analysis of several images taken by different sensors (MSS, TM and ETM+ imagery). Then, removing atmospheric effects is done using Dark Object Subtraction (DOS) technique which removes the effects of scattering from the image data. DOS technique assumes that there are pixels within each band of a multispectral image that have very low or no reflectance (as a deep water-body), and that the difference between the brightness value of these pixels and zero is due to haze and atmospheric scattering (Tyagi, et al., 2011). Next, converting the atmospherically corrected reflectance (at the sensor) to reflectance of pixels at the Earth's surface is done.

Using the Cosine of the Solar Zenith Angle (COST) method, the DN transformed to reflectance as discussed above. Atmospheric correction using DOS is also included in the Chavez (1996) COST method (Chavez, 1996) (Wen, 2008) (Ramsey, 2010) (Irons, 2011) (Green, et al., 2000). Ramsey (2010) illustrates Chavez (1996) method in one equation as illustrated in equation 4-1.

Using ERDAS Imagine, a model has been built by the researcher, see Figure 4-3, the model consist of the three operations listed above, presented as circles, since DOS stage and converting to earth reflectance stage are merged in one operation. This model is built in order to make the correction process easier and less time consuming sense this correction will be run for fourteen imageries each consists of several bands.

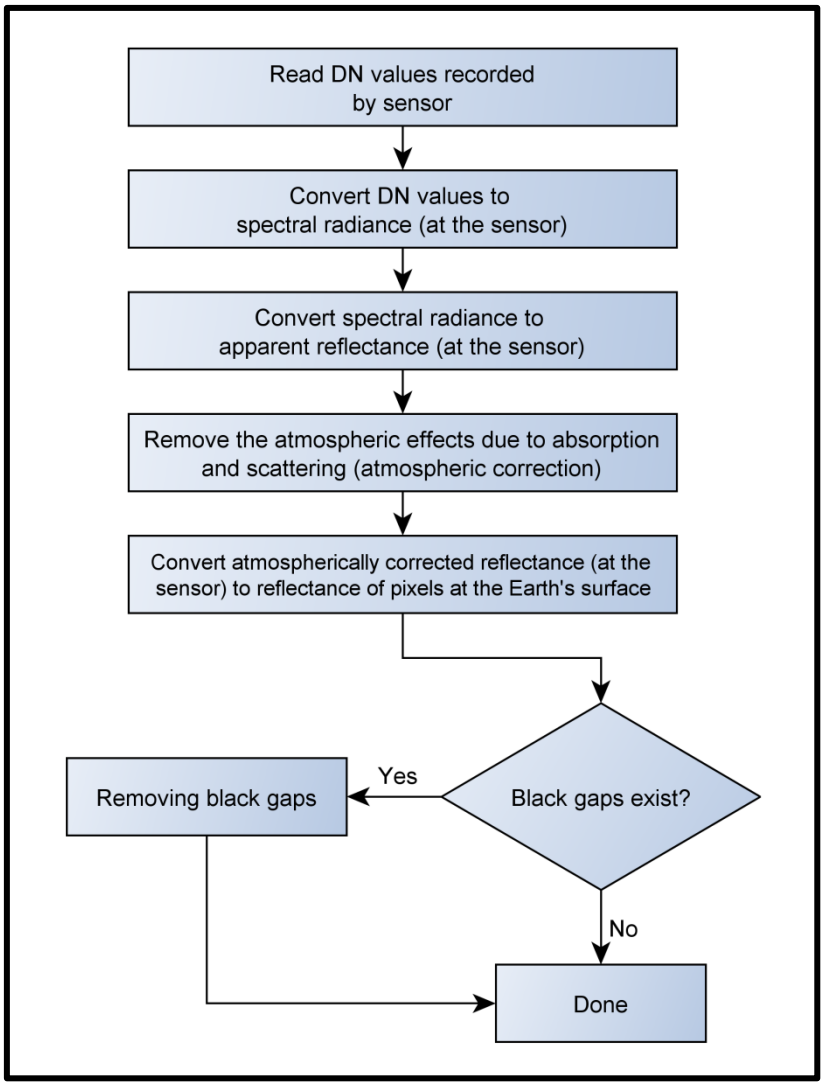

Figure 4-2 Image pre-processing and normalization process

$$\rho_{Band\ N} = \frac{\pi((L_{band\ N} \times Gain_{band\ N} + Bias_{band\ N}) - (H_{band\ N} \times Gain_{band\ N} + Bais_{band\ N})) \times D^2}{E_{band\ N} \times (COS((90 - \theta) \times \frac{\pi}{180}))}$$

Equation (4-1)

Where:

$\rho_{Band\ N}$ = Reflectance for Band N.

$Gain_{bandN} = \frac{L_{max\ \lambda}}{254} - \frac{L_{min\ \lambda}}{255}$.

$Bais_{bandN} = L_{min\ \lambda}$.

$L_{max\ \lambda}$: The spectral radiance that is scaled to (QCALMAX=255), watts × (m^2 * ster * µm) $^{-1}$.

$L_{min\ \lambda}$: The spectral radiance that is scaled to (QCALMIN=254), watts × (m^2 * ster * µm) $^{-1}$.

$L_{band\ N}$ = Digital Number for Band N.
$H_{band\ N}$ = Digital Number representing Dark Object for Band N.
$E_{band\ N}$ = Solar Irradiance for Band N, watts/ (m^2 * μ).
θ = Sun Azimuth.
D' =Normalized Earth-Sun distance, see equation 4-2.

$$D'^2 = (1 - 0.01674\,COS\,(0.9856\,(JD - 4)))^2 \qquad \text{Equation 4-2}$$

Where JD is the Julian Day (day number of the year) of the image acquisition.

For instance, the tables below are the charactrestics of ETM+ 7 and 2006-2008 imageries respectivily.

Table 4-2 ETM+ 7 characteristics used for image pre-processing and normalization

Band #	L_{max_λ}	L_{min_λ}	$H_{band\ N}$	$E_{band\ N}$
	watts/(meter squared * ster * μm)			watts/(meter squared * μm)
1	293.7	-6.2	44	1997
2	300.9	-6.4	28	1812
3	234.4	-5	19	1533
4	241.1	-5.1	11	1039
5	47.57	-1	6	230.8
7	16.57	-0.35	5	84.90
8	243.1	-4.7	13	1362

Table 4-3 2006 and 2008 Landsat imagery characteristics

	Day	θ	D (Irons, 2011)
2006	Oct 13, 2006	149.2817	0.997752
2008	Oct 18, 2008	150.6524	0.996050

Finally, removing black gaps in ETM+ since Landsat 7 ETM+ downloaded imageries (from 2004 to 2008) are SLC-off data (contains black gaps, DN=0). This type of gaps has been minimized by taking two ETM+ scenes, radiometrically corrected, and then combines them for more complete coverage (USGS, 2008).

Another model has been built by the researcher to do this kind of correction in order to make it easier and less time consuming sense this correction will be run for three imageries (2004, 2006 and 2008) each consists of several bands.

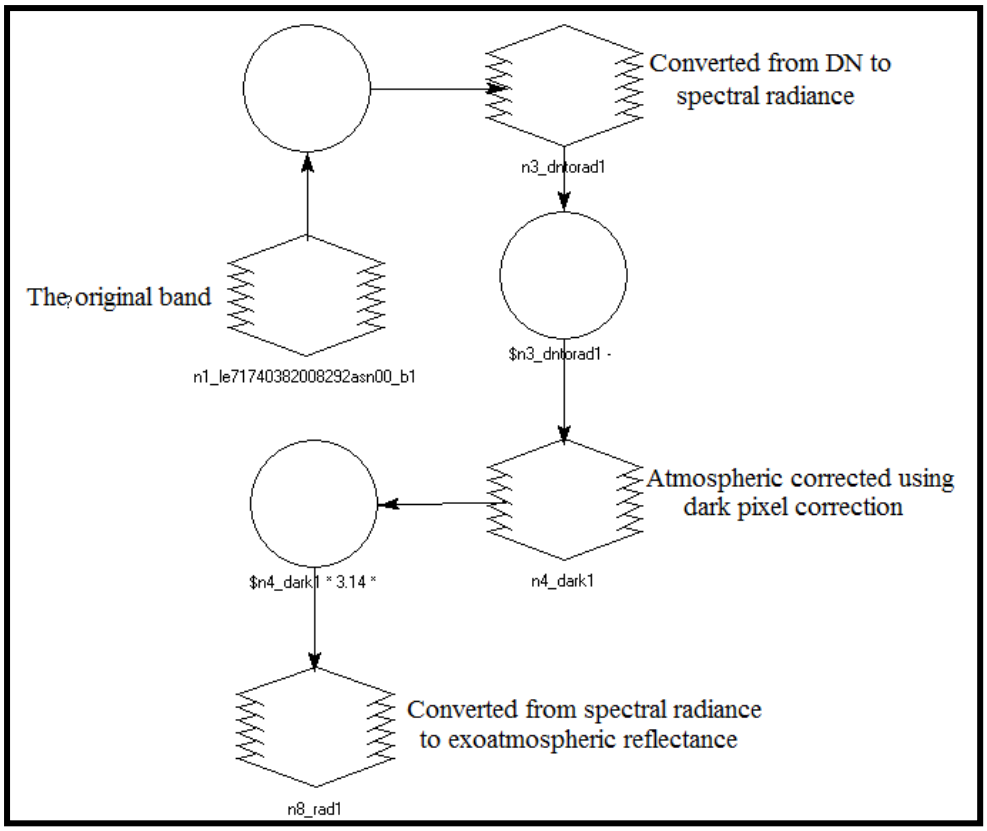

Figure 4-3 Model used for image pre-processing and Normalization

Figure 4-4 represents the model which consist two inputs (a band from each year) and one output; the merged image. The process concept of this model as illustrated in (USGS, 2008) is as follows: Where band N in image 1 > 0, use band N in image 1 data, Otherwise, use band N in image 2. In other words, Image 2 data will fill the gaps in Image 1.

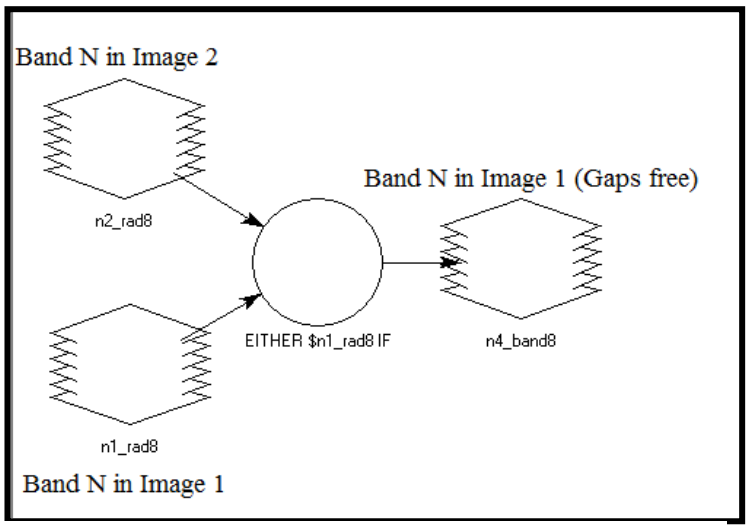

Figure 4-4 Black gaps removing model

4.5 Supervised Classification

In this research, supervised classification is used since the Areas of Interest (AOI) are known and clear to be distinguished (the water-body), so the spectral signatures of the sea body and the land around are developed and then the software assigns each pixel in the image to the type to which its signature is most similar.

Figure 4-5 summarizes the steps performed for supervised classification.

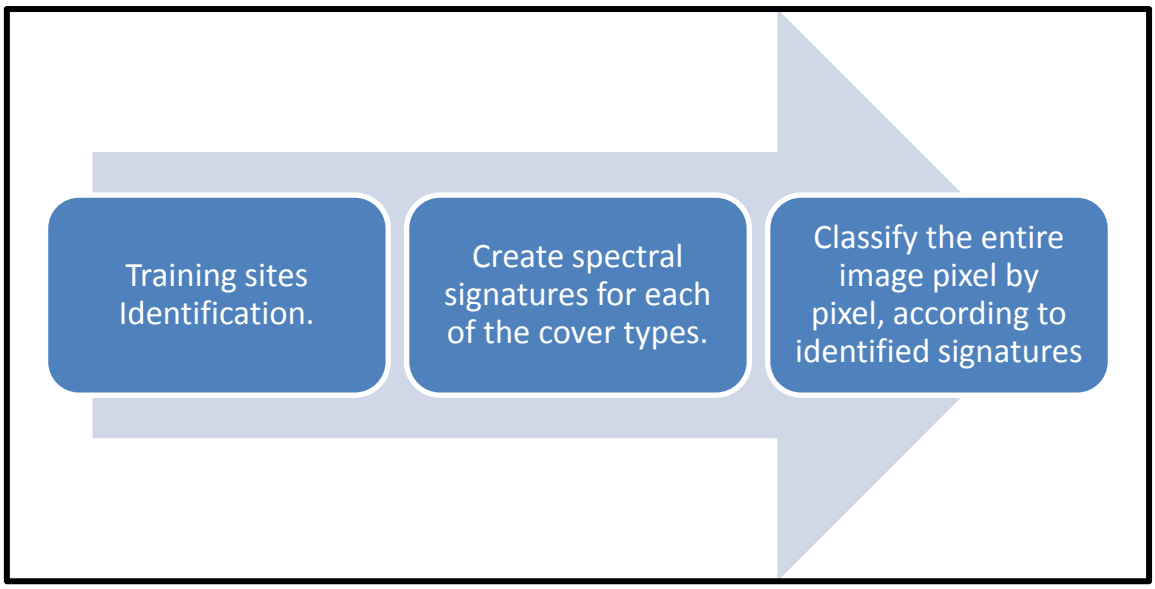

Figure 4-5 Steps for supervised classification

In order to classify the images based on these signature files. Each pixel in the study area has a value in each of the Blue, Green, Red, Near Infrared, Middle Infrared, Thermal Infrared and another Middle Infrared bands. The pixel is then assigned to the type that has the most similar signature.

In term of evaluation how similar signatures are to each other, there are several different statistical techniques that can be used; minimum distance, maximum likelihood classifier and parallelepiped classifier. In this research the Maximum Likelihood method is used since Jesús D. Chinea (2006) recommends that if your training sites are well defined – as in the Dead Sea Area- the Maximum Likelihood classifier should produce the best results. However, when training sites are not well defined, the Minimum Distance classifier with the standardized distances option often performs much better.

In The maximum likelihood classifier, the distribution of reflectance values in a training site is described by a probability density function, developed on the basis of Bayesian

statistics. This classifier evaluates the probability that a given pixel will belong to a category and classifies the pixel to the category with the highest probability of membership (Jesús D. Chinea, 2006).

Figure 4-6 illustrates infrared band values on x-axis while red band values on y-axis in a feature space layer before and after image pre-processing. That is right the signatures are well separated either after or before correction but it is obvious that land ellipse in Figure 4-6-B contains more pixels than Figure 4-6-A which means that the signature after correction is more representative than before correction. The flattening of the water point to 0 on the Y axis in Figure 4-7-B is more a function of the dark object subtraction value that is done than the conversion to reflectance.

The spikes and gaps are due to the stretching and rounding that occurs during the calculation. While it looks unusual it does not change the relative distribution of the data (Ramsey, 2010).

Figure 4-7 represents the image pre-processing and normalization, since Figure 4-7-A illustrate the DN values which will be converted to reflectance while Figure 4-7-B is the atmospherically corrected reflectance. It is noticeable that the water body get darker in the effect of DOS process and image color looks more real. However, both Figure 4-7-A and Figure 4-7-B are with black gaps. Figure 4-7-C represents the reflectance without black gaps after merging 2006 and 2008 using the built models illustrated in Figures 4-3 and 4-4.

Figure 4-8 represents the image supervised classification process which begins with identifying Area of Interests (AOI) as shown in Figure 4-8-A. Figure 4-8-B illustrates the resulted supervised classification; dark gray represents the water while light gray represents the land. It is obvious that the southern parts of the Dead Sea does not seem as smooth as the northern pars since the evaporation bonds in the south is too shallow, two meters in some places, which is detected form the Landsat satellites. Figure 4-8-C is the water body in a vector format exported to ArcGIS software to start change analysis process.

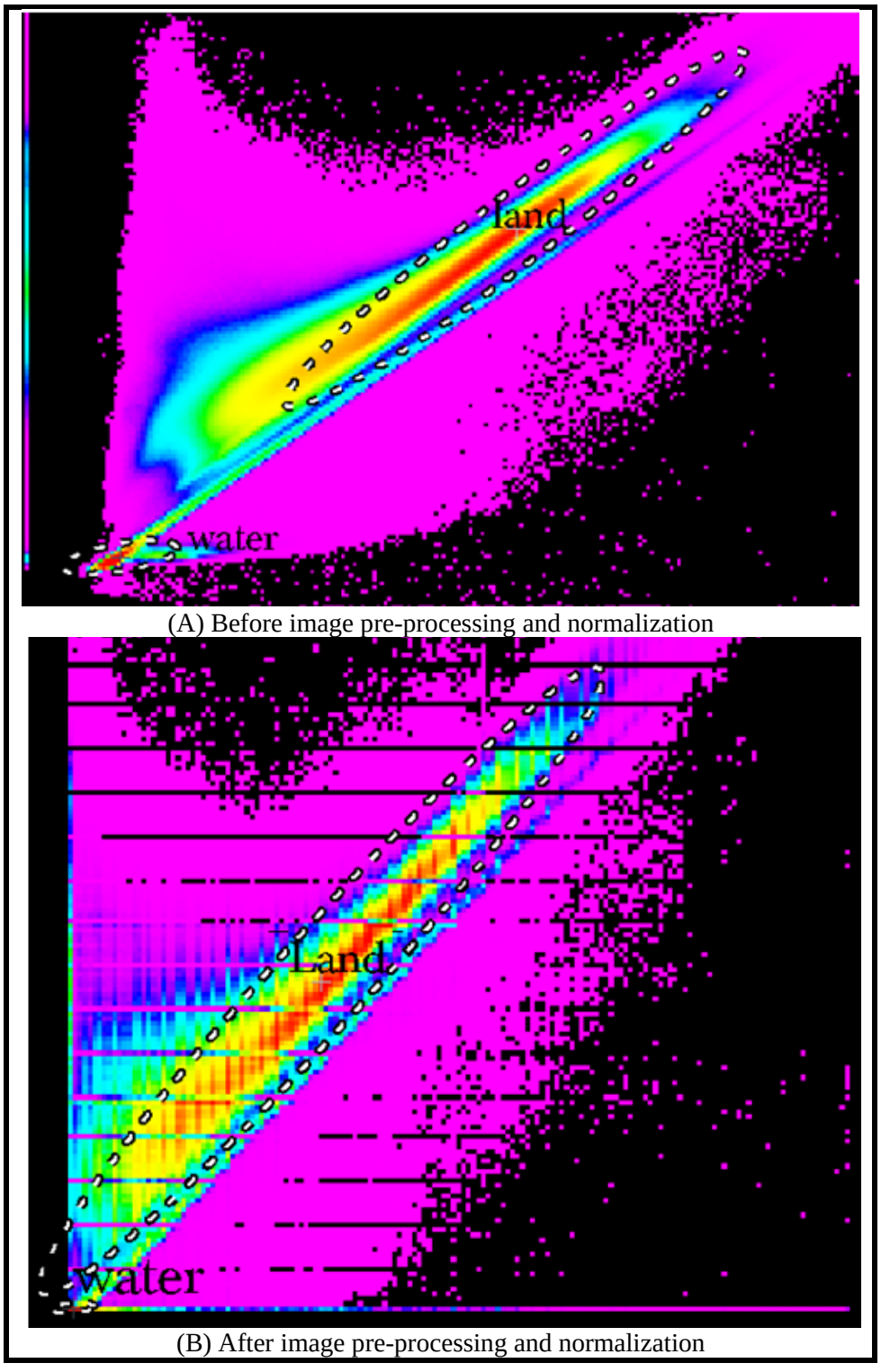

(A) Before image pre-processing and normalization

(B) After image pre-processing and normalization

Figure 4-6 Red vs. infrared bands feature space

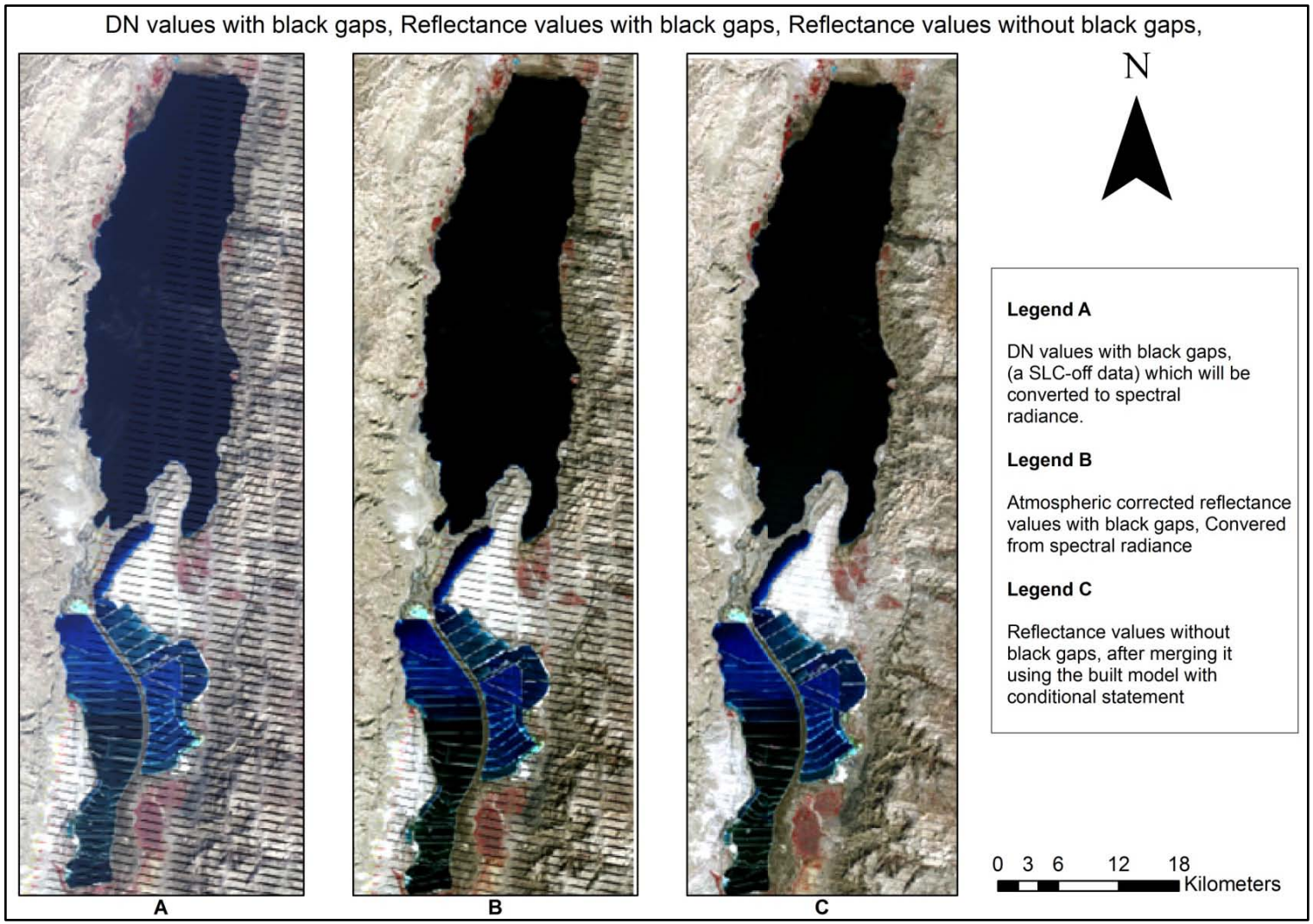

Figure 4-7 Image pre-processing

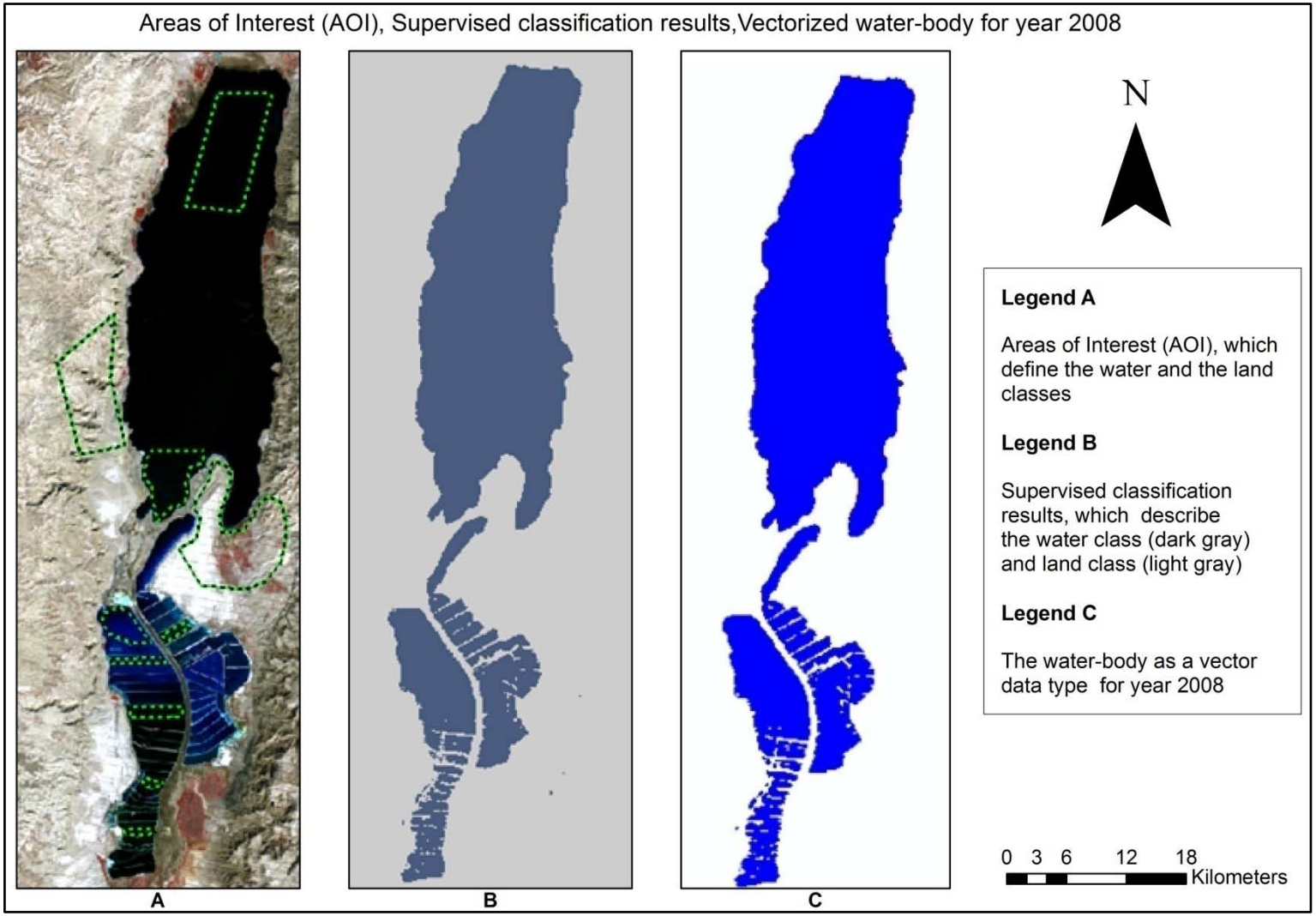

Figure 4-8 Supervised classification and victorization

4.6 Change Detection Analysis

In this stage, area, shape, water level and volume change detiction analyses are done using ArcGIS tools.

Akin et al. (2013) and Cooley (2013) describe a volume estimating method of a watershed by considering watershed as a bowl. Its volume can be found by delineating two things: a plane across its rim and its curved inner surface. A capping surface can be constructed by connecting a set of points located along the divide, while the inner surface is the modern topography represented by the ASTGTM-DEM. The volume is simply the difference between the cap elevation and topography.

In order to follow this method to calculate the volume of the Dead Sea water body, it needs some modifications since the ASTGTM-DEM does not give information about the bathymetry shape of the Dead Sea because of the water existence. Therefore, the change in volume is measured instead of measuring volume itself by using remotely sensed imageries and ASTGTM-DEM. Figure 4-9 lists the methodology followed to analyze the spatial changes over time. First of all, classified imageries will be converted from a raster to a vector format. Then, vectorized maps are converted from polygon type to polyline type in order to get the Dead Sea shoreline contour as shown in figure 4-10-B, Next, the shoreline is converted to a point type as shown in figure 4-10-C. After that, the converted points are joined spatially with ASTGTM-DEM to assign the elevation of the ASTGTM-DEM cell to that point which overlaid it. Finally, the elevation of the Dead Sea surface is calculated by averaging the assigned elevation values in a converted point layer. For example the average water level in 2008 is -431m MSL. In fact, this methodology is correct only if the ASTGTM-DEM acquisitioned in the time with the lowest water level (as the data used in this research).

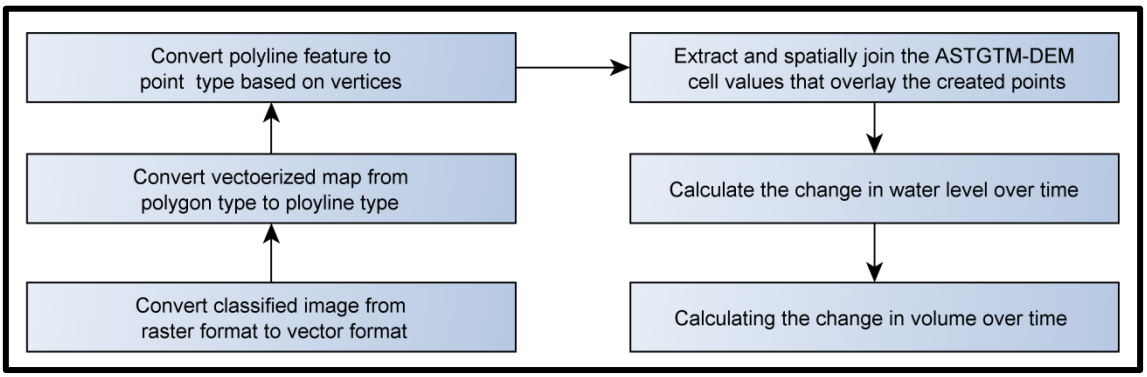

Figure 4-9 Change detection analysis steps.

Figure 4-11 illustrates change detection model which is built by the researcher using ArcGIS. The model consists of two inputs, blue ellipses, six operations, umber

rectangles and six outputs one of them is the final result, green ellipses. The inputs are the Dead Sea polygon in a vector format and ASTGTM-DEM while the operations are the tools used in converting polygon to points, spatially joining, calculating area of the water body and averaging the assigned elevation values in a converted point layer.

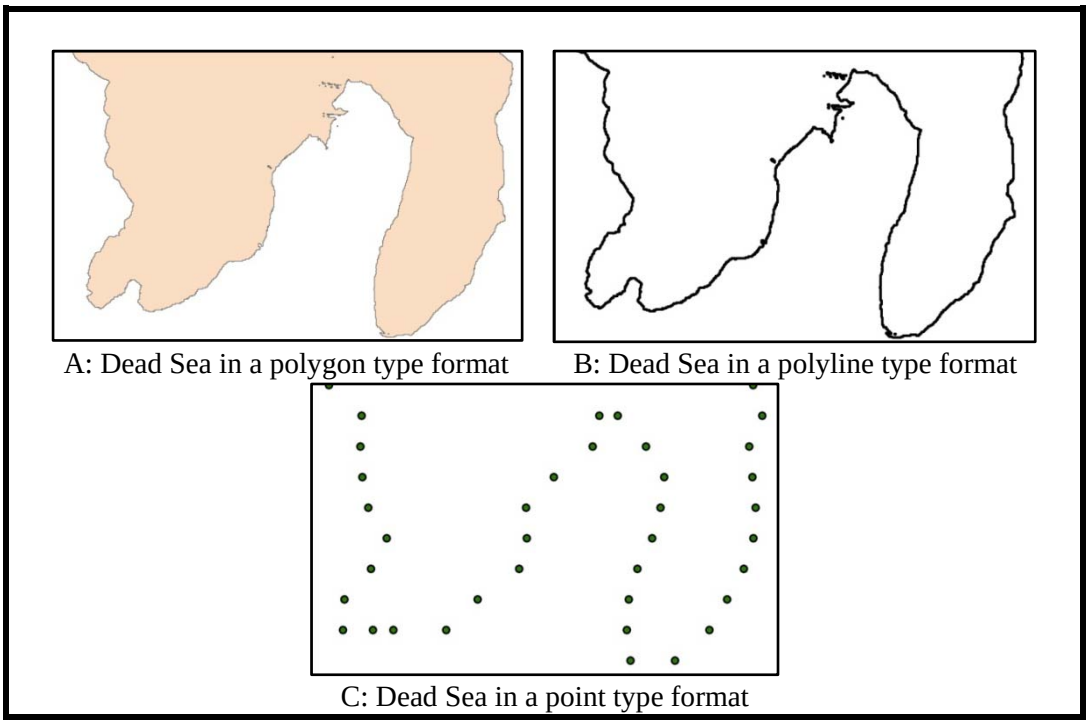

Figure 4-10 Dead Sea in point, line and polygon types

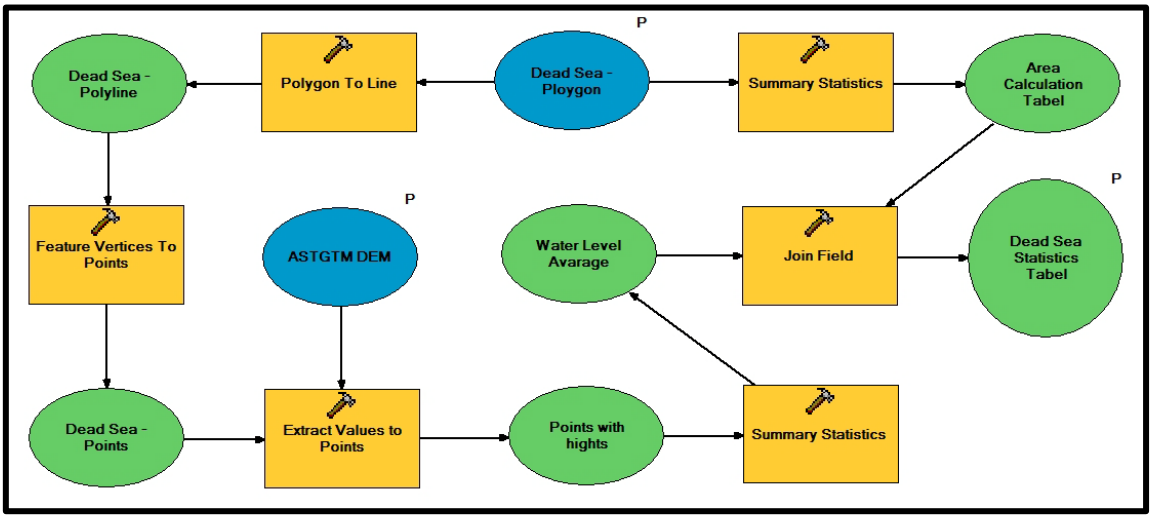

Figure 4-11 Change detection analysis model

Figure 4-12 shows the model interface which consists of the main inputs and outputs data.

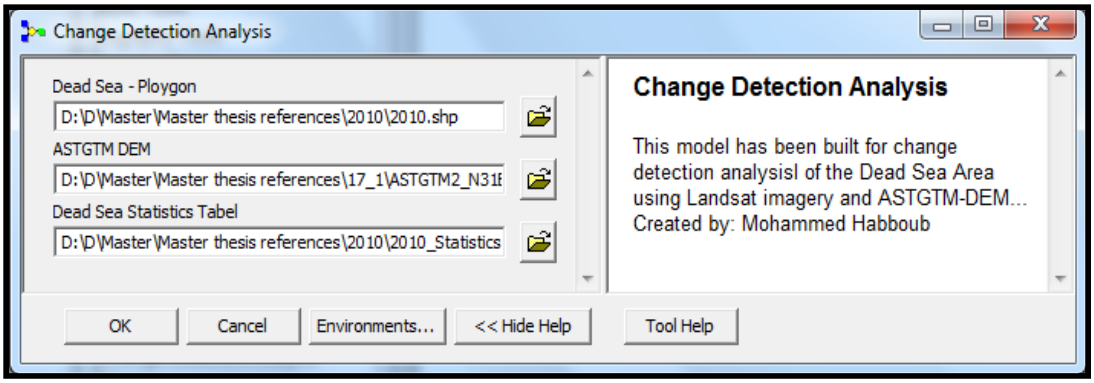

Figure 4-12 Change detection analysis model interface

4.7 Data Preparation for Prediction

In terms of future prediction, Markov - Cellular Automata (CA-Markov) model will be used. CA_Markov is a combined Cellular Automata, Markov Chain and Multi-Criteria Evaluation (MCE) land cover prediction procedure that adds an element of spatial contiguity as well as knowledge of the likely spatial distribution of transitions to Markov chain analysis. So, three main processes are required; Markov model, Cellular Automata model and validation and prediction. Figure 4-13 summaries the main steps in each process of data preparation for prediction which consists of three steps:

1. Markov chain analysis: In this step three outputs are generated; conditional probability images, transition probability matrix and transition area matrix.
2. Data generation for Multicriteria Evaluation (MCE): In this step two maps are created; bathymetric map which generated from TM imagery and slope map which generated from ASTGTM-DEM.
3. Suitability map creation using MCE.

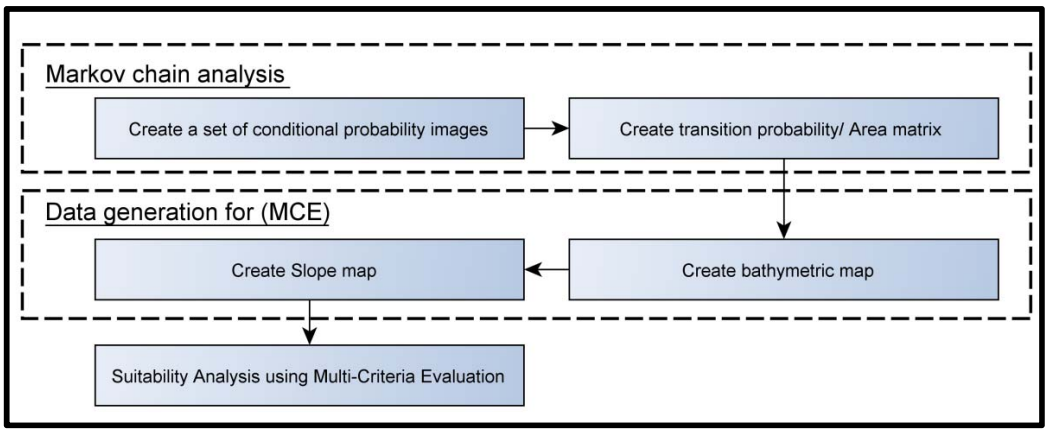

Figure 4-13 The main processes used in data preparation for prediction.

4.7.1 Markov Chain Analysis

Markov analysis needs two imageries as inputs to create (a) a transition probability matrix, (b) a transition area matrix (c) a set of conditional probability images.

This study focuses on the northern part of the Dead Sea since the southern part is turned into manmade evaporation bonds in 1987. The 1984 imagery is considered as the closest imagery from the separation date so it will be used as the first imagery in Markov analysis while 2010 is considered the later image to predict the 2020, 2030 and 2040 Dead sea shape.

The prediction of future changes based on the rates of past changes and on the probability that the Dead Sea Area will change from one mutually exclusive state to another. These probabilities are generated from past changes and then applied to predict future changes (Wen, 2008). Eastman (2012) lists the results of Markov chain as follows:

1. A transition probability matrix which expresses the likelihood that a pixel of a given class will change to any other class (or stay the same) in the next time period.
2. A transition areas matrix which expresses the total area (in cells) expected to change in the next time period.
3. A set of conditional probability images - one for each class. These maps express the probability that each pixel will belong to the designated class in the next time period. They are called conditional probability maps since this probability is conditional on their current state.

4.7.2 Data generation for Multicriteria Evaluation (MCE)

In this step two maps are created; bathymetric map which generated from TM imagery and slope map which generated from ASTGTM-DEM.

4.7.2.1 Bathymetric Map

As discussed above bathymetric map is one of the essential criteria map for prediction. The measurement of bathymetry can be expected to be the best with Landsat TM data because that sensor detects visible light from a wider portion of the visible spectrum, in more bands, than other satellite sensors. Landsat bands 1, 2 and 3 are all useful in measuring bathymetry, so too is band 4 in very shallow (<1 m), clear water over bright sediment (where bands 1-3 tend to be saturated). Bands 5 and 7 are completely absorbed by even a few centimeters of water and should therefore be removed from the image before bathymetric calculations are performed. Figure 4-14 shows the schematic illustration of Depth of Penetration (DOP); the DOP of band 1 is the largest (from 20-25m) in clear water, then DOP of band 2, 3 and 4 which are about 15, 5 and 1m respectively (Green, et al., 2000).

In order to create a bathymetric zones map represents a very crude bathymetric map, the following steps have to be accomplished one by one: First, finding out the average DN values of deep water pixels for blue, green, red and infrared bands of the 2010 Landsat TM image (Green, et al., 2000). This is done by finding a block of pixels (2500 pixel are used in this research) in a spot of the water-body known as deep water. Deep water block is identified by the lest DN in the imagery. In this research a squared spot centered in (X:739965E, Y: 3496125N, UTM) is used.

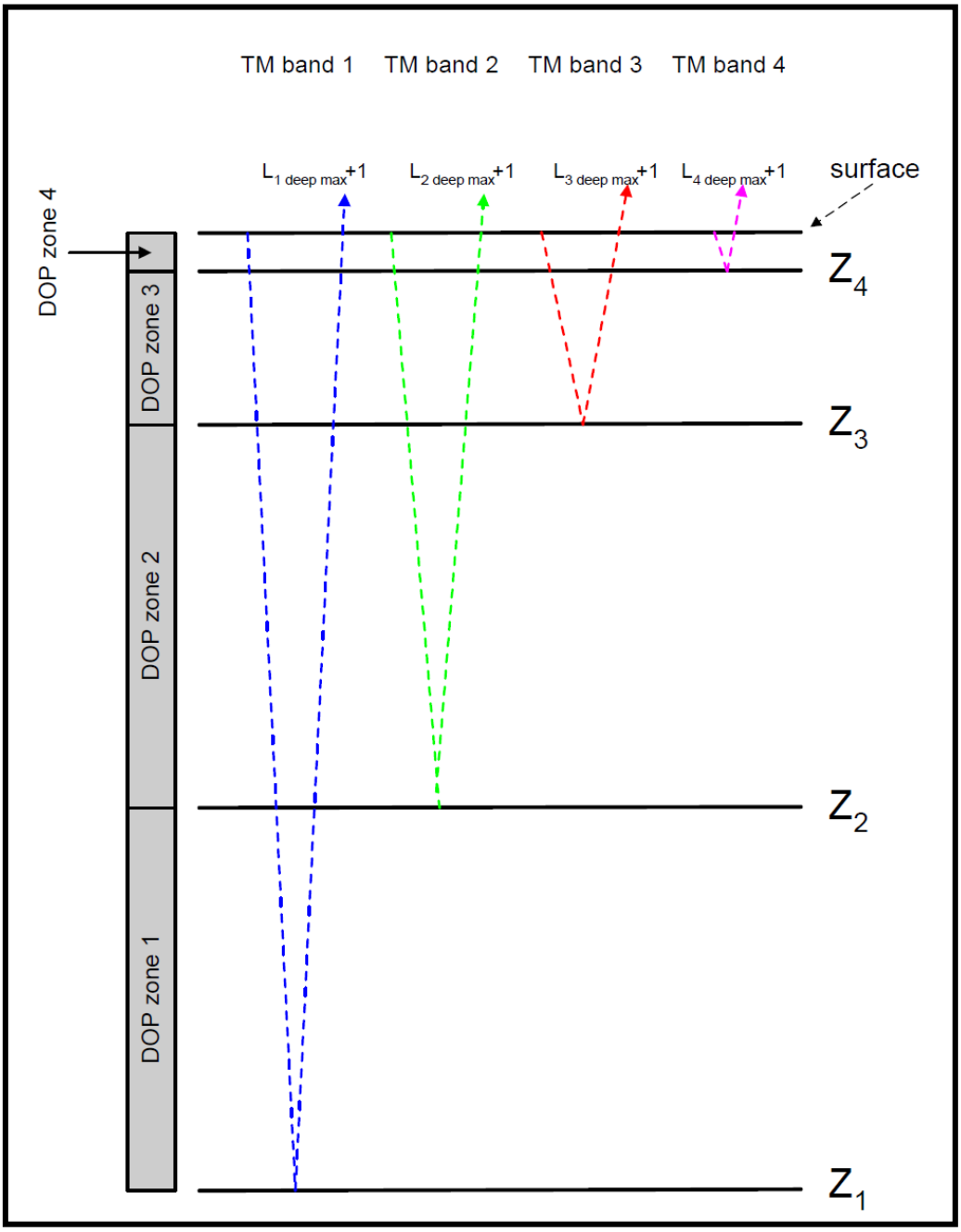

Figure 4-14 DOP zones of TM bands 1,2,3 and 4 (Green, et al., 2000)

In fact, either the image is radiometrically corrected or not, it would not affect the accuracy of the result because no comparisons between images will be made. Moreover the values of radiometrically corrected image will be too close or equal to zero which makes it difficult in creating the decision tree. The maximum, minimum and average values for the first four bands are listed as shown in Table 4-4.

Table 4-4 The maximum, minimum and average values for deep water in the first four bands

	Band 1	Band 2	Band 3	Band 4
Max DN of deep water	59	24	20	14
Min DN of deep water	51	20	15	11
Average DN of deep water	55	21	18	12

Green et al. (2000) explains that knowing the maximum DN values over deep water provides us a baseline. This baseline is used to determine the depth at pixels higher than background reflectance from the seabed.

For each waveband, if DN values are greater than the maximum deep water values then it is assumed that the sensor is detecting light reflected from the seabed but in this research, the average values are used instead of maximum values which represent more convenient results and better visualization since when using maximum values the results show that all Dead Sea water-body is very deep which is not correct.

There is no point in specifying certain depths in meters since the aim of this step is to get a classification of depths relative to each other not to develop an exact bathymetric map. Five classified zones is enough to develop a decision tree, see table 4-5, which used in creating bathymetric zones map.

Table 4-5 The decision tree used in creating bathymetric zones map

	Band 1	Band 2	Band 3	Band 4	Then
If DN is	≤55	≤21	≤18	≤12	Very deep
If DN is	>55	≤21	≤18	≤12	deep
If DN is	>55	>21	≤18	≤12	medium
If DN is	>55	>21	>18	≤12	shallow
If DN is	>55	>21	>18	>12	Very shallow

Using ERDAS Imagine, a model has been built by the researcher in order to develop bathymetric zones map, see Figure 4-15, the model consists of four inputs, and one output. The inputs are the first four bands while the output is the bathymetric zones map.

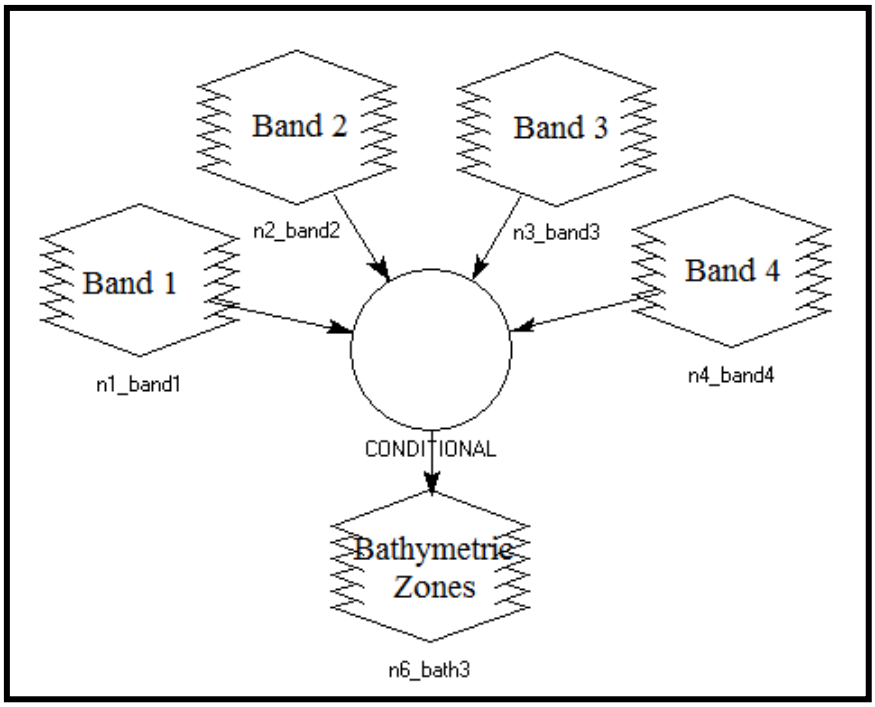

Figure 4-15 Bathymetric zones map model.

The process used in this model is a conditional statement represents the decision tree that shown in table 4-5. Equation 4-3 illustrates this conditional statement. The values 0, 63, 127, 191 and 255 are assigned to each zone in order to make it visually recognizable before cartographical presentation. Figure 4-16 shows the final bathymetric zones map.

$$
\begin{aligned}
&\boldsymbol{CONDITIONAL}\,\{\,(\boldsymbol{Band1}\ \leq \boldsymbol{55}\ \boldsymbol{AND}\ \boldsymbol{Band2}\\
&\quad \leq \boldsymbol{21}\ \boldsymbol{AND}\ \boldsymbol{Band3}\ \leq \boldsymbol{18}\ \boldsymbol{AND}\ \boldsymbol{Band4}\ \leq\ \boldsymbol{12}\,)\,\boldsymbol{0}\,,\\
&\quad\ (\boldsymbol{Band1}\ > 55\ \boldsymbol{AND}\ \boldsymbol{Band2}\ \leq \boldsymbol{21}\ \boldsymbol{AND}\ \boldsymbol{Band3}\\
&\quad \leq \boldsymbol{18}\ \boldsymbol{AND}\ \boldsymbol{Band4}\ \leq\ \boldsymbol{12})\boldsymbol{63}\,,\\
&\quad\ (\boldsymbol{Band1}\ > 55\ \boldsymbol{AND}\ \boldsymbol{Band2}\ > 21\ \boldsymbol{AND}\ \boldsymbol{Band3}\\
&\quad \leq \boldsymbol{18}\ \boldsymbol{AND}\ \boldsymbol{Band4}\ \leq\ \boldsymbol{12}\,)\boldsymbol{127}\,,\\
&\quad\ (\boldsymbol{Band1}\ > 55\ \boldsymbol{AND}\ \boldsymbol{Band2}\ > 21\ \boldsymbol{AND}\ \boldsymbol{Band3}\\
&\quad > 18\ \boldsymbol{AND}\ \boldsymbol{Band4}\ \leq\ \boldsymbol{12}\,)\boldsymbol{191}\,,\\
&\quad\ (\boldsymbol{Band1}\ > 55\ \boldsymbol{AND}\ \boldsymbol{Band2}\ >\ 21\ \boldsymbol{AND}\ \boldsymbol{Band3}\\
&\quad >\ 18\ \boldsymbol{AND}\ \boldsymbol{Band4}\ >\ 12\,)\,255\,\}
\end{aligned}
$$

Equation 4-3

4.7.2.2 Slope Map

Slope map is one of the essential criteria map for prediction. The creation of the slope map is a forward process using ArcGIS software – spatial analyst extension. However, the concept of creating slope map is by calculating the difference between DN stored in a ASTGTM-DEM cell and the minimum value on the eight adjacent cells in that

ASTGTM-DEM. Then, the calculated difference is divided by the cell size of ASTGTM-DEM. This process is repeated for every cell in ASTGTM-DEM in order to create the slope map. Figure 4-17 represents ASTGTM-DEM and slope maps.

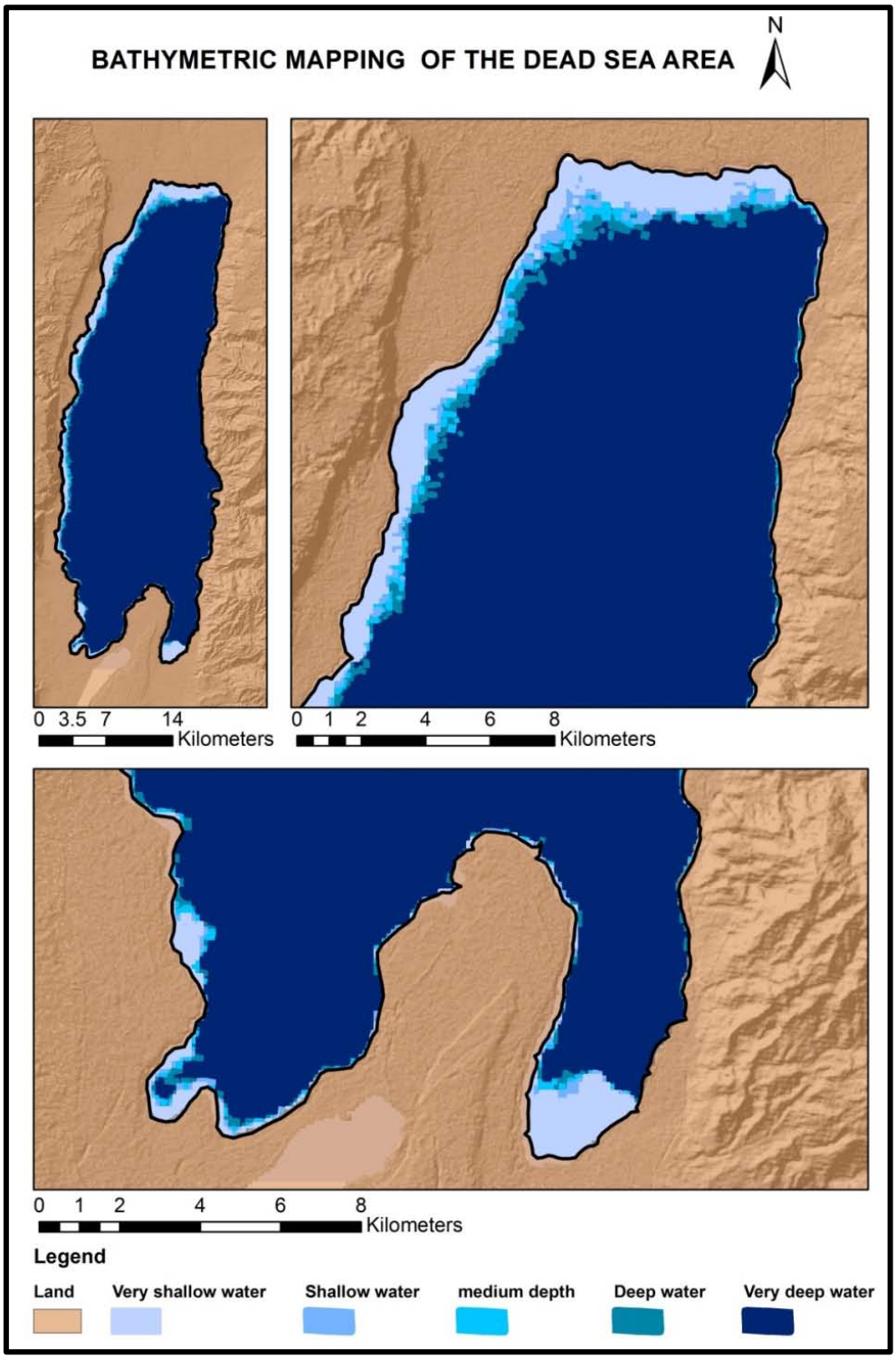

Figure 4-16 Zones of bathymetric map using the previous model

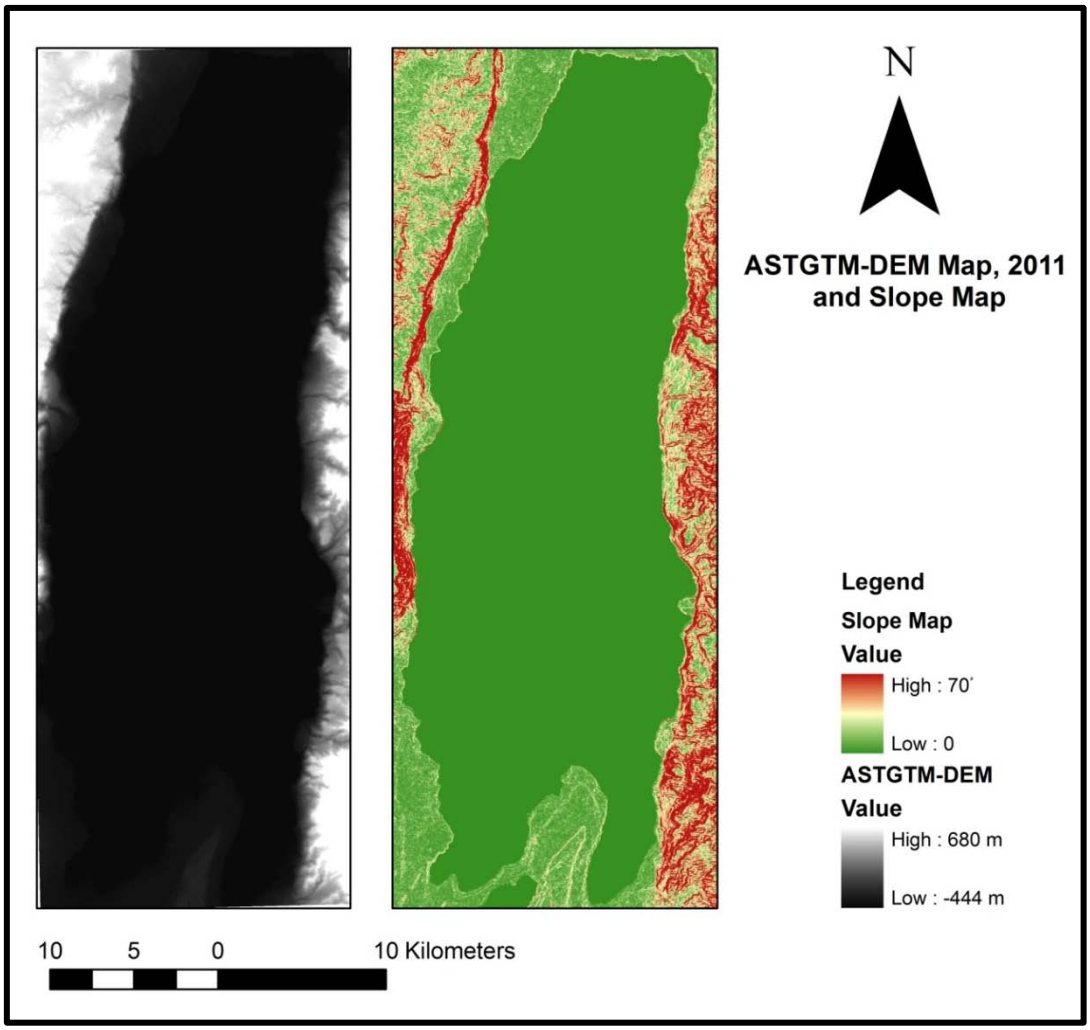

Figure 4-17 ASTGTM-DEM and Slope Map

4.7.3 Suitability Map Creation Using MCE

In order to use Cellular Automata, a suitability map for each class is considered as a prerequirement. Suitability maps are derived using Multi-Criteria Evaluation by combining the information from several criteria to form a single index of evaluation (Eastman, 2012). A weight linear combination equation –Equation 4-4 - is used to obtain suitability map for the Dead Sea Area.

$$S = \sum_{i=1}^{n} W_i C_i \prod_{i=1}^{n} r_i \qquad \text{Equation 4-4}$$

Where
S: Is the suitability map
W_i: Weight for a criteria i
C_i : Criteria for suitability
r_i: Restriction

By applying weights to each rated factor, the suitability map of the Dead Sea Area was developed using three maps; the bathymetric map, the probability of classes map derived from Markov process and the slope map derived from ASTGTM-DEM. More than one trial is made to get the best results in validation. Table 4-6 illustrates the final weights for each rated map criteria for each suitability map.

Table 4-6 Suitability map criteria weights and rates

Suitability map for water class			
	i = 1	i = 2	i = 3
C_i : Criteria for suitability	Bathymetric zones map rated from 0.1 to 1 as very shallow to very deep water respectively.	The water class probability map of Dead Sea Area derived from Markov process.	Slope map derived from ASTGTM-DEM map rated from 0.1 to 1 as the highest slope to the lowest slope respectively.
W_i: weight for a criteria i	34%	33%	33%
r_i: Restriction	Area boundaries		
Suitability map for land class			
	i = 1	i = 2	i = 3
C_i : Criteria for suitability	Bathymetric zones map rated from 0.1 to 1 as deep to very shallow water respectively.	The land class probability map of Dead Sea Area derived from Markov process.	Slope map derived from ASTGTM-DEM map rated from 0.1 to 1 as the lowest slope to the highest slope respectively.
W_i: weight for a criteria i	34%	33%	33%
r_i: Restriction	Very deep water	Area boundaries	

Using ArcGIS, a model has been built by the researcher, see Figure 4-18, to create the suitability map for water/Land class using MCE. The model consists of three inputs, blue ellipses, five tools, umber rectangles, and five outputs one of them is the resulted suitability map. The inputs are the class probability, the bathymetric zones and ASTGTM-DEM maps while the tools are slope generation tool, reclassification tools and weighted overlay tool. Figure 4-19 shows the model interface which consists of the main inputs and outputs data.

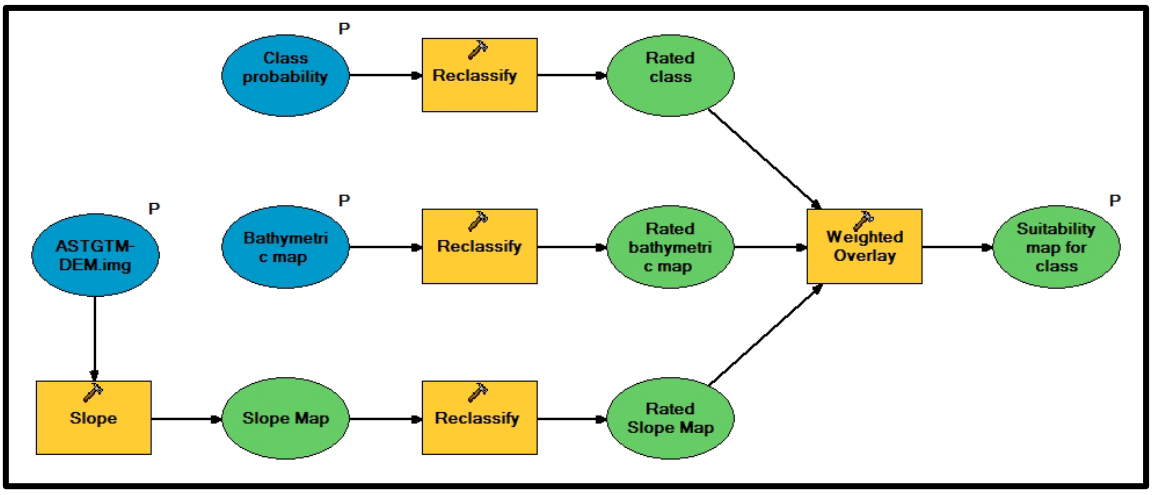

Figure 4-18 MCE model.

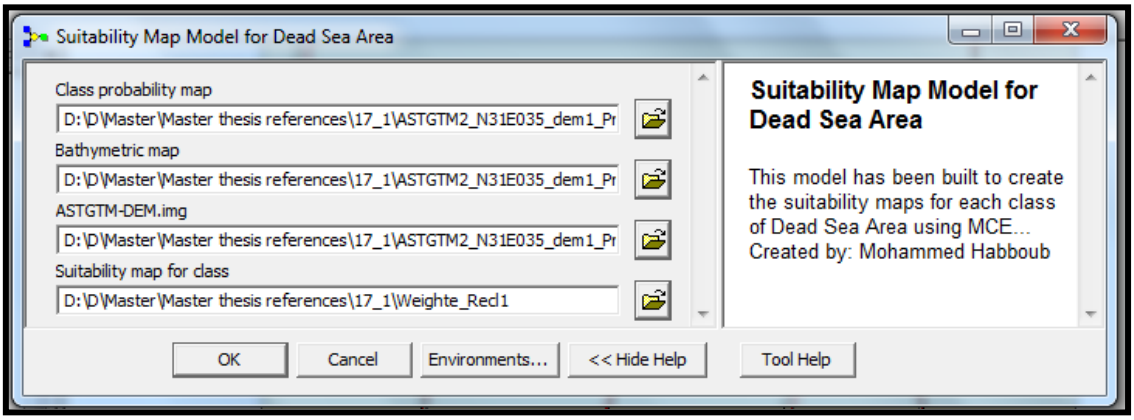

Figure 4-19 MCE model interface.

4.8 Prediction and Validation

Using the output data produced by the Markov chain analysis, the predicting model will apply a contiguity filter to grow out from imagery captured in the year of 2000 to a future time. This CA filter develops a spatially explicit contiguity-weighting factor to change the state of a cell based on its neighbors. Dead Sea shape at later dates of 2020, 2030 and 2040 will be created, but first 2010 map will be predicted and compared with the real 2010 classified imagery using the standard Kappa Index and other spatio-statistical parameters. Kappa index is used to check the results whether the model is true or not (usually the Kappa Index for the standard agreement is > 70 %) (Wen, 2008). If the model has the Kappa Index less than 70 % then the suitability map for the wetland area and/or filter used should be repeated again based on several considerations, otherwise, the suitability maps and the filter will be used to create the spatial model for 2020,2030 and 2040 years.

CHAPTER 5

5 Results and Discussion

5.1 Scope

This chapter illustrates the results of the detected changes in area, shape, water level and volume of the Dead Sea over time. Then, it discusses the relationship between area and water level. After that, it shows the results of Markov chain analysis and Multicriteria evaluation. Next, it presents the validation and statistical analysis results. Finally it discusses the predicted shapes of the Dead Sea.

5.2 The Change in the Area over Time

Historical studies tell that the Dead Sea has been separated into two basins in 1978, unfortunately, the earliest imagery which is convenient to the data collection criteria is in 1984, so from this date, it was preferred to distinguish between the two parts with focusing on the northern part since southern part is turned to manmade basins which represent from 25 to 29 % of the overall Dead Sea Area as shown in Figure 5-1. These percentages are calculated based on the supervised classification process and areas derivation using GIS and RS techniques discussed in chapter four.

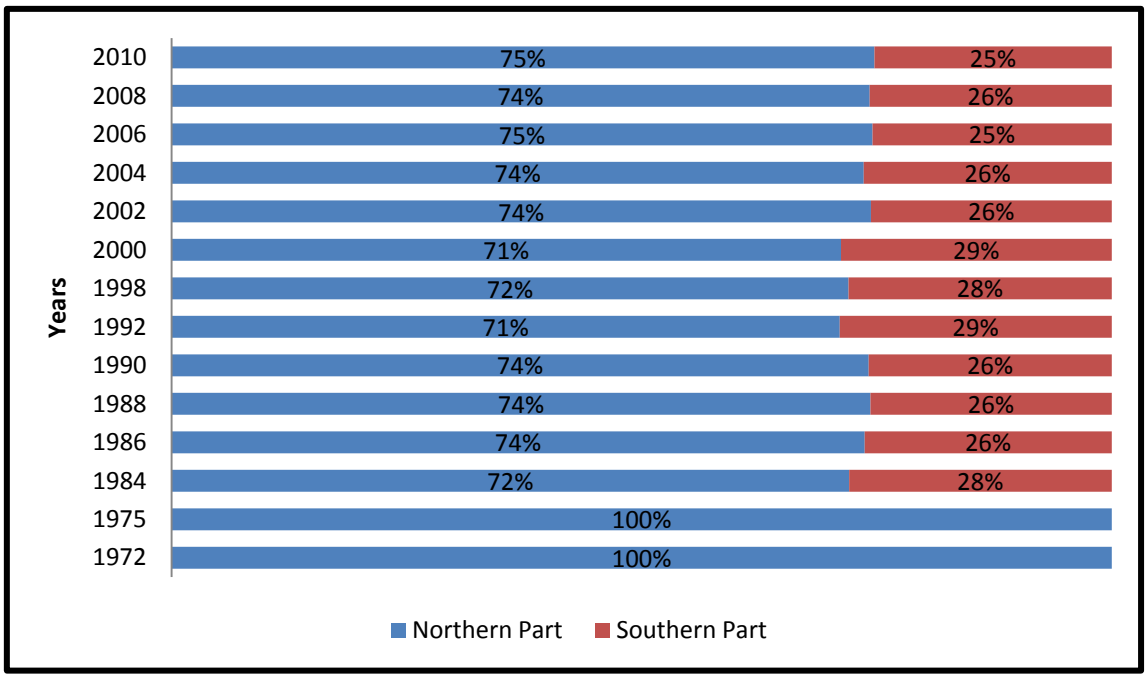

Figure 5-1 Northern and southern parts percentages to the overall Dead Sea area

The general trend of area of the northern part is decreasing as shown in Table 5-1 and Figure 5-2 which illustrate that from 1984 to 2010 the area of the northern part decreases in a percentage of 9.5%. The behavior of this trend is nonlinear and it is noticeable that the in 2000, 2004 and 2010 the level increased a little bit if compared with before and after years. This increasing making such a cycle, however this cycle could not be identified accurately due to the lack of imageries from 1992 to 1998. Worthy to say that the decrease between 1984 and 1992 – 8 years – reaches 7.98% while this percentage decreases to 1.8% from 1992 to 2010 – 18 years. This variation is due the variation of the amount used in industry, the amount of inflow released from Jordan River. Perhaps this variation is also due to the period of time consumed to use the water from the southern part in industrial use. In other words, from 1978 to 1984 is the period needed to use the southern part water and to start compensating by northern part water. In terms of defining the minimum values, it's clear that the area reaches the deck in 2008, 618.34 Km^2, but it is a little bit tricky to identify the main reason for this decreasing since there are more than one reason affecting the water-body area such as evaporation, inflow, precipitation and industrial uses. However weather data tells that the inflow amounts in this year were small enough to cause such deficit as shown in Figure 3-8. In general, the annual average area change is -2.5 km^2.

Figure 5-3-A illustrates the shapes of the water-body in 1972 while Figure 5-3-B represents the change in shape of the water-body from 1972 to 1975. The changes are detected in the eastern part of the south portion of the Dead Sea (before separation) and the bathymetry in the southern portion of the sea began to appear more clearly due to that shrinkage in area which reached about 6.1%.

Table 5-1 Total, northern and southern parts of Dead Sea areas

Year	Area (Km^2)	Northern part (Km^2)	Southern part (Km^2)
1972	986.21	986.21	
1975	926.01	926.01	
1984	968.37	697.94	270.43
1986	911.65	672.08	239.57
1988	898.30	667.70	230.60
1990	892.10	661.50	230.60
1992	904.62	642.87	261.75
1998	887.99	639.35	248.63
2000	901.82	642.04	259.78
2002	859.80	639.57	220.23
2004	865.80	637.43	228.37
2006	837.99	624.69	213.30
2008	832.89	618.34	214.55
2010	844.47	631.27	213.21

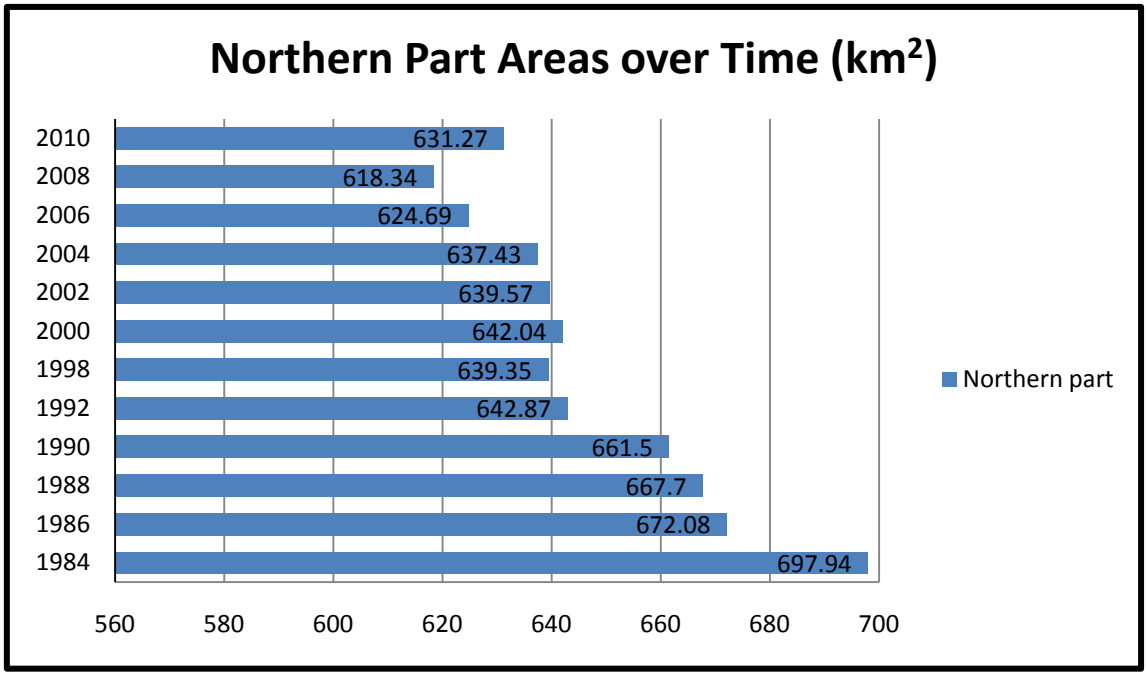

Figure 5-2 Northern part of Dead Sea areas from 1984 to 2010

Figure 5-3-C represents the change in shape of the water-body from 1975 to 1984 excluding the southern part (after separation). As discussed so far, this research focuses on the northern part of the Dead Sea since the southern part is converted to manmade evaporation basins.

Figure 5-4 shows the shape changes of the northern part water-body over 14 years, from 1984 to 1998. In general, the changes are detected in two major directions; from the northern west and from the south. The change in area reached 3.7% in the first year. It is worthy to say that there is no remarkable change in the eastern side of the Dead Sea; this is because the depth of the water is so deep where the fault exists.

Figure 5-5 illustrates the change occurred in the shape over 8 years, from 2000 to 2008. The shrinkage happened in the same direction even though the magnitude of the shrinkages is just 3.7% which the same percent of shrinkage between 1984 and 1986! However, the area increased in 2010 by about 2% as shown in Figure 5-6.

Figure 5-7 gives the big picture of what happened from 1972 till 2010, 38 years. It is worthy to say that the behavior of the water-body over time travels from north, northwest and south with no horizontal movement from the east which is very convenient to bathymetric zones map created and illustrated in Figure 4-16 even though the bathymetric map is derived from 2010 TM imagery (not before) but it gives a general trend of how the land behaves under water.

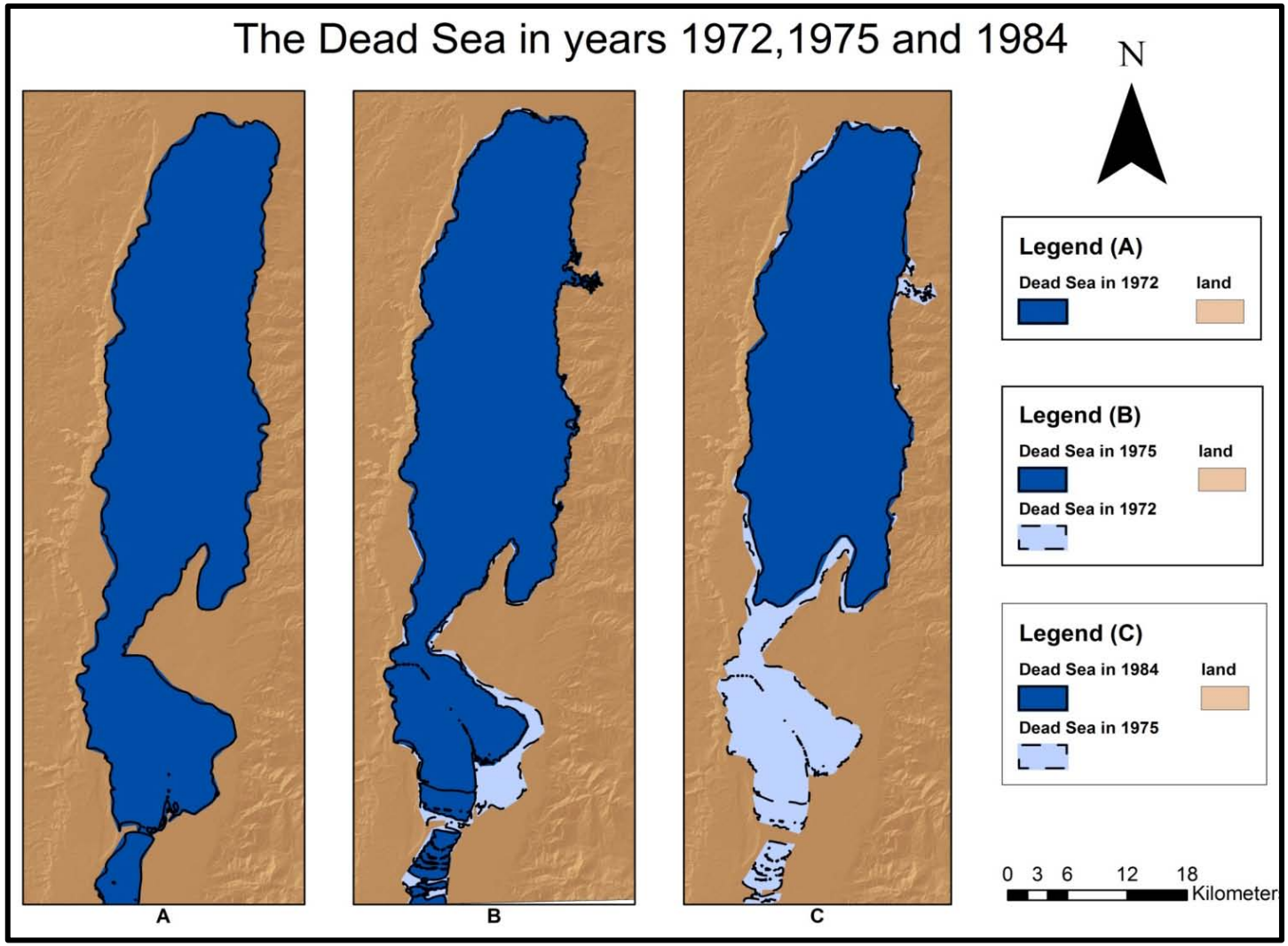

Figure 5-3 Dead Sea in 1972, 1975 and 1984

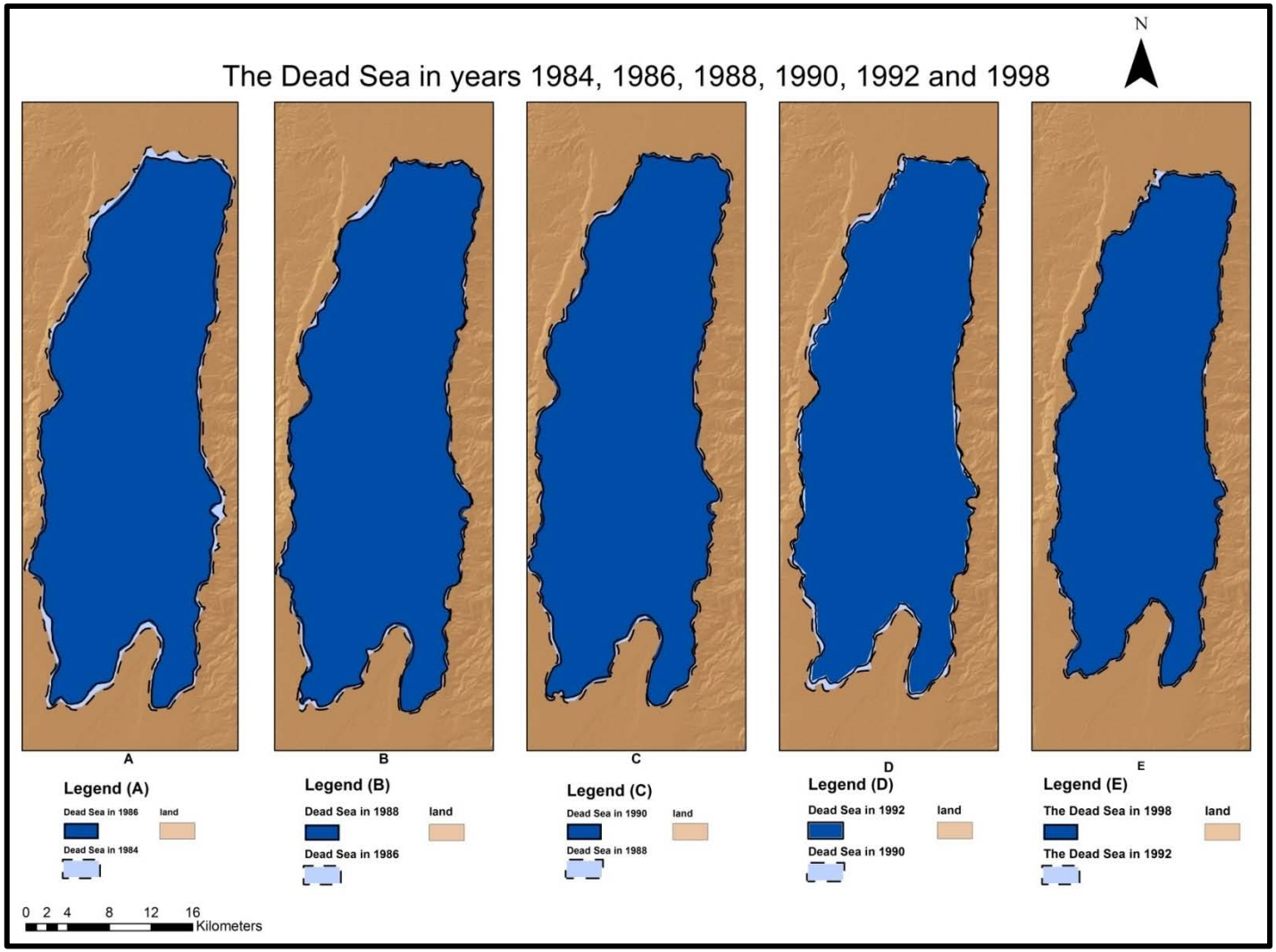

Figure 5-4 Dead Sea from 1984 to 1998

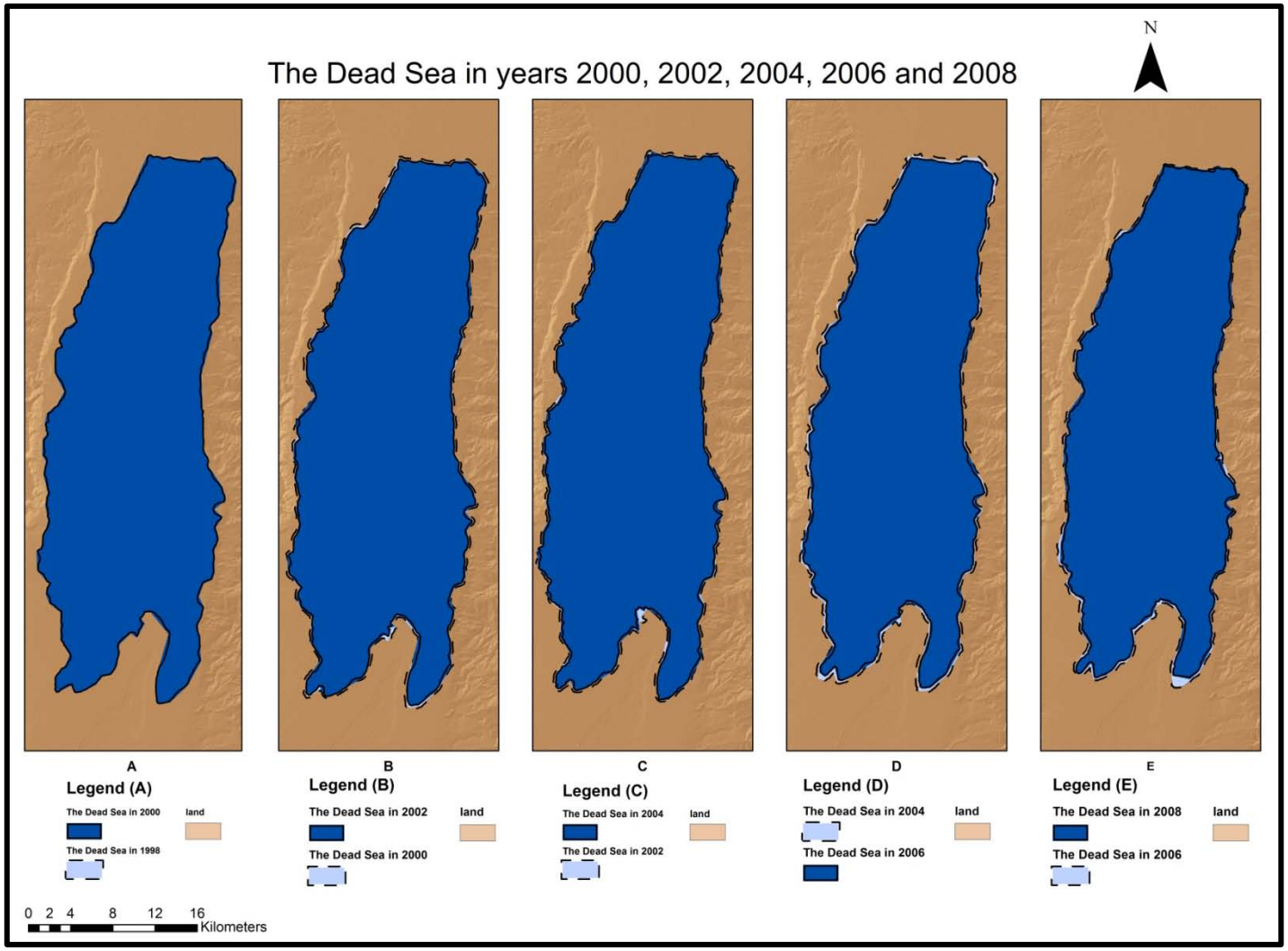

Figure 5-5 Dead Sea from 2000 to 2008

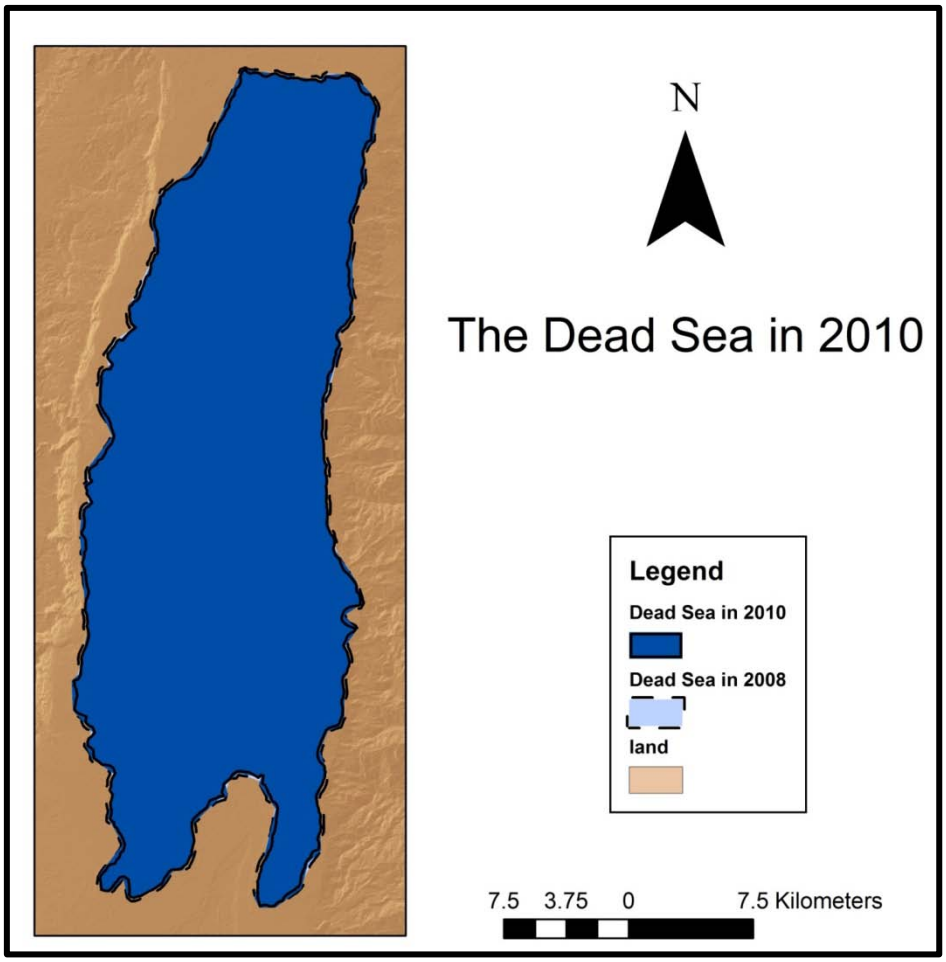

Figure 5-6 The Dead Sea in 2010

In fact, determining the exact reasons of this shrinkage in this percentage is too hard and need lots of researches and the area of closed sea such as the Dead Sea reflects more than one factor. The use of Dead Sea water for the industry by both Israel (Israeli occupation) and Jordan is one of the essential factors that affect area of the Dead Sea. Moreover these quantities are roughly estimated even in governmental reports. Climatic conditions playing an important part of this behavior of the water-body since this behavior is the result of the balance between water running into the sea from the tributary area and direct precipitation, minus water evaporation. In any case, the main reason causing this dramatic recession in the Dead Sea area is the intensive human water consumption from the Jordan and Yarmouk Rivers for other usage. Israel transfers huge quantities of surface water through the National Water Carrier from Upper Jordan River to the Negev, where these quantities equal 420 MCM/yr in addition to local consumption in the Tiberias Basin and the Huleh Valley.

By studying the trend behavior of this decrease, a third degree polynomial could be derived from regression analysis as shown in Figure 5-8 with R^2= 0.931 which indicates that the derived equation is representative.

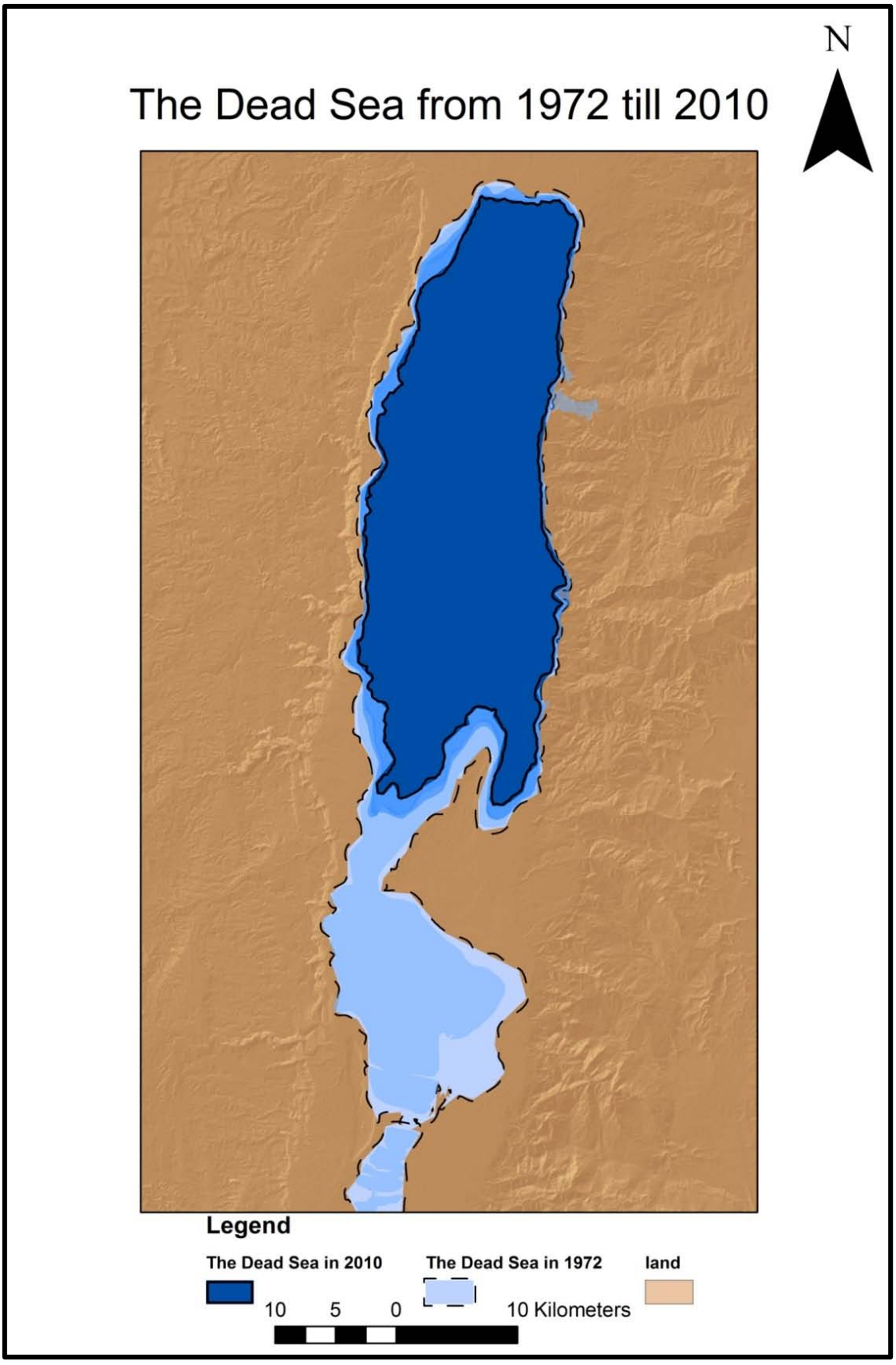

Figure 5-7 The Dead Sea from 1972 to 2010

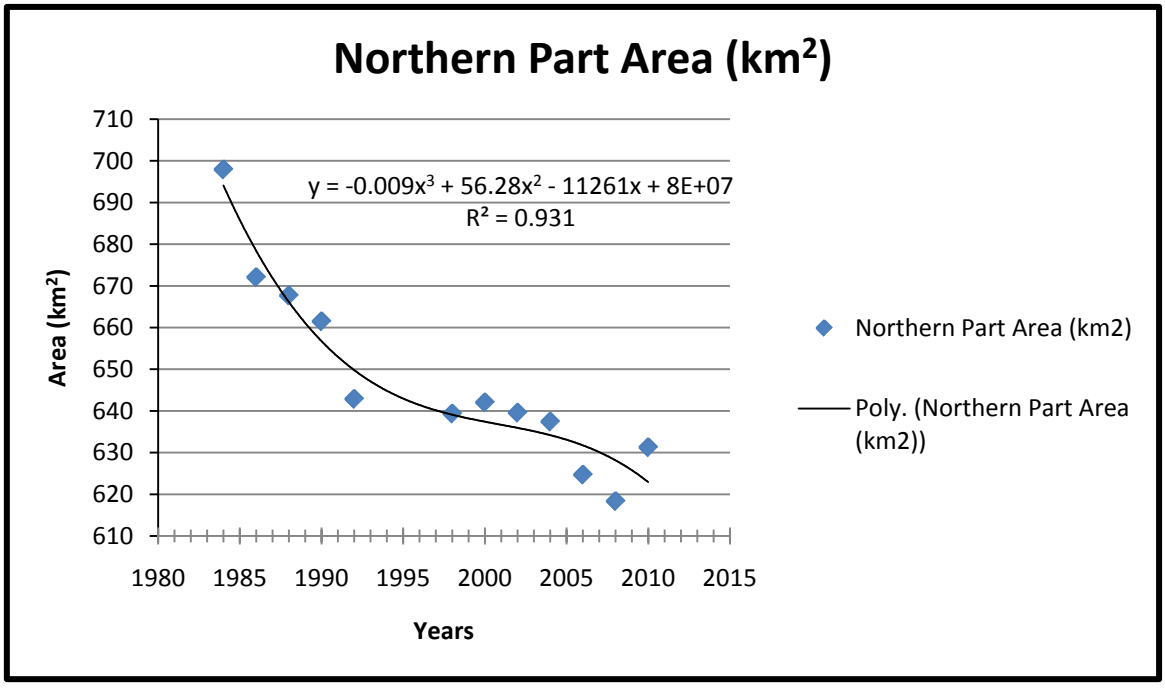

Figure 5-8 Regression analysis of the northern Dead Sea part over time

5.3 The Change in Water Level over Time

The derivation of the Dead Sea level was not a straight forward process even though the results were consistent with area changing as well as with previous studies, as will be discussed later.

Table 5-2 illustrates the average Dead Sea level in meters derived from ASTGTM-DEM raster data with standard deviation representing the variance values of these points about the average. It is obvious that from 1984 to 2010 the water level of northern part decreases by about 25.6 m and this decrease reaches more than this in 2006 and 2008.

Since the behavior of this trend is nonlinear, it is noticeable that from 1975 to 1984 the Dead Sea level raised dramatically by 6.6 m, perhaps this was due to the separation as discussed in the area change detection section. However, there is no point in finding a relation between water level and area before and after the separation since the boundary conditions is totally changed.

The change in water level between 1984 and 1986 is justified by changing in water-body area. In 2006 and 2008, the water levels reached the deck which correspond to water-body areas in these years which were less than the before and after years.

In general, every year the average water level change is -0.7m which is the same result that Abu Ghazleh et al. (2010) reached in her research.

By studying the trend behavior of this decrease, a third degree polynomial could be derived from regression analysis as shown in Figure 5-9 with R^2= 0.95 which indicates that the derived equation is representative.

Table 5-2 The average Dead Sea level with standard deviation

Year	Water level (m) Mean Sea Level	standard deviation
1972	-404.30	7.2
1975	-404.80	6
1984	-411.40	8
1986	-420.00	8
1988	-419.5	7.5
1990	-421.32	7.1
1992	-424.30	14
1998	-427.90	6
2000	-427.30	5
2002	-428.20	5.1
2004	-428.90	4.7
2006	-431.10	2.5
2008	-431.00	2.6
2010	-429.90	4.5

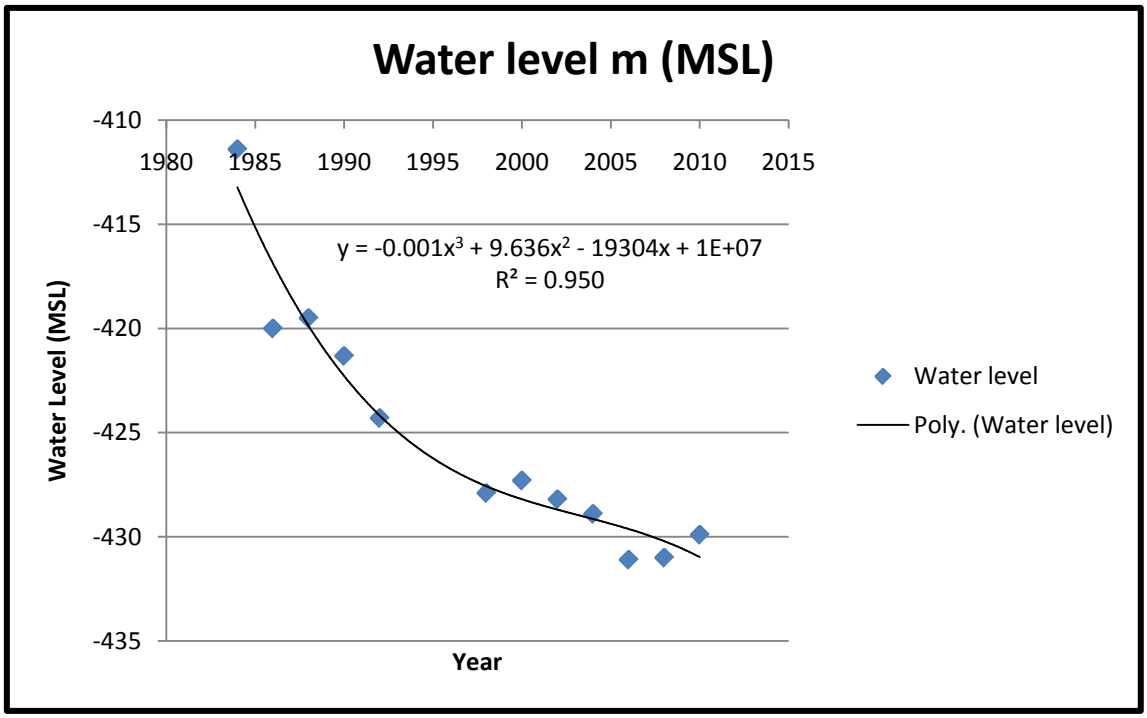

Figure 5-9 Regression analysis of the northern Dead Sea part over time

5.4 Area- Water Level Relationship

In order to find out the relation between the Dead Sea area and its water level, regression analysis is used putting the areas on x- axis and corresponding water level on y-axis to get an linear equation with R^2 = 0.967 which is considered a strong relation between both, see Figure 5-10. Therefore from this relation the water level could be estimated without even ASTGTM-DEM, just by using satellite imageries.

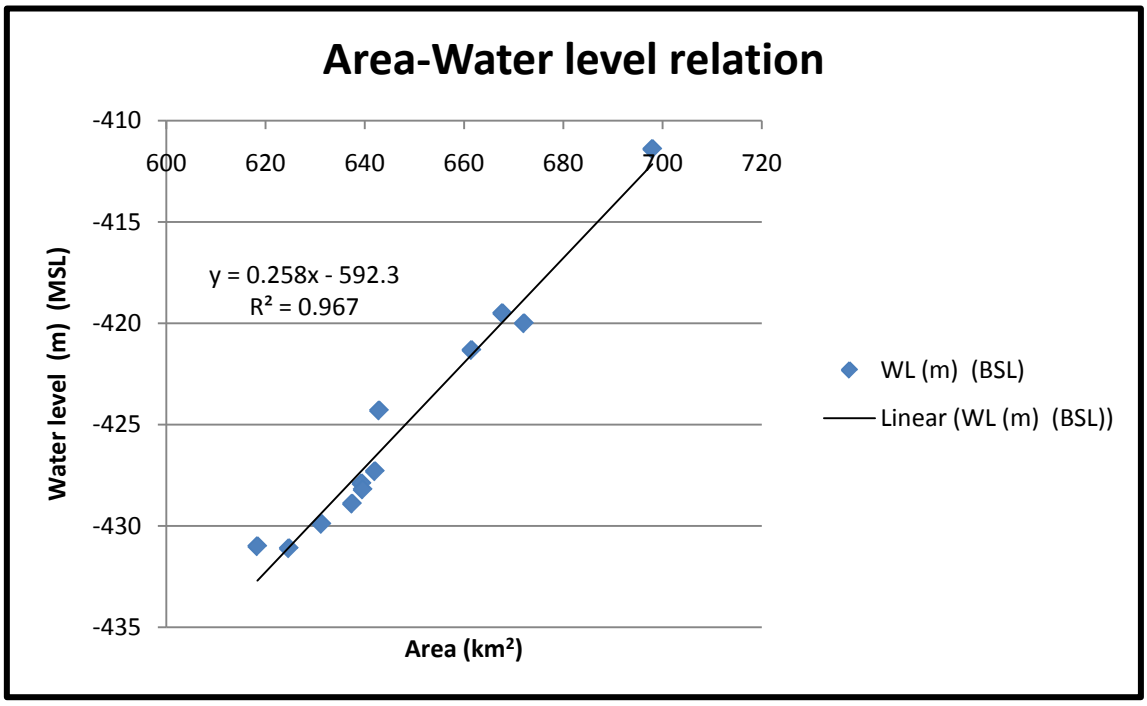

Figure 5-10 Relation between area and water level

5.5 The Change in Volume over Time

Based on area and water level derivations, the volume change could be calculated by using the following equation:

$$\Delta V = \frac{1}{2}(A_{1984} + A_t) \times (H_{1984} - H_t) \qquad \text{Equation 5-1}$$

Where:
ΔV : The change in volume.
A_{1984} : Dead Sea area in year 1984.
A_t : Dead Sea area in a given time.
H_t : Dead Sea water level in a given time.
H_{1984} : Dead Sea water level in year 1984.

Table 5-3 and Figure 5-11 illustrate the volume changing from the referential year, 1984. In general, every year the average volume change is -0.33 km^3.

Table 5-3 The Dead Sea volume change relative to the year of 1984

Year	change in Volume km^3	Year	change in Volume km^3
1984	-	2000	15.01
1986	8.16	2002	15.51
1988	7.63	2004	16.21
1990	9.32	2006	17.97
1992	12.20	2008	17.83
1998	15.46	2010	16.93

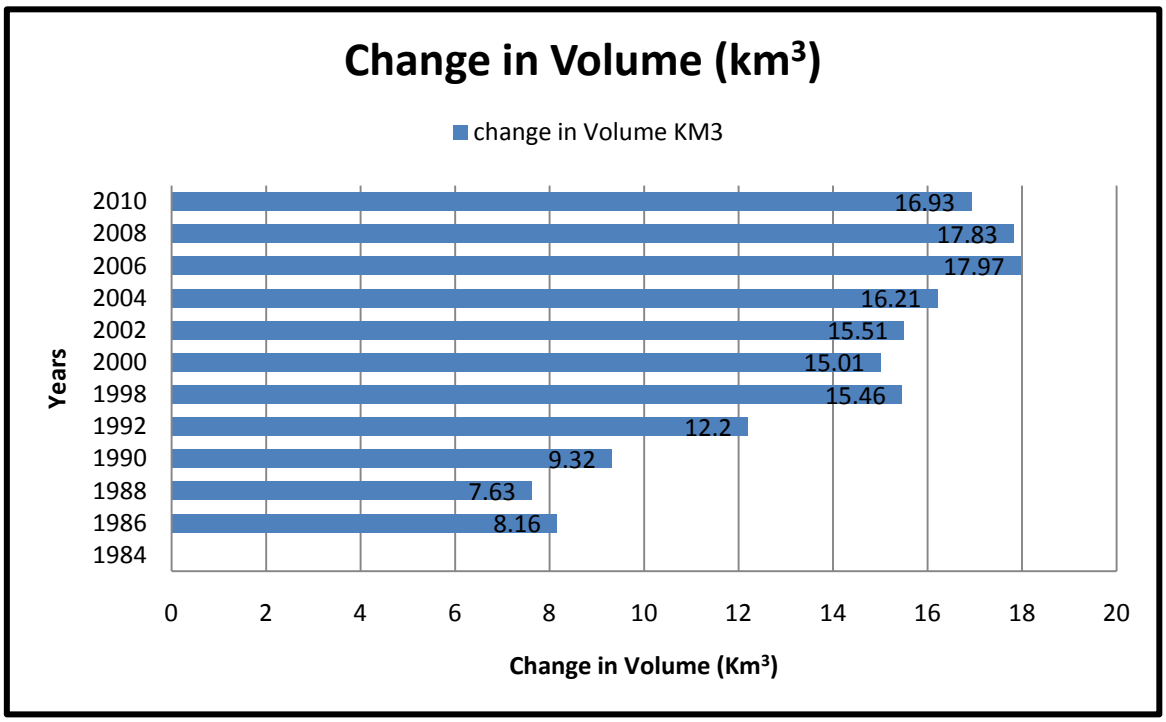

Figure 5-11 Dead Sea volume changing from the referential year, 1984.

5.6 Dead Sea Shape Prediction

5.6.1 Markov Chain Analysis

There are three outputs of Markov chain analysis for each predicted year. The following three outputs are resulted from using the classified imageries 1984 and 2000 as inputs in the process of predicting the 2010 map using CA-Markov analysis.

1. A transition areas matrix(1984-2000-2010):

$$\begin{bmatrix} & \text{Class 1 (water)} & \text{Class 2 (Land)} \\ \text{Class 1 (Water)} & 681062 & 32316 \\ \text{Class 2(Land)} & 416 & 1387417 \end{bmatrix}$$

The transition areas matrix (1984-2000-2010) expresses the total area (in cells) expected to change from the year of 2000 to the year of 2010 according to those changes happened from 1984 to 2000. Based on matrix above, there are 416 land classified cells (30m/cell) will turn into water class, meanwhile there are 32316 water classified cells will turn into land class.

2. Transition probability matrix(1984-2000-2010):

$$\begin{bmatrix} & Class\ 1\ (water) & Class\ 2\ (Land) \\ Class\ 1\ (Water) & 0.9547 & 0.0453 \\ Class\ 2(Land) & 0.0003 & 0.9997 \end{bmatrix}$$

The transition probability matrix (1984-2000-2010) expresses the likelihood that a pixel of a given class that will change to any other class (or stay the same) in the next time period. This could be derived from transition areas matrix by knowing the total cells of each class.

3. A set of conditional probability images/each class (1984-20000-2010)

These maps (Figure5-12-A) and (Figure5-13-A) express the probability that each pixel will belong to the designated class in the next time period. They are called conditional probability maps since this probability is conditional on their current state. So these maps are a cartographical presentation of the transition probability matrix.

5.6.2 Suitability Map Creation Using MCE

Multicriteria Evaluation is used to create suitability map for land and water classes. Figures 5-12-B show the classified slope map for land class which is rated from 0.1 to 1 as the lowest slope (less convenient to the land) to the highest slope (more convenient to the land) respectively, while Figure 5-12-C illustrates the classified bathymetric zones map for land class which is rated from 0.2 to 1 as the very deep water (less convenient to the land) to the very shallow water (more convenient to the land) respectively. The value of 1 is not assigned to the water-body for suitability but in order multiply overlaid layers by 1. Land restriction map is shown in Figure 5-12-D where deep water area is restricted for land class. Then the corresponding suitability map for land class 2010 is illustrated in Figure 5-12-E which is rescaled from 0-255 where the more DN (darker) is, the more suitable for land class. In contrast, Figure 5-13-B, Figure 5-13-C and Figure 5-13-D, represent classified slope map for water class, classified bathymetric zones map for water class and suitability map for water class 2010 respectively. It is obvious that the more DN is, the more suitable for water class. Figure 5-13-E illustrates the corresponding predicted 2010 Dead Sea shape.

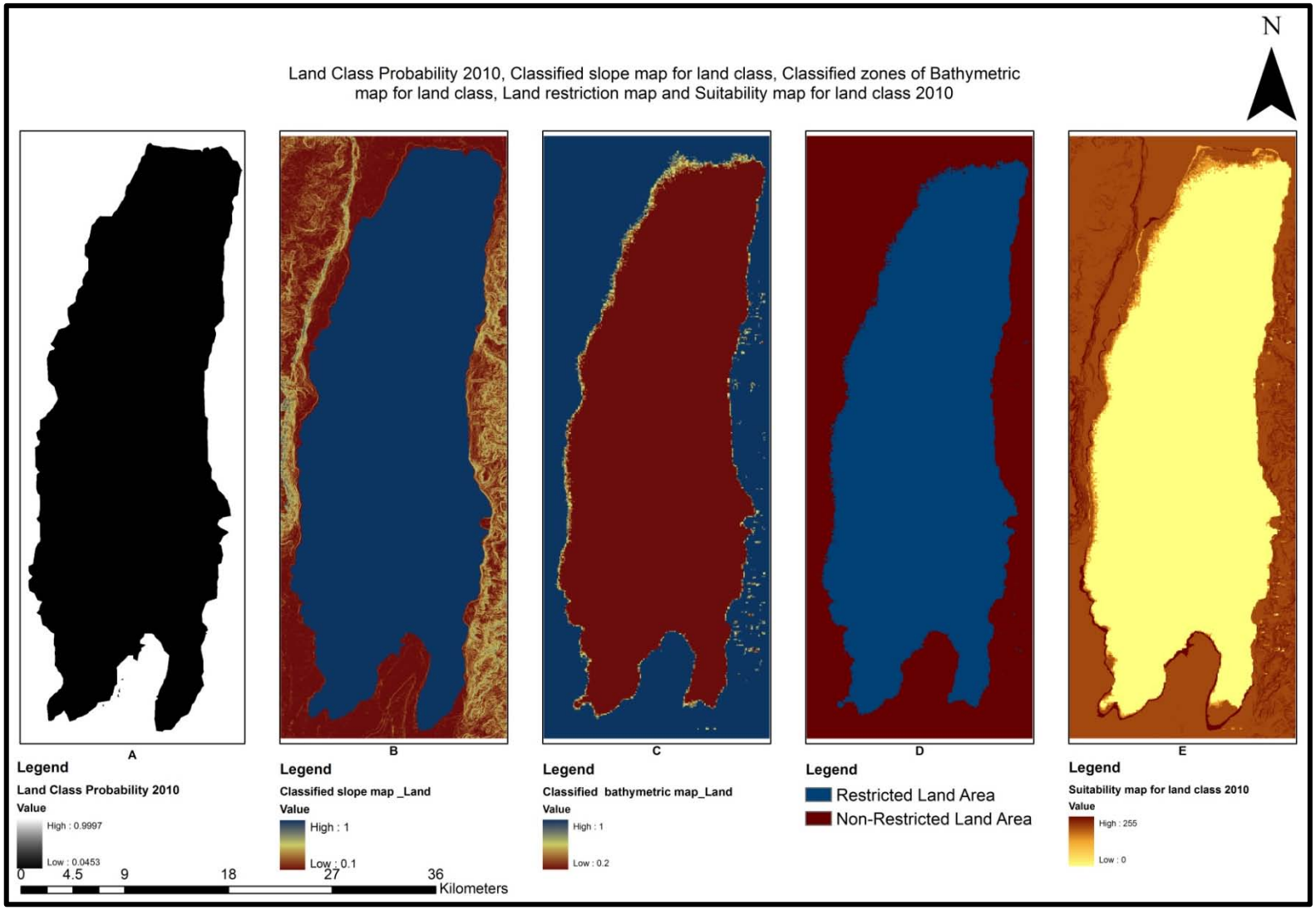

Figure 5-12 Data used for MCE and suitability map for land class 2010

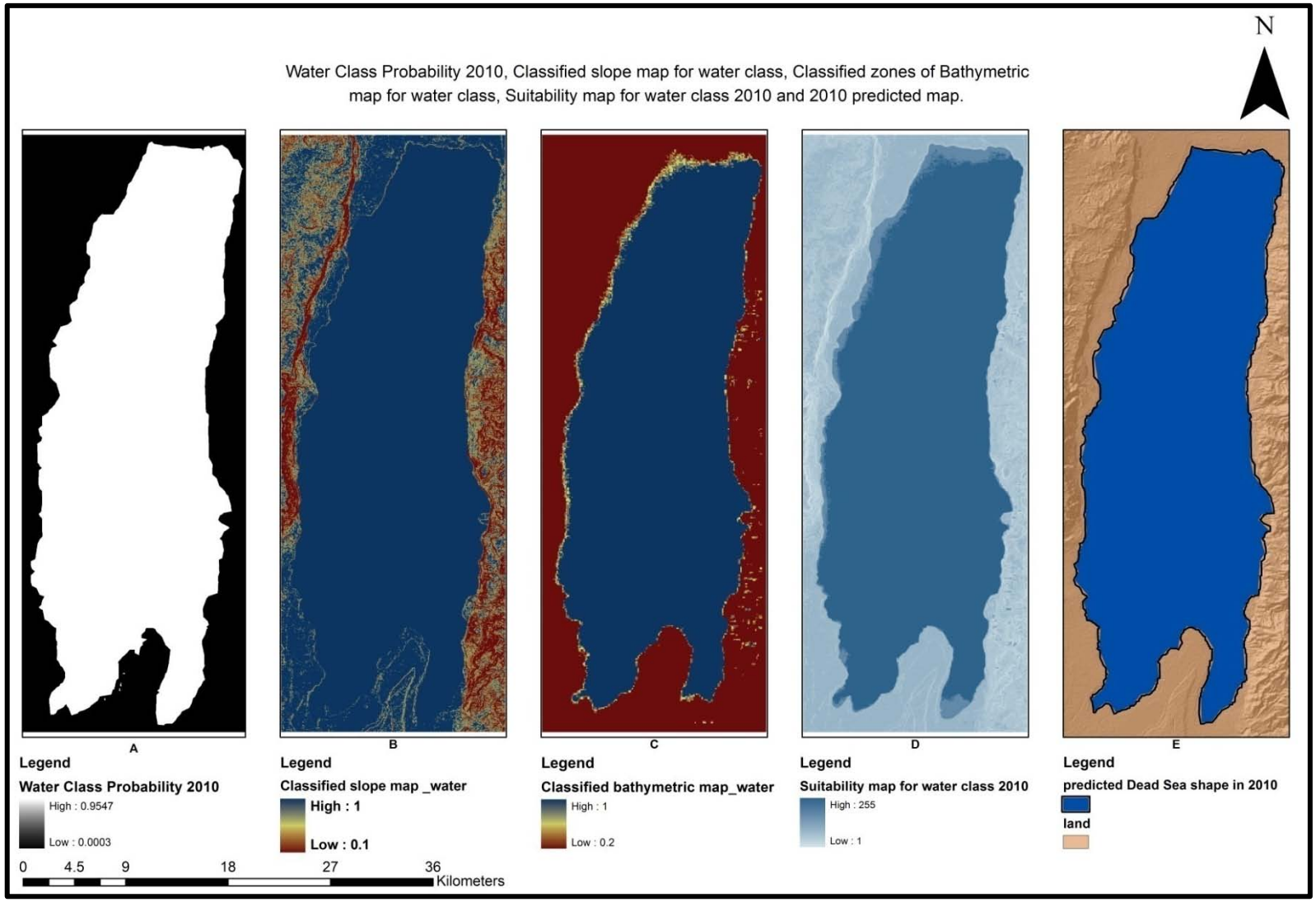

Figure 5-13 Data used for MCE, Suitability map for water class 2010 and 2010 predicted map

5.6.3 Prediction and Validation

By using the output data produced by the Markov chain analysis and MCE analysis, the predicting model applied for the year of 2010. The expected 2010 map is shown in Figure 5-14. Then, standard Kappa index is used to check whether the model is valid or not (usually the Kappa Index for a valid model is > 70 %) (Wen, 2008). If the model has the Kappa Index less than 70 % then the suitability map for the wetland area and/or filter used should be repeated again based on several considerations, otherwise, suitability maps and filter will be used to create the spatial model for 2020, 2030 and 2040 years.

Using VALADATE tool, IDRISI gave the standard Kappa of 0.9545, Kappa for no information of 0.9564, Kappa for grid-cell level location of 0.9981 and Kappa for stratum-level location of 0.9981 Which are all more than 0.7. Moreover IDRISI offers quantity disagreement of about 0.0209, which is convenient with the outputs of the transition matrix. Transitional matrix shows that the water-body will decrease by 28.63 km^2 from 2000 to 2010 to equal 613 km^2. However; the real 2010 map tells another story since the decrease from 2000 to 2010 was just 10.77 km^2 to equal 631.27. The percentage between both areas is 2.8% which so close to quantity disagreement since the difference could be due to some pixels generated in arbitrary locations (not inside the water-body) when using these stochastic algorithms. Strata disagreement = 0 which is logical because the number of output classes is the same as the number of input classes. The allocation disagreement = 0.0009 which is so close to zero. Since overall disagreement is 0.0218, the overall agreement is 0.9782. The overall agreement consists of agreement due to chance, agreement due to quantity and agreement due to grid cell level location. The agreement due to chance is the agreement that a scientist could achieve with no information of location and no information of quantity. Therefore, it could be a good baseline upon which to compare the actual agreement. The agreement due to chance equals 0.5. While the agreement due to grid cell level location which is the additional agreement when the comparison map is somewhat accurate in terms of its specification of the grid cell-level location of each category within each stratum. The agreement due

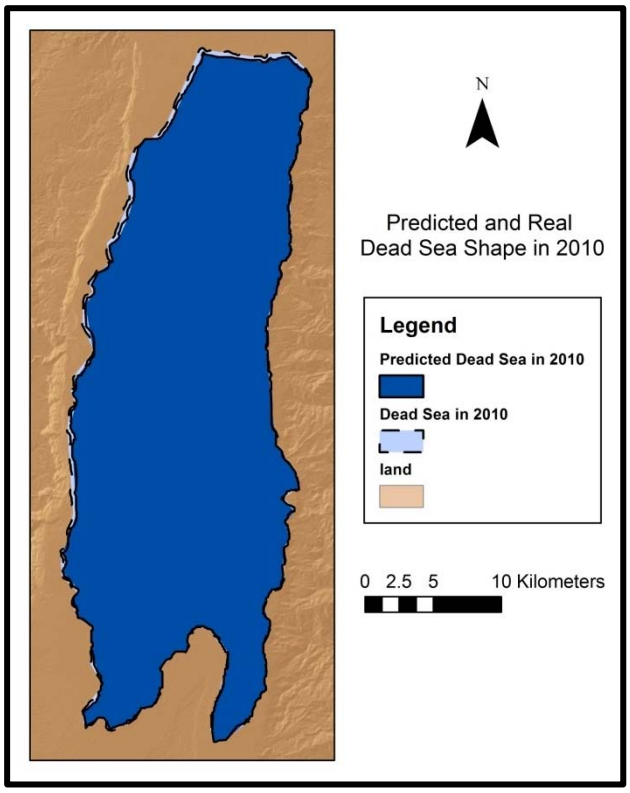

Figure 5-14 The predicted and real Dead Sea shape in 2010

to grid cell level location equals 0.4575. The agreement due to quantity which is the additional agreement when the comparison map is somewhat accurate in terms of its specification of quantity of each category. The agreement due to quantity equals 0.0207. There is no additional agreement when the comparison map is somewhat accurate in terms of its specification of quantity of each category within each stratum.

Another factor commonly used in the literatures which measures of agreement between maps called **M(m)** . It describes the agreement between the reference map and the unmodified comparison map. It is the proportion of grid cells classified correctly. It confounds agreement due to quantity and agreement due to location. IDRISI gives M(m) = 0.9782 which is considered a good matching. Figure 5-15 describes all these spatial statistics in number format and illustrates these values as a graphical bar shown in the left of the figure.

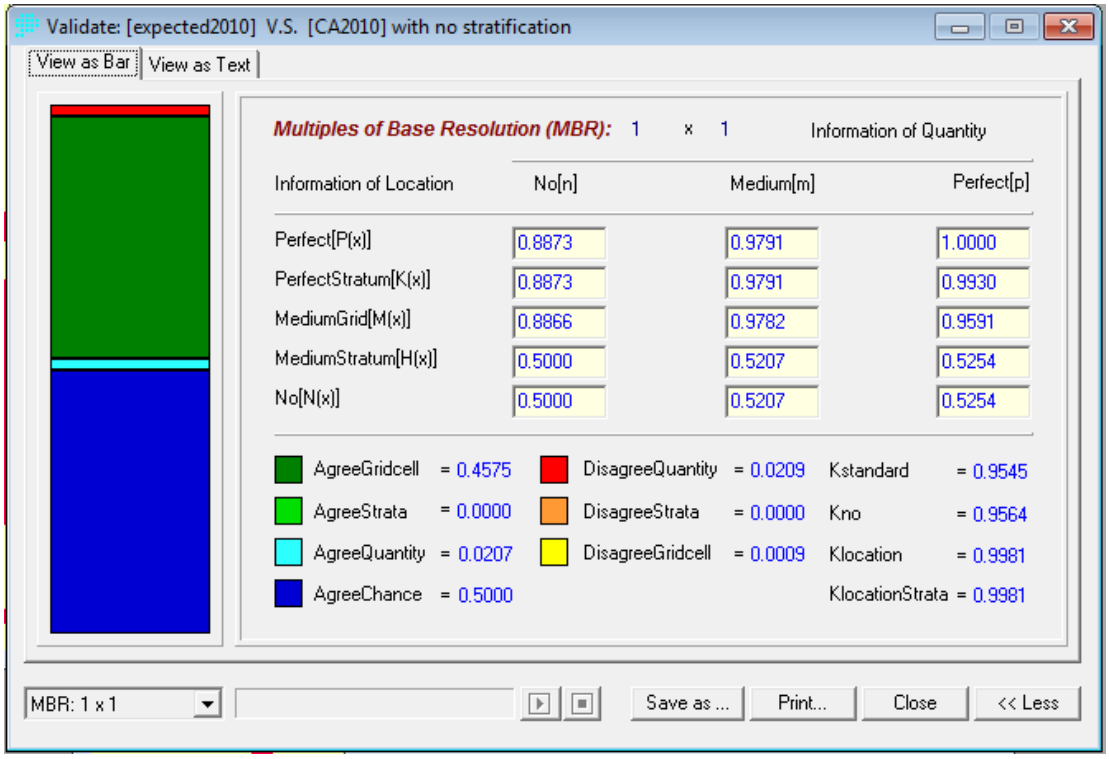

Figure 5-15 The spatio-statistical output graph generated in validation process

Based on these results, the suitability maps and model are valid and will be used to predict 2020, 2030 and 2040 maps as shown in Figure 5-16. The predicted shapes follow the same conditions from 1984 to 2010. The areas of predicted 2020, 2030 and 2040 are 610, 591 and 574km^2 which are considered a logical extension of the trend from 1984 till 2010. The direction of this shrinkage is from the north, northwest and from the south direction of the northern part due to slopes of bathymetry. No shrinkage is considered from the east direction due to the same reason since the bathymetric slope is so sharp.

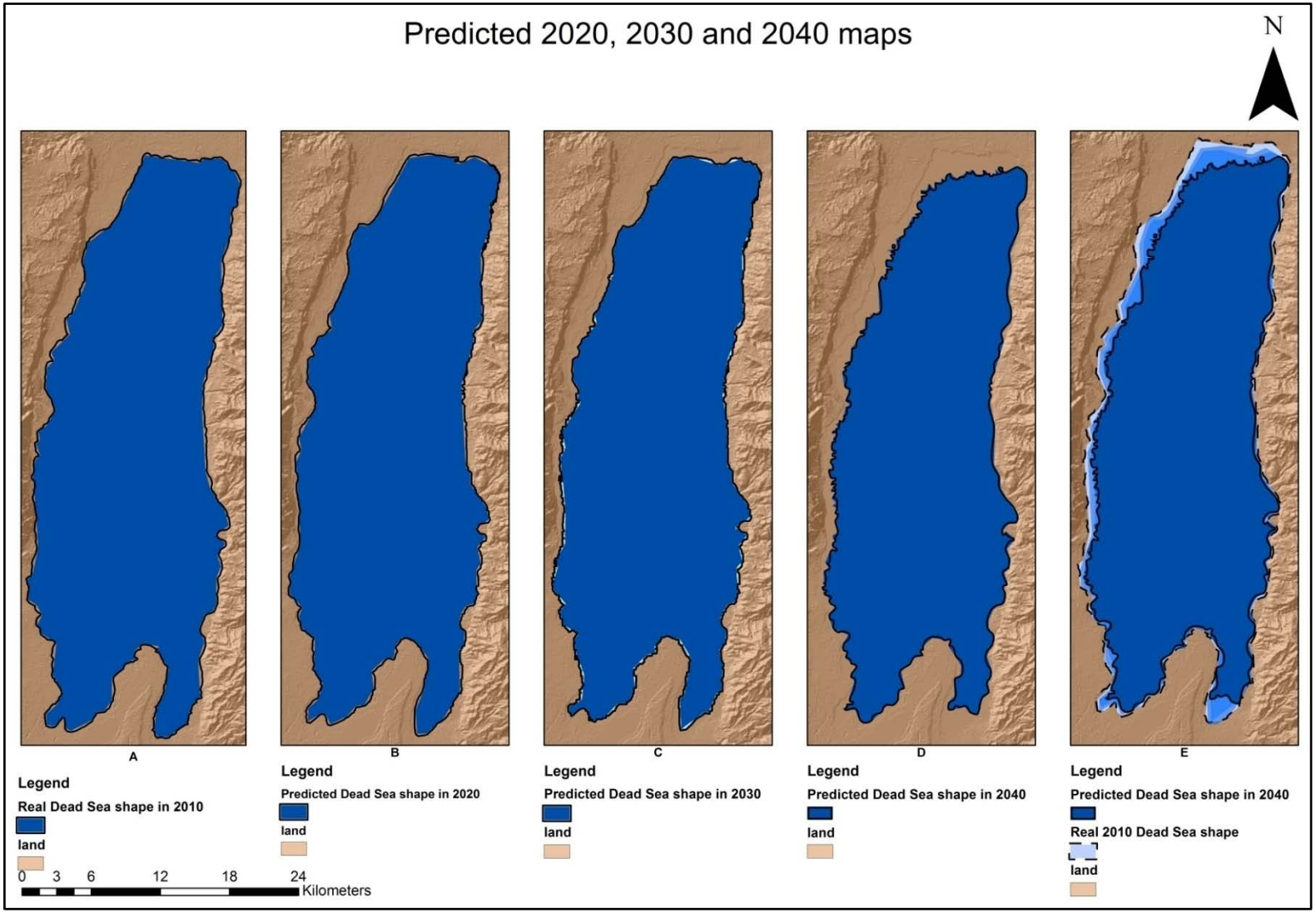

Figure 5-16 Predicted 2020, 2030 and 2040 maps

CHAPTER 6

6 Conclusion and Recommendations

6.1 Conclusion

The area of the Dead Sea surface - at the end of the fifties - was about 1000 km^2. The altitude of the surface was around 350 m below sea level. Since 1978, the Dead Sea has retreated, and the sea body turned into two basins: the principal northern one that was about 631.27 km^2 with a water level of -429.9 m (in 2010), and the shallow southern one with the Lisan Peninsula and the Lynch Straits in between, which has a sill elevation of about 400 m below the sea level.

The Dead Sea shrinks by 2.5 km^2 / yr while the water level decreases by 0.7m / yr. Consequently, the volume changes by -0.33 km^3 / yr. The use of Dead Sea water for the industry by both Israel and Jordan is one of the essential factors that affect area of the Dead Sea. The intensive human water consumption from the Jordan and Yarmouk Rivers for other usage is the main reason of that shrinkage in area as well.

The direction of this shrinkage is from the north, northwest and from the south direction of the northern part due to slopes of bathymetry. No shrinkage is considered from the east direction due to the same reason since the bathymetric slope is so sharp.

Markov – Cellular Automata is used in prediction process. The predicted shapes of 2020, 2030 and 2040 follow the same conditions from 1984 to 2010. The areas of predicted 2020, 2030 and 2040 are 610, 591 and 574km^2 which are considered a logical extension of the trend from 1984 till 2010. So Markov - Cellular Automata model can be used to predict closed seas as the Dead Sea.

6.2 Recommendations

- It is so recommended to use the result of this research in order to find strategies and solutions to keep the Dead Sea “alive”.
- The result of this spatial simulation model can be used as an environmental alert focusing on the Dead Sea case.
- It is so recommended to include hydrological parameter in prediction process and to use other surface water models to include Jordan valley in consideration that will give results more reliability.
- Using Markov – Cellular Automata analysis in landuse prediction is highly recommended because it gives very accurate results.

7 Bibliography

Abu Ghazleh, Shahrazad, et al. 2010. Rapidly Shrinking Dead Sea Urgently Needs Infusion of 0.9 km 3 /a from Planned Red-Sea Channel: Implication for Renewable Energy and Sustainable Development. Germany : s.n., 2010. Vol. 4. 1995-6665.

Agnew, Mike. 2005. Geological Significance. *Dead Sea Geo.* [Online] 2005. [Cited: 2 22, 2013.] http://deadseageo.webs.com/geologicalsignificance.htm.

Akin, Erika and Cooley, Skye. 2013. Lake Basin Volume. *GIS 4 Geomorphology*. [Online] 2013. [Cited: 3 11, 2013.] http://gis4geomorphology.com/lake-basin-volume/#more-1239.

Al-Zubaidy, Rashid, Khaled, Moh'd- and Shambour, Yousef. 2011. Prediction of the Dead Sea Water Level using Neural Networks. s.l. : Fourth International Symposium on Innovation in Information & Communication Technology, 2011.

Asmar, Basel. 2003. The science and politics of the Dead Sea : Red Sea canal or pipeline. s.l. : Journal of environment and development, 2003.

AUG signals. 2008. Change Detection. *AUG SIGNALS.* [Online] 2008. [Cited: 11 19, 2012.] http://www.augsignals.com/page.php?menu=14.

Baker, Corey, et al. 2007. Change Detection Of Wetland Ecosystems Using Landsat Imagery And Change Vector Analysis. s.l. : The Society of Wetland Scientists, 2007. Vol. 27.

Bell, Earl and Hinojosa, R. 1977. Markov analysis of land use change: Continuous time and stationary processes. 1977. pp. 13-17.

Briassoulis, Helen. 2012. Analysis of Land Use Change: Theoretical and Modeling Approaches. [Online] 2012. [Cited: 3 24, 2013.] http://www.rri.wvu.edu/WebBook/Briassoulis/chapter4(models6).htm#4.7.2.

Cabral, Pedro and Zamyatin, Alexander. 2006. Three Land Change Models For Urban Dynamics Analysis In Sintra-Cascais Area. Humboldt-Universität zu Berlin : s.n., 2006.

Chavez. 1996. Image-Based Atmospheric Corrections - Revisited and Improved. s.l. : PE & RS, 1996.

Collet, Claude and Barboux, Chloé. 2012. GITTA. [Online] 2012. [Cited: 3 26, 2013.] http://gitta.info/SpatChangeAna/en/html/Spat_dyn_mod_discont_learningObject1.html.

Cooley, Skye. 2013. Minimum Eroded Volume. *GIS 4 Geomorphology.* [Online] 2013. [Cited: 3 11, 2013.] http://gis4geomorphology.com/calculate-basin-volume/#more-8.

Dead Sea Research Team. 2011. *Red Sea – Dead Sea Water Conveyance Study Program.* s.l. : TAHAL Group & the Geological Survey of Israel (GSI), 2011. IL-201280-R10-055A.

Deer, P. 1999. Digital Change Detection Techniques. *Civilian and Military Application Published in the UK.* s.l. : Taylar & Francis Ltd, 1999.

Eastman, J. Ronald. 2012. IDRISI Selva Manual. 2012.

—. 2012. IDRISI Tutorial. s.l. : Clark University, 2012.

Falk, Michael, et al. 2011. *A First Course on Time Series Analysis.* University of W□urzburg : s.n., 2011.

Fonstad, Mark A. 2006. Cellular automata as analysis and synthesis engines at the geomorphology–ecology interface. *Geomorphology.* s.l. : ELSEVIER, 2006. Vol. 77, 3-4.

Green, Edmund P., et al. 2000. *Remote Sensing Handbook for Tropical Coastal Management.* 2000.

Irons, Jim. 2011. Chapter 11. *landsat hand book/ NASA.* [Online] 3 11, 2011. [Cited: 3 8, 2013.] http://landsathandbook.gsfc.nasa.gov/data_prod/prog_sect11_3.html.

Jesús D. Chinea. 2006. Supervised Classification. *Universidad de Puerto Rico, Recinto Universitario de Mayagüez.* [Online] 2006. [Cited: 3 7, 2013.] http://www.uprm.edu/biology/profs/chinea/gis/lectesc/tut4_3.pdf.

Jianya, Gong, et al. 2008. A Review Of Multi-Temporal Remote Sensing Data Change Detection Algorithms. Hong Kong : The International Archives of the Photogrammetry, Remote Sensing and Spatial Information Sciences, 2008. Vol. XXXVII.

Kandare, Kaja. 2000. *The time series change detection methods of remote sensing.* 2000.

Kushwaha, S.P.S., et al. 2011. Forest Ecosystem Dynamics Assessment And Predictive Modelling Ineastern Himalaya. *International Archives of the Photogrammetry, Remote Sensing and Spatial Information Sciences.* 2011. Vol. XXXVIII.

LU, D., et al. 2004. Change detection techniques. s.l. : Taylor & Francis Ltd, 2004. Vol. 25.

Maps of tha world. 2010. Dead Sea. *Maps of tha world.* [Online] 2010. [Cited: 2 22, 2013.] http://www.mapsofworld.com/jordan/tourism/the-dead-sea.html.

Memarian, Hadi, et al. 2012. Validation of CA-Markov for Simulation of Land Use and Cover Change in the Langat Basin, Malaysia. *Journal of Geographic Information System.* 2012.

Moayeri, M., et al. 2012. Change Detection of Wetland Development with Satellite Data and GIS. s.l. : American Journal of Scientific Research, 2012. 73. 2301-2005.

Morin, Efrat, et al. 2009. Flash Flood Prediction In The Dead Sea Region Utilizing Radar Rainfall Data. s.l. : Journal of Dead-Sea and Arava Research, 2009. Vol. 1.

Ndzeidze, Stephen Koghan. 2009. *Detecting Changes in a Wetland: Using Multi-Spectral and Temporal Landsat in the Upper Noun Valley Drainage Basin-Cameroon.* 2009.

Omar, Manal. 1996. Shrinking of Dead Sea raises deep environmental concerns . 1996.

Pontius, R. Gil. 2000. Quantification error versus location error in comparison of catagoral maps. 2000.

Pontius, R. Oil. 2002. Statistical Methods to Partition Effects of Quantity and Location During Comparison of Categorical Maps at Multiple Resolutions. *Photogrammetric Engineering & Remote Sensing.* 2002. Vol. 68.

Pontius, Robert Gilmore and Millones, Marco. 2011. Death to Kappa: birth of quantity disagreement and allocation disagreement for accuracy assessment. *International Journal of Remote Sensing.* s.l. : Taylor & Francis, 2011. Vol. 32.

Ramsey, R. Douglas. 2010. Image Standardization. *RS/GIS Laboratory.* [Online] 2010. [Cited: 3 8, 2013.] http://earth.gis.usu.edu/imagestd/.

Reinert, Gesine. 2010. *Time Series.* 2010.

Richard, J., et al. 2005. Image Change Detection Algorithms. *A Systematic Survey.* s.l. : , IEEE Transactions on Image Processing, 2005.

RUAN, R., ZHANG, Y. and ZHOU, Y. 2008. Change Detection Of Wetland In Hongze Lake Using A Time Series Of Remotely Sensed Imagery. s.l. : The International Archives of the Photogrammetry, Remote Sensing and Spatial Information Sciences, 2008. Vol. XXXVII.

Samat, Narimah, Hasni, Rosmiyati and Elhadary, Yasin Abdalla Eltayeb. 2011. Modelling Land Use Changes at the Peri-Urban Areas Using Geographic Information Systems and Cellular Automata Model. *Journal of Sustainable Development.* 2011. Vol. 4.

Shaoqing, Zhang. 2008. *The Comparative Study Of Three Methods Of Remote Sensing Image Change Detection.* China : s.n.

Singh, A. 1989. *Digital change detection techniques using remotely-sensed data.* s.l. : Taylor & Francis, 1989.

Smith, Randall B. 2012. Introduction to Remote Sensing. 2012.

TANG, J., WANG, L. and YAO, Z. 2007. Spatio-temporal urban landscape change analysis using the Markov chain model and a modified genetic algorithm. 2007.

Théau, Jérôme. 2012. Change detection. [ed.] David M. Danko Wolfgang Kresse. *Springer Handbook of Geographic Information.* New york : Springer, 2012, 7.

Tyagi, Priti and Bhosle, Udhav. 2011 . Atmospheric Correction of Remotely Sensed Images in Spatial and Transform Domain. *International Journal of Image Processing (IJIP).* 2011 . Vol. 5, 5.

U.S. Geological Survey. 1998. *Overview of Middle East Water Resources.* s.l. : Executive Action Team, 1998. p. 41.

USGS. 2008. Landsat Update. *Landsat Update.* 2008. Vol. 2, 1.

Wen, Wen. 2008. Wetland Change Prediction Using Markov Cellular Automata Model in Lore Lindu National Park Central Sulawesi Province, Indonesia. 2008.

Yao, Xin. 2010. cellular-automata. *university of birmingham.* [Online] 2010. http://www.cs.bham.ac.uk/internal/courses/intro-nc/current/notes/02-cellular-automata.pdf.

Zhang, Qian, et al. 2009. Simulating urban development scenarios using Markov-Cellular automata a case study of greater Shanghai area, China. 2009.